

**Titre:** Surface Defect Visibility on Low-Emissivity Coatings After Heat  
Title: Treatment

**Auteur:** Oumar Touré  
Author:

**Date:** 2024

**Type:** Mémoire ou thèse / Dissertation or Thesis

**Référence:** Touré, O. (2024). Surface Defect Visibility on Low-Emissivity Coatings After Heat  
Citation: Treatment [Mémoire de maîtrise, Polytechnique Montréal]. PolyPublie.  
<https://publications.polymtl.ca/61984/>

 **Document en libre accès dans PolyPublie**  
Open Access document in PolyPublie

**URL de PolyPublie:** <https://publications.polymtl.ca/61984/>  
PolyPublie URL:

**Directeurs de  
recherche:** Ludvik Martinu, & Jolanta-Ewa Sapieha  
Advisors:

**Programme:** Génie physique  
Program:

**POLYTECHNIQUE MONTRÉAL**

affiliée à l'Université de Montréal

**Surface defect visibility on low-emissivity coatings after heat treatment**

**OUMAR TOURÉ**

Département de génie physique

Mémoire présenté en vue de l'obtention du diplôme de *Maîtrise ès sciences appliquées*

Génie physique

Décembre 2024

# **POLYTECHNIQUE MONTRÉAL**

affiliée à l'Université de Montréal

Ce mémoire intitulé :

**Surface defect visibility on low-emissivity coatings after heat treatment**

présenté par **Oumar TOURÉ**

en vue de l'obtention du diplôme de *Maîtrise ès sciences appliquées*

a été dûment accepté par le jury d'examen constitué de :

**Alain ROCHEFORT**, président

**Ludvik MARTINU**, membre et directeur de recherche

**Jolanta-Ewa SAPIEHA**, membre et codirectrice de recherche

**Daniel THERRIAULT**, membre

## ACKNOWLEDGEMENTS

First and foremost, a special thank you goes out to my research director and co-director, Ludvik Martinu and Jolanta-Ewa Sapieha for graciously welcoming me into the FCSEL and providing me the opportunity to expand my research project in a warm, collaborative, and supportive environment. I am fortunate to have been part of this laboratory, where a community of knowledgeable, insightful, and passionate people continually encouraged me to grow and think critically, both personally and professionally.

On a more practical note, a big thank you to the technicians, Francis Turcot and Francis Boutet, who were always available at a moment's notice and generously offered their time and insight for the benefit of every project, saving me days, if not weeks, of additional work.

Additional credit and gratitude need to be accorded to the past and current research associates of the lab, Jincheng Qian, Oleg Zabeida, and, especially, Bill Baloukas, for their thorough revisions and commentary on my work throughout these two years, ever forcing me to question my results and always dig deeper for more answers. Bill, thank you for *closely* following me every step of the way, your attention to detail and undeniable experience in the field paired with your immense professionalism and congenial spirit made this journey memorable.

Marie-Andrée, I cherished our partnership from the very first day, when we were figuring out everything one day at a time. Phillip, you have the most research-oriented mind that I've ever come across, I was fortunate enough to work on a project similar to yours and our discussions were always the most insightful. I am lucky to have had you as my mentor and, dare I say, my friend, throughout these few years and beyond. The sentiment is shared for all my other colleagues at the FCSEL as well, this page is too short to name you all, but you truly made this lab feel like a family.

Speaking of family, my last acknowledgements go out to them. To my mother and father, brother and sisters, you mean the world to me, and nothing would've been possible without your unwavering support. Friends of Poly, your presence made everything outside of work so much more enjoyable, I am grateful to have connected with like-minded people. Finally, but certainly not least, Nicolas and Jean-Marc, who are like two older brothers to me at this point, I am proud and extremely thankful to have you both in my life. To many more years of fraternity to come.

## RÉSUMÉ

La consommation et la gestion de l'énergie gouvernent notre monde. Les revêtements à faible émissivité (« low-e coatings ») sont un type de revêtement fonctionnel déposé sur le verre architectural, destiné à être utilisé sur des fenêtres, tant pour des applications résidentielles que non résidentielles. Ils filtrent essentiellement les radiations infrarouges entrantes et sortantes des bâtiments, rendant ainsi la fenêtre plus thermiquement efficace et réduisant simultanément les coûts liés au chauffage et à la climatisation qui découlent de la mauvaise isolation typique des fenêtres non revêtues.

Les revêtements à faible émissivité existent déjà depuis quelques décennies maintenant et se présentent, sous leur forme optimale, comme une série de couches extrêmement minces disposées dans une configuration diélectrique/métal/diélectrique. L'utilisation d'une fine couche métallique, le matériau le plus utilisé étant l'Ag pour ses propriétés optiques favorables dans les régions infrarouge et visible, est essentielle dans la conception du revêtement final. Ce verre revêtu doit être « trempé », c'est-à-dire traité thermiquement à haute température pendant de courtes périodes afin d'obtenir un verre renforcé thermiquement qui peut être utilisé en toute sécurité pour les bâtiments. Cependant, entre le dépôt du revêtement et le processus de trempe du verre, des défauts peuvent être générés à la surface des revêtements lors de la manipulation manuelle et robotique, du nettoyage et du polissage des produits. Sous l'effet du traitement thermique, ces défauts, qui peuvent être complètement invisibles avant le traitement, peuvent devenir très visibles, pouvant mener au rejet total du produit et rendant le contrôle de la qualité des produits difficile à gérer.

Cette étude définit ces objectifs autour de cette problématique: reproduire des défauts de rayures visibles sur les revêtements, développer des techniques pour observer et quantifier l'apparition de défauts sur les revêtements avant et après le traitement thermique (HT), et proposer un modèle de dégradation pour l'intensification des défauts observés après le traitement thermique. L'analyse microstructurale et chimique, à l'aide de la microscopie AFM, SEM, TEM et des images EDS, a révélé différents modes de défaillance sur les échantillons après les tests de rayures. Des cas de déformation plastique, de fissuration par traction, ainsi que de délamination partielle et totale ont été observés sur les échantillons testés, variant en occurrence et en densité en fonction de la charge appliquée lors des tests de rayures. Un dispositif expérimental de photographie a été mis en place

pour prendre des images reproductibles de manière précise, en utilisant des paramètres d'imagerie identiques, afin de comparer de manière adéquate le comportement avant et après traitement thermique. De plus, un code de traitement d'images *Python* a été développé pour quantifier la visibilité et l'intensification des rayures via la définition de "métriques de visibilité" extraites des images prises précédemment.

Enfin, les résultats des deux premiers objectifs ainsi que des expériences supplémentaires visant à modifier le comportement d'intensification des rayures après traitement thermique ont été utilisés pour proposer un modèle de dégradation pour les revêtements à faible émissivité à base d'Ag. Il a été constaté que la dégradation observée après le traitement thermique, dans les traces des rayures, se manifestait par de multiples zones de délamination, où le revêtement et le substrat en verre étaient complètement séparés l'un de l'autre. De plus, la dégradation de la couche d'Ag était significative, la plupart du matériau métallique ayant diffusé ailleurs dans le revêtement, formant de grands amas d'atomes d'Ag. Ces caractéristiques de dégradation ont été liées à la formation de fissures et à la perturbation de la couche d'Ag ainsi que de sa couche protectrice formée après la rayure, permettant une grande mobilité des atomes d'Ag et, ainsi, une dégradation et une visibilité accrue de la rayure. Différentes méthodes pour modifier l'intensification ont également été testées et sont présentées; ceci comprend notamment l'influence du stockage du revêtement dans un environnement haut en humidité qui s'est avérée significative lors de l'observation des rayures créées utilisant une faible charge lors des tests de rayures, où la disruption des couches du revêtement est minimale. Des améliorations et des recommandations concernant le modèle de dégradation proposé sont également considérées.

## ABSTRACT

Energy consumption and management are very important in our world. Low-emissivity (low-e) coatings are a type of functional coating deposited on architectural glass, to be used on windows, for residential and non-residential applications. They effectively filter infrared radiation from entering and exiting buildings, rendering the window more thermally efficient, and, simultaneously, reducing resulting heating and cooling costs that arise from the typically poor insulation properties of un-coated windows.

Low-e products have been around for a few decades now and consist, in their optimal form, as a series of extremely thin layers arranged in a dielectric/metal/dielectric arrangement. The use of a thin metallic layer, the most used material being Ag for its favorable optical properties in the infrared and visible region, is critical in the design of the overall coating. Such coated glass most often needs to be tempered, i.e. heat-treated at high temperatures for short periods in order to obtain thermally toughened glass that can be safely applied to buildings. However, between the deposition and tempering process of the glass, defects can be generated on the surface of the coatings via manual and robotic manipulation, cleaning, and polishing of the glass products. Following the heat treatment (HT), these defects, which can be completely invisible prior to heating, can become highly visible, leading to rejection of the product as well as rendering the quality control of the products difficult to manage.

This work based its objectives around the following subject matter: reproduce noticeable scratch defects on low-e coatings, develop techniques to observe and quantify the appearance of as-coated and heat-treated defects on the coating, and propose a degradation model for the intensification of the defects observed post-HT. Topological and chemical analysis using AFM, SEM, TEM, and EDS imagery revealed various failure modes occurring on the samples following the scratch tests. Instances of plastic deformation, tensile cracking, partial and full delamination were all observed on the tested samples, varying in density and occurrence as a function of the applied load during scratch testing. An experimental photography setup was developed to accurately take reproducible images, using identical imaging parameters, and adequately compare the as-coated and heat-treated states. In addition, a *Python* image processing code was also developed to quantify the observed

visibility and intensification of the scratches via the definition of visibility metrics extracted from the previously taken images.

Finally, the result of the first two objectives as well as additional experiments aiming to alter the intensification behavior seen on the heat-treated scratches were used to propose a degradation model for Ag-based low-e coatings. It was found that the degradation witnessed following the HT within the scratch tracks manifested itself as multiple delaminated regions, where the coating and the glass substrate were fully separated from one another. Additionally, degradation of the Ag layer was significant, where most of the metallic material had diffused elsewhere in the coating, forming large clusters of Ag atoms. These degradation features were linked with the crack formation and disruption of the Ag layer as well as of its protective layer that were created after scratching, enabling a higher mobility of Ag atoms and thus, degradation and higher visibility of the scratch. Different means of altering the intensification were also tested and, most notably, the influence of storing scratched samples in high humidity revealed itself to be significant when observing the intensification of low loading scratches, where disruption of the layers of the coating is minimal. Improvements and recommendations regarding the proposed degradation model are also considered.



## TABLE OF CONTENTS

ACKNOWLEDGEMENTS .....	III
RÉSUMÉ.....	IV
ABSTRACT .....	VI
LIST OF TABLES .....	XI
LIST OF FIGURES .....	XII
LIST OF SYMBOLS AND ABBREVIATIONS.....	XVII
LIST OF APPENDICES .....	XXII
CHAPTER 1    INTRODUCTION.....	1
1.1    Low-emissivity windows .....	1
1.2    Context of the research.....	6
1.3    Objectives.....	7
1.4    Outline .....	8
CHAPTER 2    THEORY & LITERATURE REVIEW .....	10
2.1    Low-emissivity coatings .....	10
2.1.1    Optical Performance.....	12
2.1.2    Design considerations .....	18
2.2    Durability of silver-based low-e coatings .....	21
2.2.1    Mechanical properties .....	21
2.2.2    Scratch resistance .....	26
2.2.3    Degradation mechanisms .....	29
2.2.4    Enhanced durability of Ag .....	34
CHAPTER 3    METHODOLOGY .....	38
3.1    Sample preparation.....	38

3.1.1	Coating deposition.....	38
3.1.2	Preparation of samples .....	40
3.2	Mechanical characterization.....	41
3.2.1	Scratch tests .....	41
3.2.2	Indentation.....	43
3.3	Heat treatments.....	45
3.4	Assessment of defect visibility.....	46
3.4.1	Visibility setup .....	46
3.4.2	Image processing .....	49
3.5	Topography Analysis .....	52
3.5.1	Scanning electron microscopy .....	52
3.5.2	Atomic force microscopy .....	54
3.6	Elemental composition analysis .....	56
3.6.1	X-ray photoelectron spectroscopy.....	56
3.6.2	Energy-dispersive X-ray spectroscopy .....	58
3.7	Additional characterization techniques .....	60
3.7.1	Focused ion beam milling/Transmission electron microscopy .....	60
3.7.2	Humidity tests .....	62
CHAPTER 4	RESULTS & DISCUSSION.....	63
4.1	Preliminary characterization .....	63
4.1.1	Design & architecture.....	63
4.1.1	Mechanical performance .....	64
4.2	Reproducing noticeable surface defects .....	67
4.2.1	As-coated scratches .....	67
4.2.2	Intensification following heat treatment .....	71

4.3	Influences on defect visibility .....	79
4.3.1	Heat treatment .....	79
4.3.2	Effect of humidity .....	83
4.3.3	Effect of the stack architecture.....	87
CHAPTER 5	GENERAL DISCUSSION.....	93
CHAPTER 6	CONCLUSION AND RECOMMENDATIONS.....	99
REFERENCES	.....	102
APPENDIX	.....	106

## LIST OF TABLES

<b>Table 2.1:</b> Result summary of nanoscratch testing on a TAG low-e coating. Average values of 5 scratches of 100 $\mu\text{m}$ length with a progressive maximum load of 20 mN. Recreated from [38]	<b>28</b>
<b>Table 2.2:</b> Diffusion coefficient values calculated for $\text{TiO}_2/\text{Ag}/\text{TiO}_2$ stacks annealed over the temperature range of 100 $^{\circ}\text{C}$ – 600 $^{\circ}\text{C}$ for 5 min. Recreated from J. Kulczyk-Malecka et al. [18]	<b>31</b>
<b>Table 4.1:</b> Result summary of micro scratch testing on the REF sample depicting the average and standard deviation values of the three pre-defined $\text{Lc}_i$ . The scratches were performed with a Rockwell-C diamond 20 $\mu\text{m}$ indenter tip with forward (23 scratches) and backward (10 scratches) mode scratching, were 1 mm in length and produced with a maximum load of 1.5 N.	<b>66</b>
<b>Table 5.1:</b> Quantifiable observed changes on the coating's integrity for the two different load regimes of scratching.	<b>94</b>

## LIST OF FIGURES

<b>Figure 1.1:</b> Global final worldwide energy consumption (left) and emissions (right) by sector in 2021 [1]. .....	<b>1</b>
<b>Figure 1.2:</b> Solar and room temperature blackbody emission spectra alongside the ideal transmittance spectra for low-e glazings in warm and cold climates [4]. .....	<b>3</b>
<b>Figure 1.3:</b> Representation of a double insulating glass unit (IGU) [10]. .....	<b>4</b>
<b>Figure 2.1:</b> a) Generalized architecture of an optimized single Ag low-e coating. b) Practical example of a single Ag patented coating [20]. c) Practical example of a triple Ag patented coating [21]. .....	<b>11</b>
<b>Figure 2.2:</b> Reflectance of various metals with a thickness of 15 nm alongside the relative solar spectrum [19]. .....	<b>14</b>
<b>Figure 2.3:</b> Simplest DMD architecture schematic (inset) and modeled $R$ and $T$ response for a $\text{TiO}_2$ / Ag (11nm) / $\text{TiO}_2$ coating, using <i>OpenFilters</i> . .....	<b>15</b>
<b>Figure 2.4:</b> Reflection and transmission spectra for Ag films as a function of thickness ranging from 5 nm to 106 nm [24]. b) Evolution of the transmittance of a DMD stack as a function of Ag thickness ranging from 10 nm to 40 nm [4]. .....	<b>16</b>
<b>Figure 2.5:</b> DMD representation of a a) single, b) double and c) triple Ag low-e coating alongside d) their respective optical responses with identical total Ag thickness (40 nm) and AZO thickness adjusted to maximize $T_{\text{vis}}$ [4]. .....	<b>17</b>
<b>Figure 2.6:</b> Transmission spectra of low-e coatings used in commercial windows [8]. .....	<b>18</b>
<b>Figure 2.7:</b> Planar FE-SEM images showing the morphological evolution of pure Ag, deposited on a $\text{SiO}_2$ substrate as a function of the nominal thickness. The scale bars represent 50 nm. Adapted from [29]. .....	<b>19</b>
<b>Figure 2.8:</b> Apparent hardness and Young's modulus (inset) as a function of indentation depth for a low-e coating on glass before and after heat treatment at 700°C for 3 min in air [12]. .....	<b>22</b>
<b>Figure 2.9:</b> Parabolic deflection curves for an as-received glass substrate, a as-deposited low-e coating and a heat-treated (500°C, 4 min) low-e coating [12]. .....	<b>24</b>
<b>Figure 2.10:</b> Principal residual stress profiles ( $\sigma_1$ and $\sigma_2$ ) as a function of depth: (a) before heat treatment and (b) after heat treatment (540°C, 12 min) [37]. .....	<b>25</b>

<b>Figure 2.11:</b> Scratch test failure regimes in terms of substrate and coating hardness as defined by S. J. Bull [44].....	<b>26</b>
<b>Figure 2.12:</b> Schematic assignment of the critical loads $LC_1$ - $LC_3$ to the respective coating failure patterns [47].....	<b>27</b>
<b>Figure 2.13:</b> Comparison of two <i>in situ</i> SEM pictures: a) at the beginning of the hole propagation step. b) at the beginning of the sintering step. The shape of grains present in b) are superposed in green in a). Zones delimited with white lines in b) represent the ensemble of points closer to the grain inside the zone than any other grain, the so-called “zone of influence”. Scale bar is 1 $\mu\text{m}$ . ....	<b>30</b>
<b>Figure 2.14:</b> SEM image of Ag/TiO <sub>2</sub> nanofilms (a) before heat treatment and (b) after heat treatment with their corresponding EDS line profiles [15]. ....	<b>32</b>
<b>Figure 2.15:</b> Sheet resistance of a Ti (2 nm) /Ag (10 nm) bilayer exposed to an O <sub>2</sub> plasma [31]. ....	<b>33</b>
<b>Figure 2.16:</b> a) Schematic image of a coating scratch by means of arc-shaped tensile cracks and recovery spallation failure of the coating. b) Dark field microscope images for 100-nm-thick pure Ag, Ag <sub>70</sub> Cu <sub>30</sub> and pure Cu films [62].....	<b>36</b>
<b>Figure 3.1:</b> a) Schematic representation of a scratch test with the indenter passing over the surface of the sample, modified from [63]. The displacement and applied load can both be controlled to achieve the desired scratch morphology. b) Pre- and post-scan methodology used to calculate and derive key scratch test variables recreated from [64].....	<b>42</b>
<b>Figure 3.2:</b> a) Schematic representation of an indentation test with the indenter pressing against the surface of the sample. b) Theoretical geometrical parameters derived from the indentation print used for calculations of the elastic modulus and hardness of the analysed specimen. c) Resulting load-displacement curve obtained from an indentation test. ....	<b>44</b>
<b>Figure 3.3:</b> a) Side view and b) front view of a schematic representation of the visibility setup. c) Image of the completed visibility setup with key features. 1: Digital camera equipped with a macro lens; 2: Support bridge; 3: Light strip; 4: XYZ micrometric stage; 5: Sample holder. ....	<b>47</b>
<b>Figure 3.4:</b> a) Grayscale image of a scratched and heat-treated low-e sample. b) Corresponding plot of the averaged pixel intensity (in the y direction of the original image) of the as-coated (green) and heat-treated (red) scratched low-e coating sample.....	<b>50</b>

<b>Figure 3.5:</b> a) Calculation methodology of the key metrics used for scratch visibility assessment: as-coated and heat-treated peak intensity and background values (AC PI, AC Bkg, HT PI and HT Bkg), variation of peak intensity ( $\Delta PI$ ) and scratch width ( $S_w$ ). b) Calculation methodology for the percentage area of coverage of a scratch ( $\% S_{Co}$ ), based on high and low intensity pixels within a predefined area. ....	<b>52</b>
<b>Figure 3.6:</b> Various detectable signals derived from the electron-matter interactions when analyzing a specimen with a focused electron beam [66]. ....	<b>54</b>
<b>Figure 3.7:</b> Schematic representation of atomic-force microscopy (AFM) [67]. ....	<b>55</b>
<b>Figure 3.8:</b> Schematic representation of the photoelectron emission effect [68]. ....	<b>57</b>
<b>Figure 4.1:</b> Architecture of the low-e coating reference sample used in this project (left) and corresponding compositional XPS depth-profiles (right). ....	<b>64</b>
<b>Figure 4.2:</b> Measured $E_r$ and $H$ on a REF sample as well as on a bare SLG substrate. ....	<b>65</b>
<b>Figure 4.3:</b> a) Microscope panoramic image of a progressive loading scratch (from 0 N to 1 N) with identified specific loads (in green) and critical loads (in red). b) SEM (2500x magnification) and c) microscope (500x magnification) images of the observed failure modes. ....	<b>68</b>
<b>Figure 4.4:</b> a) Plastic deformation depth profiles for various constant load scratches performed on a reference sample with b) inset graph representing the profiles of lower load scratches. c) AFM 3D mapping of a low load scratch (0.4 N on the top) and a higher load scratch (0.8 N on the bottom). ....	<b>69</b>
<b>Figure 4.5:</b> Visibility setup images of an as-coated, scratched reference sample (with various constant load scratches ranging from 0.2 N to 1.2 N) taken with a) lighting configuration A and b) lighting configuration B (see Section 3.4.1). ....	<b>70</b>
<b>Figure 4.6:</b> a) As coated and b) heat-treated images of constant load scratches (ranging from 0.2 N to 0.8 N) taken on a reference sample with lighting configuration A. ....	<b>71</b>
<b>Figure 4.7:</b> AC and HT microscope image (100x magnification) of a a) low load scratched (0.4 N) and b) high load scratched (0.8 N) reference sample. ....	<b>72</b>
<b>Figure 4.8:</b> SEM and EDS mapping (Ag) image of a) low load (0.4 N) and b) high load (0.8 N) scratches following heat-treatment. ....	<b>73</b>

- Figure 4.9:** SEM images of the cross-section exposed for the TEM analysis as well as the corresponding higher magnification SEM images of the cross-section of a) an as-coated and b) heat-treated, 0.4 N scratch. ....74
- Figure 4.10:** a) Full TEM images of a lamella taken from an as-coated scratched sample (0.4 N load) (see Figure 4.9a for SEM images). b), c) and d) correspond to higher magnification TEM images of regions of interest within the cross-section. ....75
- Figure 4.11:** a) Full TEM images of a lamella taken from a heat-treated scratched sample (0.4 N load) (see Figure 4.9b for SEM images). b), c), d) and e) correspond to higher magnification TEM images of regions of interest within the cross-section. ....77
- Figure 4.12:** DF-TEM images taken from a heat-treated scratched sample (0.4 N load)78 paired with corresponding EDS mappings for chemical analysis highlighting a) Ag nanoparticle formation, and b) full delamination of the coating.....78
- Figure 4.13:** a) Images of the four REF samples, each scratched at four constant loads of 0.4 N and heat-treated with increasing durations at 650 °C (6, 9, 12 and 15 minutes). Images taken with f/16 for the aperture, 100 ISO and 2 s of exposure. b) Corresponding average scratch width (**Sw**) and variation of peak intensity ( $\Delta PI = HT PI - AC PI$ ) values extracted from the images.....80
- Figure 4.14:** a) Images of the four REF samples, each scratched at four constant load of 0.6 N and heat-treated with increasing durations at 650 °C (6, 9, 12 and 15 minutes). Images taken with f/16 for the aperture, 100 ISO and 2 s of exposure. b) Corresponding average scratch width (**Sw**) and variation of peak intensity ( $\Delta PI = HT PI - AC PI$ ) values extracted from the images. ....82
- Figure 4.15:** Visibility setup images of scratched coatings: a) as-coated, to be stored in a high humidity environment for 20 h; b) after storage and heat-treatment; c) as-coated, to be stored in a low vacuum environment for 20 h; d) after storage and heat-treatment. Images were taken with f/16 for the aperture, 100 for the ISO and exposed for 0.5 s. e) Corresponding  $\Delta PI$  (bold colors, left axis) and  $\Delta S_w$  (light colors, right axis) metrics obtained via the image processing code. ....84
- Figure 4.16:** SEM images presenting the observed degradation features on a) a heat-treated sample stored in a high humidity for 0.3 N and 0.4 N load scratches, and b) a heat-treated sample stored in a low vacuum environment for 0.3 N and 0.4 N load scratches as well. ....86



- Figure 4.17:** SEM images presenting an observed degradation feature of interest on a) a heat-treated sample stored in a high humidity for 0.4 N load scratches, and b) heat-treated sample stored in a low vacuum environment for 0.4 N load scratches as well as the respective EDS mapping for Ag elemental chemical composition analysis.....**86**
- Figure 4.18:** Architectures of a) the REF sample, b) coatings with changes in the topcoat: T-1 (no  $\text{ZrO}_2$ ) and T-2 (no  $\text{SiN}_x$ ), c) coatings with changes near the Ag layer: T-5 ( $\text{NiCrO}_x$ ) and T-6 (no  $\text{NiCrO}_x$ ), d) coatings with changes in the Ag layer: C-5 (thicker Ag) and C-6 (no Ag), and e) coatings with changes in the bottom layers: B-4 (no  $\text{SiZrN}_x$ ). .....**88**
- Figure 4.19:** Visibility setup images of AC and HT scratches (constant load from 0.8 N to 0.2 N, left to right) on the REF sample as well as five variant stacks of interest: T-2 (no  $\text{SiN}_x$ ), T-5 ( $\text{NiCrO}_x$ ), T-6 (no  $\text{NiCrO}_x$ ), C-5 (thicker Ag) and C-6 (no Ag). .....**89**
- Figure 4.20:** Histogram presenting the variation of peak intensity ( $\Delta\text{PI}$ ) for the different tested variant stacks for lower and higher equivalent loading as well as the heat-treated background intensity values (HT Bkg). .....**90**
- Figure 5.1:** a) Full TEM image of a lamella taken from a heat-treated (under SEM) scratched sample (0.8 N load). b), c) and d) correspond to higher magnification TEM images of regions of interest within the cross-section. ....**95**

## LIST OF SYMBOLS AND ABBREVIATIONS

### Abbreviations

AC	As-coated
AFM	Atomic force microscopy
BE	Binding energy
BF	Bright field
Bkg	Background
BSE	Backscattered electrons
COF	Coefficient of friction
DAG	Double Ag
DC	Direct current
DF	Dark field
DL(s)	Dielectric layer(s)
DMD	Dielectric/Metal/Dielectric
EDS	Energy dispersive X-ray spectroscopy
FDM	Frank-van der Merve (growth mode)
FIB	Focused ion beam
HT(s)	Heat treatment(s), heat-treated
IEA	International Energy Agency
IGU	Insulated glass unit
IR	Infrared
KE	Kinetic energy
Lc <sub>i</sub>	Critical load <i>i</i>

LED	Light-emitting diode
Low-e	Low-emissivity
ML	Metallic layer
NIR	Near infrared
PI	Peak intensity
PVD	Physical vapor deposition
REF	Reference
RF	Radio frequency
SAG	Single Ag
SE	Secondary electrons
SEM	Scanning electron microscopy
SHGC	Solar heat gain coefficient
SLG	Soda-lime glass
SPM	Scanning probe microscopy
TAG	Tripple Ag
TEM	Transmission electron microscopy
UN	United Nations
VW	Volmer-Weber (growth mode)
XPS	X-ray photoelectron spectroscopy

**Elements and materials**

Ag	Silver
Ar	Argon
Au	Gold
AZO	Aluminum dopped zinc oxide
C	Carbon
Cr	Chrome
Cu	Copper
H	Hydrogen
ITO	Indium titanium oxide
N	Nitrogen
NiCr	Nickel chrome
Si	Silicon
SiN	Silicon nitride
SnO	Silicon oxide
Ti	Titanium
Zn	Zinc
ZnO	Zinc oxide

## Symbols and units

%RH	Relative humidity (percentage)
%S <sub>Co</sub>	Area of scratch coverage (percentage)
Å	Angstrom
<i>A</i>	Absorptance
<i>A<sub>p</sub></i>	Projected contact area
<i>d</i>	Thickness
<i>D</i>	Diffusion coefficient
<i>E<sub>r</sub></i>	Reduced Young's modulus
<i>H</i>	Hardness
h	Hour
in	Inches
<i>k</i>	Complex component of the refractive index, extinction coefficient
<i>n</i>	Real component of the refractive index
<i>R</i>	Reflectance
<i>S</i>	Stiffness
<i>S<sub>w</sub></i>	Scratch width
<i>T</i>	Transmittance
<i>T<sub>Vis</sub></i>	Luminous transmittance
ω	Frequency
<i>Z</i>	Atomic number
Δ	Variation
ε	Relative permittivity

$\epsilon_0$	Permittivity of vacuum
$\lambda$	Wavelength
$\sigma$	Conductivity
$\sigma_{1,2}$	Anisotropic stresses

## LIST OF APPENDICES

APPENDIX A	VISIBILITY ASSESSMENT <i>PYTHON</i> CODE – IMAGE PROCESSING
	..... 106

## CHAPTER 1 INTRODUCTION

### 1.1 Low-emissivity windows

In the present age of immense urbanization, human activities related to energy consumption, energy management and, especially, greenhouse gas emissions play a critical role in the development of new technologies and how we manage existing ones. Figure 1.1 presents the end-use worldwide energy consumption (left) as well as the global emissions (right) by sector, taken from the *2022 Global Status Report for Buildings and Construction* by the United Nations (UN) Environment Program [1]. It can be seen that approximately 34% of all the energy consumption is reserved for building applications (residential, non-residential, construction industry, etc.) and approximately 37% of all sources of emissions originate from building-related activities (heating, cooling, lighting, equipment, etc.). Moreover, according to the International Energy Agency (IEA), assuming a growth similar to what we have observed in the past few years, the net energy consumption of buildings (using electricity and gas) is expected to increase by approximately 30% by 2040 [2].

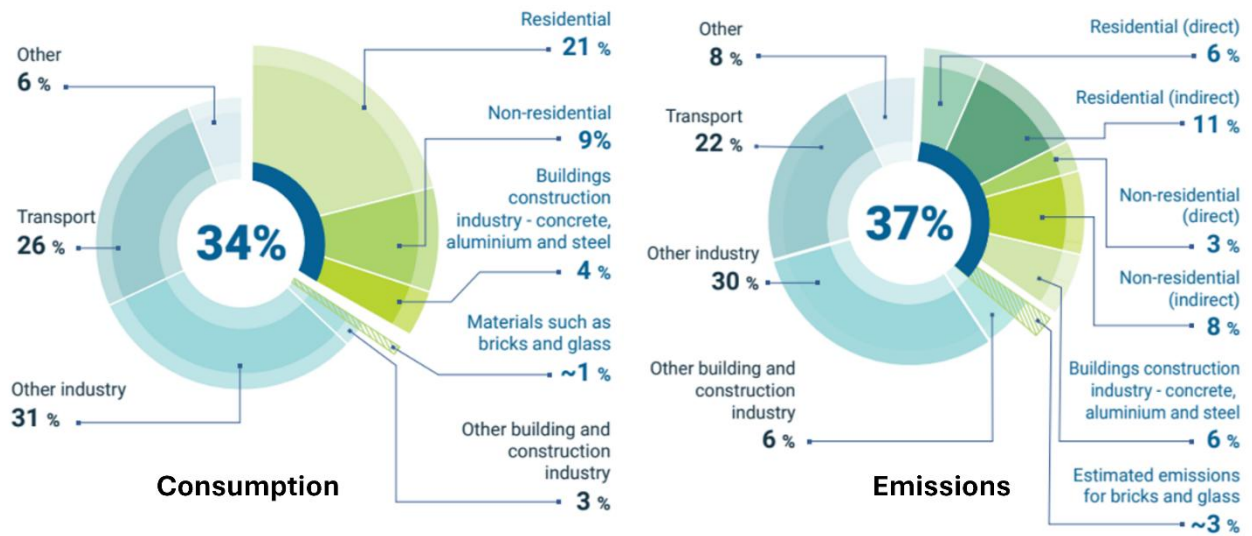


**Figure 1.1:** Global final worldwide energy consumption (left) and emissions (right) by sector in 2021 [1].

These statistics help paint a general picture of the importance of energy management, especially in the building sector, in the upcoming years. Apart from the energy used for lighting, appliances and



equipment in these buildings, a significant portion is used for space heating and cooling purposes [1]. Reducing, or at least, controlling the heat exchanges between the inside and the outside of buildings is thus critical.

In past years, efforts have been made to achieve this goal by mitigating one of the biggest sources of heat loss in homes and buildings: windows. In fact, heat gain and loss through common architectural glass is typically responsible for 25% to 30% of energy use related to temperature control in residential and non-residential buildings [3]. The reason being that commonly used float glass is highly emissive, meaning highly effective at emitting energy as thermal radiation. Thus, when heat is absorbed by the glass, it is re-radiated by the glass surface and can significantly alter interior temperatures during the day. Similarly, through blackbody radiation, hot buildings radiate (and lose) significant portions of their heat outside via these same windows, especially in winter. This gain or loss in thermal energy within buildings is then compensated with excess cooling or heating to achieve desirable interior temperatures.

The goal, to mitigate the above energy losses, is thus to decrease the emissivity of the glass by the addition of a low emissivity (low-e) coating, limiting the amount of radiative heat losses typically present in these buildings with, ideally, minimal impact on the amount of visible light passing through. Figure 1.2 shows the solar spectrum (black line) and room temperature blackbody spectrum (green line) alongside the ideal transmittance spectra for a low-e glazing in warm (red line) and cold (blue line) climates [4]. We see that a significant portion of the solar radiation falls within the near and short-wavelength infrared (IR) region ( $0.75\ \mu\text{m} - 3\ \mu\text{m}$ ). In warm climates, we would want to filter out as much radiation from the sun as possible, achieving an ideal filter like the one shown in red where almost all wavelengths above the visible are filtered out, guarantying a minimum heat gain, and thus minimizing cooling energy consumption/costs/emissions. Inversely, in cold climates, we would prioritize a filter such as the one shown in blue in the figure: allowing for a maximum transmission of solar radiation to minimize heating energy consumption/costs/emissions, but still reflecting the radiation of a blackbody at room temperature, ensuring that we don't lose the building's own interior heat.

Significant research efforts in the past years have focused on designing, manufacturing, characterizing, and optimizing these so-called low-emissivity glazings, commonly referred to as

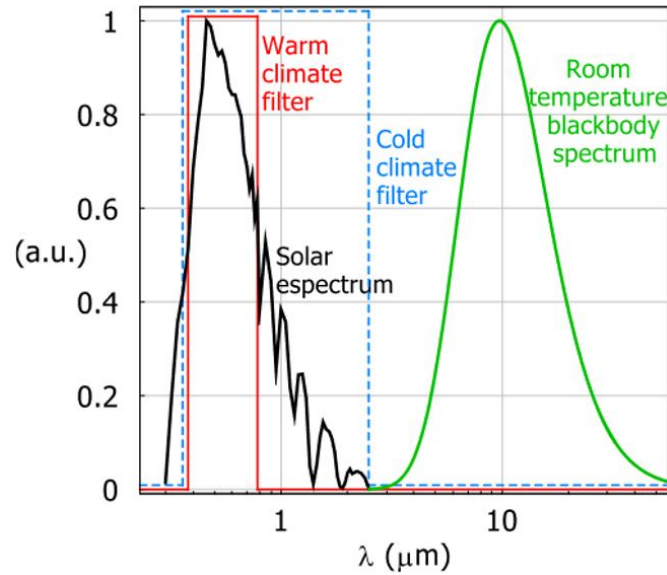


**Figure 1.2:** Solar and room temperature blackbody emission spectra alongside the ideal transmittance spectra for low-e glazings in warm and cold climates [4].

low-e coatings on glass. Low-e coatings are generally categorized in two separate groups: hard coatings, deposited during the glass formation process, and soft coatings, deposited after the formation of the glass [5], [6]. Hard coatings, typically based on indium tin oxide (ITO) for its thermal and optical properties, usually present higher weather, corrosion, and abrasion resistance due to its dielectric-like nature and the strong bond created between the coating and the glass [7]. On the other hand, soft coatings, are usually weaker, but present better optical properties as they most often use silver (Ag) and are optimized on the nanoscale forming multilayer architectures. Between both categories of coatings, hard coatings use significantly less material for production (up to 10-20x less) and have been shown to be more compatible for large-scale production, as the deposition process is less complex and expensive than soft coatings [7], [8], [9]. However, soft coatings provide lower emissivity values, lower solar heat gain, and transmit more visible light, hence why they are often used on highly optimised low-e products. As the present work focuses on soft low-e coatings, hard low-e coatings will not be further addressed.

The simplest designs of soft low-e coatings (further referred to simply as low-e coatings) typically include a single thin conductive metallic layer (ML) encapsulated between at least two (often more) dielectric layers (DLs). This very thin metallic layer (usually silver in the range of 8-15 nm of

thickness) plays the most important role in the whole architecture by efficiently reflecting IR radiation due to its high conductivity as well as providing high visible transmittance in the case of Ag. Neighboring dielectric layers (with optimized thicknesses), on the other hand, play multiple secondary roles ensuring an optimized final product. They primarily act as protective layers shielding the Ag film from ionic diffusion from the glass substrate as well as during the deposition process, which introduces and generates multiple reactive species in the deposition chamber [7]. Other roles of some of the DLs include antireflective properties by increasing the visible light transmission via optical interference, the use of a *seed layer* to optimize the deposition and growth of Ag, and protective topcoats to ensure a higher mechanical resistance to scratching and higher corrosion resistance via their barrier properties that protect the Ag layer from elements which can lead to its corrosion.

Low-e coatings present a major drawback of not being extremely weather-, corrosion- and scratch resistant. In practice, one ingenious way to protect these coatings from the external environment is to install them in an insulated glass unit (IGU) as shown in Figure 1.3 [10]. Here, an example of an installed coating on surface 2 is shown, but, in principle, the coating could be present on all four surfaces. In typical configurations (on surfaces 2 or 3), the coating is deposited in such a way that it faces the interior of the insulating unit and thus is protected from both the exterior and the interior environments. Furthermore, the inside of these IGUs is often filled with an inert gas such as argon (Ar), providing better thermal insulation than air and further protecting the coating from entering into contact with any type of hostile environment (e.g.: humidity).

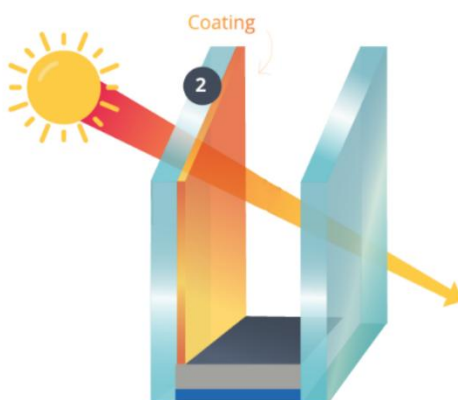


**Figure 1.3:** Representation of a double insulating glass unit (IGU) with a low-e coating deposited on surface 2 [10].

While protection of the *installed* coating is successful and permits a shelf life of the product for up to 20 years using such units, this arrangement does not address the weak nature of these low-e coatings prior to their installation. As briefly mentioned above, during the production of such coatings, specific material and deposition conditions are chosen to protect and achieve the desired *as-coated* (AC) coating. What is often hard to control is the post-deposition performance of such coatings following multiple steps required between the AC state and the installed state. In fact, as expected, various manipulations of the coated glass are required before it arrives at its final destination. Cleaning procedures, sanding and polishing practices, storage, loading, and shipping of the products are among the many activities that expose the coating to various hostile environments, rendering it susceptible to damage (scratches, cracks, etc.) that is often undetectable to the human eye [11]. Some of the most damaging steps include the cutting of the glass as well as displacement and manipulation of large glass panes with robotic arms, where dust (or residual glass particles from the cutting) stuck underneath the suction cups is also expected to lead to significant damage. Furthermore, a final heat treatment (HT) is typically performed to obtain toughened glass for increased safety in architectural applications. While toughened glass shatters into small pieces upon breaking (a desired property of safe glass), this also entails that, once heat-treated, the glass can no longer be precisely cut into specific sizes for various accommodations, explaining the need to have the low-e deposited on the glass prior to the HT. This HT, usually performed for a few minutes (6-15 minutes depending on substrate thickness) at high temperatures (450-700°C) also provides significant thermal energy to the coating [12], [13]. Assuming no damage to the integrity of the stack, material choices and thickness optimization are often sufficient to successfully protect the crucial ML layer from detrimental modifications during the HT. However, if some surface defect is present before the HT (scratches, cracks, contaminants, etc.) the added thermal energy can very well intensify and aggravate it increasing its size and rendering it much more visible [14], [15], [16], [17], [18]. These AC defects can be completely invisible before the HT and thus, appear seemingly unexpectedly following the HT. It goes without saying that these highly visible post-HT defects are undesirable from an aesthetic point of view. Furthermore, these HTs are usually performed after leaving the production facility by third-party customers, therefore, these visible defects appear later in the installation process and can no longer be controlled or mitigated by the coating supplier.

As a result, the present research focuses on this problematic by studying and investigating defects generated in controlled environments on as-coated low-e coatings, recreating what is observed in the field, as well as how they behave and evolve during and following heat treatments in the hopes of addressing unanswered questions pertaining to the physical mechanisms involved in the observed defect intensification.

## **1.2 Context of the research**

As expected, an important part of the design of low-e coatings is the choice of the material for the ML. This ML needs to be carefully chosen based on multiple technical, application and aesthetic criteria. On the technical side, it needs to have a high reflectance in the IR and low absorption in the visible range. For application purposes as well as large-scale production, a perfect ML candidate would need to be durable, compatible with other materials, have an easily controllable thickness during the deposition of very thin layers, be relatively low in cost and environmentally friendly. From an aesthetic perspective, the color and tint of the final product are also considered by customers during purchase. Commonly studied materials achieving acceptable results include Ag, Au, and Cu, offering satisfactory visible transmittance (above 50%) with thicknesses below 15 nm [19]. While the reflective properties of these ML are interesting in the IR region, they also present non-negligible absorption in the visible, minimizing the transmitted light through the film, which is obviously undesirable for low-e coating applications.

Guardian Glass, a world leader in glass innovation and production, is also heavily involved in the low-e industry, providing multiple low-e-based residential and architectural products to customers worldwide. As a means to further improve their products, Guardian Glass has shown interest in investigating the mechanical behavior of some of their products and reached out to MIC-CSE, the Multisectoral Industrial Research Chair in Coating and Surface Engineering with the intent to collaborate on this matter. The ultimate goal would then be to, once the physics behind the formation and intensification of the defects is known and well understood, modify the original design of the products accordingly to create more durable coatings that would, on the one hand, be more resistant to possible damage during production and, on the other hand, be optimized to minimize defect intensification during heat treatments. This work presents and summarizes the principal findings derived from this collaboration.

As mentioned above, when talking about low-emissivity coatings, optical performance and mechanical durability are among the most important aspects of the final design and product. As this thesis focuses on durability, especially on actual products purchased and used by customers, the various low-emissivity coatings used and analysed in this thesis were provided directly by Guardian Glass, with modifications to the original products made after internal discussions following the advancement of the project. Therefore, the optical properties and performance of the analysed samples were already well-documented and established and the focus could be kept on the study of the defect formation and the intensification of defects following the heat treatments.

### **1.3 Objectives**

The main objective of this research project is to understand the physical mechanisms behind the formation of defects on AC low-e coatings as well as understand their intensification during and after the HT procedure. Through characterization of the generated surface defects, we aim to better observe the underlying mechanisms related to their evolution between their as-coated and heat-treated states.

As this research heavily focuses on defect visibility and assessment of damage, there has been an interest in the industry to be able to quickly and efficiently observe and quantify, the damage on low-e products for quality control purposes. Consequently, in addition to the first objective, a secondary objective of this research was to develop an experimental setup that could be implemented in a production line, aiming to observe, qualify and, more importantly, quantify the visibility of defects on glass. Furthermore, adding an element of image processing on the taken pictures could help quantify the visibility/intensity of those defects. Such a setup and analysis would then assist in the regulation of the quality control of the products and allow an automation process to be implemented instead of typical human inspection.

Finally, following these first objectives, the goal is to develop a model of the degradation of silver-based low-e coatings during their heat treatment. This model would specify the physical mechanisms at play leading to degradation/accentuation of defects as well as explain the different behaviors we observe when studying the impact of various parameters (load of scratches, heat treatment duration, environment of heat treatment, etc.) on defect intensification.

Therefore, the sub-objectives of this thesis can be summarized in the three following points:

1. Characterization of the defects created on as-coated low-e coatings, i.e. generating scratches in a controlled environment and under controlled conditions (mode of scratching, applied load, geometry of counterpart, temperature, and humidity) and investigating them post-HT using various characterization instruments (SEM, TEM, AFM, EDS, etc.), thus replicating and analyzing typical damage observed in real-life applications.
2. Design and fabrication of an experimental setup that would be able to provide reproducible images with fixed, but controllable, parameters (lighting of the sample, sensitivity of the camera, exposure time, etc.) of the generated defects. Additionally, develop an image processing code in order to compare images taken on AC and HT samples and quantify the surface defects.
3. Develop a model of degradation of silver-based low-e coatings during their heat treatment.

## **1.4 Outline**

The following work is presented in the form of six chapters with this introduction being the first one. The second chapter, Theory & Literature Review, will provide a general overview of low-e coatings from their overall design which depends on the desired optical properties to their final performance. As this work is more focused on the durability of low-e coatings undergoing high-temperature heat treatments, some time will be spent on reviewing the mechanical properties, scratch resistance as well as typical degradation mechanisms of silver-based low-e coatings found in the literature.

The third chapter, Methodology, will present and guide the reader through the complete method developed to answer the aforementioned objectives of the project, from the deposition of the samples by our partner, to the preparation of the samples in-house, to the various characterization experiments that were performed. Naturally, the methodology surrounding the heat treatment procedures, and the method developed for the assessment of defect visibility will both be addressed.

The fourth chapter, Results & Discussion, will discuss the main findings derived from this work. This chapter will start with an assessment of the product sample used as a reference for this work, detailing its design and architecture as well as its optical and mechanical performance. Then, the

characterization of the created surface defects (topography, surface images) as well as the various factors influencing the defect visibility (visibility setup) will be discussed in detail.

Here, parameters affecting the visibility of surface defects between as-coated and heat-treated samples will be separated into three categories:

1. **Impact of the heat treatment:** The heat treatment duration will be discussed and analyzed in correspondence to their effect on defect visibility.
2. **Impact of sample storage:** A comparison of the defect visibility between samples stored in different environments prior to their HT (vacuum vs. humidity) will be presented as well.
3. **Design considerations:** The use of slightly modified coatings will be compared to the reference product in order to isolate the role of singular layers (or a combination of layers) in the intensification and visibility of HT surface defects.

The fifth chapter, General Discussion will provide additional pertinent results as well as continue the discussion on the hypothesized models and mechanisms defined in the last chapter regarding the intensification of surface defects. Also, some additional considerations and potential factors influencing surface defect visibility will be presented.

Finally, the sixth and final chapter, Conclusion and Recommendations, will complete the discussion by restating the primary objectives and results of this work. Recommendations will be made regarding the future work to be done studying the durability and degradation of such films. Similarly, limitations and difficulties regarding some of the methodology will be stated and refinements will be proposed.



## CHAPTER 2      THEORY & LITERATURE REVIEW

As this thesis aims to define, explain, and detail physical mechanisms regarding the degradation of silver-based low-e coatings, an effort will be made, in this chapter, to firstly introduce the optical properties of low-e coatings, looking into the optical performance derived from design considerations to the inherent weakness of silver-based low-e coatings: the degradation of the Ag layer. Indeed, literature shows multiple instances of Ag degradation in low-e coatings, and typically, degradation is believed to initiate near defects. However, very little work is done on explicitly linking specific mechanical failures of the coating to particular degradation patterns in such films. In order to achieve this, a thorough understanding of durability and common degradation mechanisms of silver is required. Paired with the known mechanical performance of Ag-based low-e coatings (essentially defining which type of surface defects can be created) this review will be used as an important starting point for our analyses and discussion in future chapters.

### 2.1      Low-emissivity coatings

As mentioned in the previous chapter, the low-e coating arrangement is primarily composed of a metallic layer (ML) encapsulated between several layers, each providing specific functions to the coating. Figure 2.1 shows the generalized architecture for these coatings as well as examples of multilayer architectures of a single Ag layer and multiple Ag layer low-e coatings patented by Guardian Glass LLC showing the complexity of improved low-e coatings on glass. As seen in the subset low-e architecture a) in the figure, the typical composition of a single Ag layer low-e coating contains the metallic layer centered in the stack, a seed layer deposited below the Ag layer, barrier layers and dielectric layers. The seed layer acts as a favorable surface for the deposition of the Ag layer, creating a continuous, conductive and crystalline Ag film while the barrier layers protect the metallic layer against contamination from the substrate or the exterior environment and interdiffusion of elements present in the coating during the high-temperature heat treatments. The specificities surrounding the use of multiple Ag layers within a low-e coating as well as the detailed functions of the seed and barrier layers will be addressed further in the chapter.

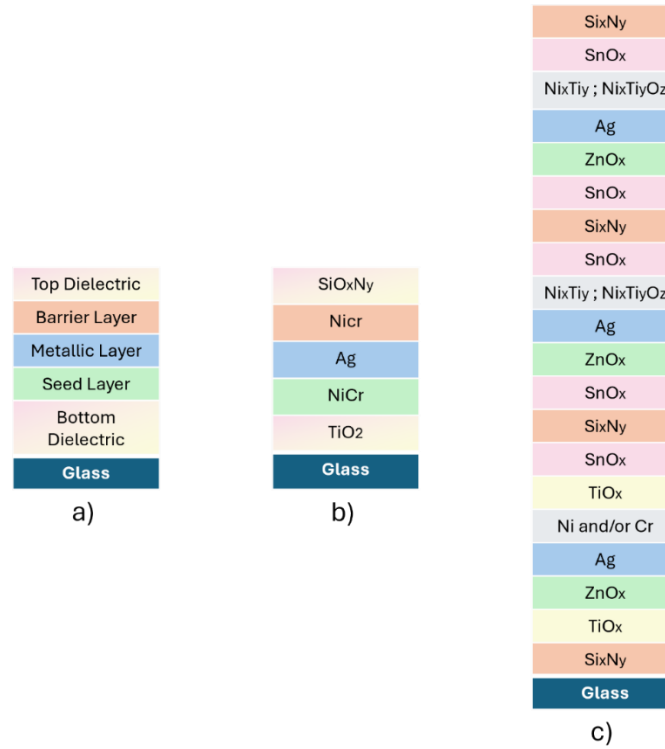


**Figure 2.1:** a) Generalized architecture of an optimized single Ag low-e coating. b) Practical example of a single Ag patented coating [20]. c) Practical example of a triple Ag patented coating [21].

As multiple barrier layers can be implemented in the architecture for protection against specific contaminations as well as multiple MLs to modify the optical response, for example, to optimize it for a specific climate (with their corresponding seed layers), one can imagine low-e architectures containing tens of layers in total totaling a few hundred nanometers in thickness, as shown in Figure 2.1c.

Moreover, typical industrial-grade low-e coatings are characterized by a few parameters such as the *U-Value* (or U-factor), the *solar heat gain coefficient* (SHGC), and the *luminous transmittance* ( $T_{Vis}$ ). The U-value defines the heat loss through the coating (usually including the spacer and the glass) and represents how well the window insulates (measured in  $W/m^2 \cdot K$ ). In colder climates, low U-values are desirable to minimize heat loss from the interior, improving energy efficiency. The *solar heat gain coefficient* (SHGC) is the ratio of the solar heat transmitted by the glass (absorbed and then reemitted) over the total incident solar energy, ranging from 0 to 1. In warmer

climates, a low SHGC is beneficial to reduce heat gain from sunlight, helping to keep interiors cooler and reducing air conditioning costs. Finally, the *luminous transmittance* ( $T_{vis}$ ) represents the portion of the visible light that the coating is transparent to and as perceived by a human observer, again ranging from 0 to 1, where higher values indicate more light transmission [7]. In spaces where natural light is desirable, such as offices or homes, higher  $T_{vis}$  values are preferred to maximize daylight while still providing insulation.

### 2.1.1 Optical Performance

The goal of low-e coatings in terms of optical performance is a maximum transmittance in the visible region paired with the control of the NIR reflectance as well as in the thermal infrared region. Slight modifications can be made to accommodate different climates, but the general idea remains the same. In fact, IR reflection as well as low-emissivity behavior can be correlated to the conductivity of the material. Emissivity, often denoted  $\varepsilon$ , describes the effectiveness of a material to emit energy as thermal radiation. In quantitative terms, it represents the ratio of thermal radiation emitted by a material to the radiation of a blackbody, an idealised physical surface that absorbs all incident electromagnetic radiation, at the same temperature. Thus, as the emissivity of a blackbody is set as 1 (ideal emitter), the ratio for other practical materials resides between 0 and 1. Based on the Drude model, which describes the optical behavior of free electrons in a solid developed in the 1900s, physicists Hagen and Rubens found that the emissivity  $\varepsilon$  (describing the thermal emission behavior) correlated with the concentration of free electrons (i.e. the conductivity,  $\sigma$ ). They derived a mathematical relation based on the Drude model linking both:

$$\varepsilon = \sqrt{\frac{8\varepsilon_0\omega}{\sigma}} \quad (1)$$

where  $\varepsilon$  is the metal's emissivity,  $\varepsilon_0$  is the permittivity of vacuum,  $\sigma$  represents the metal's conductivity, and  $\omega$  is the frequency. One can quickly deduce, that the higher the conductivity, the lower the emissivity [7]. Moreover, as thin films are involved in the production of such coatings and resistivity can easily be related to conductivity, film sheet resistance is a very important parameter when qualifying low-e coatings and products, being a relatively easy metric to measure as well.

Consequently, common noble metals (Ag, Au, Cu) that exhibit high reflectance in the thermal infrared region (and high conductivity) have been extensively used in the literature and in the industry over the years [5], [19], [22], [23]. Figure 2.2 shows a comparison of the reflectance spectra between different metals (15 nm-thick) alongside the relative solar intensity in the visible and near-infrared regions. This figure confirms the superiority of Ag and Au for optimised MLs as they exhibit the highest reflectance in the NIR. Furthermore, transmission should also be maximised in the visible region, consequently reducing adsorption and reflectance in the same region. On this matter, Fresnel's equation, in the specific case of metallic thin materials, gives the relation between the reflectance  $R$  (for both s- and p-polarized light), the refractive index  $n$  as well as the extinction coefficient  $k$ :

$$R_P = R_S = \frac{(n_0 - n_1)^2 + k_1^2}{(n_0 + n_1)^2 + k_1^2} \quad (2)$$

With  $n_0$  being the refractive index of the exterior medium and  $n_1$  and  $k_1$  respectively being the refractive index and extinction coefficient of the metallic material. It can be concluded that to maximise reflection, one needs to lower the value of  $n$  and increase the value of  $k$ , thus increasing the  $k/n$  ratio. In the case of Ag, it presents one of the highest  $k/n$  ratios (with values of 0.06 for  $n$  and 3.59 for  $k$ ), at 550 nm, compared to Cu and Au, making it the ultimate choice for an optimal ML [23]. Moreover, contrary to Cu and Au, Ag is neutral in color, favoring its use for window applications.

The second essential component when designing a low-e coating is the pairing of the Ag layer with transparent dielectric layers (DLs). These high refractive indexes ( $n$ ) DLs are chosen to adjust the transmittance properties of the full coating, ensuring the desired anti-reflective behavior for architectural glass applications. Common DLs such as ZnO, TiO<sub>2</sub>, AZO, and SnO<sub>2</sub> have frequently been used over the years [7]. Consequently, the simplest low-e design one can produce boils down to a dielectric/metal/dielectric arrangement, commonly referred to as a DMD stack.

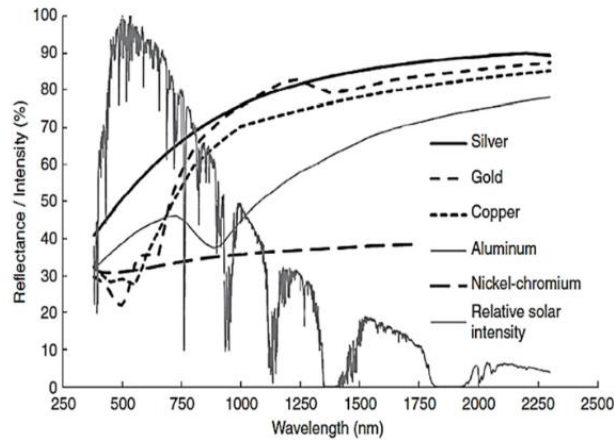


**Figure 2.2:** Reflectance of various metals with a thickness of 15 nm alongside the relative solar spectrum [19].

This encapsulation of the center ML is commonly used to improve the transmission via the top and bottom dielectrics as well as protect the Ag layer from the environment and possible contaminants. As it will be discussed and detailed further, either one of these dielectric sections in the DMD arrangement can contain multiple DLs and, similarly, the DMD sequence can be replicated (D/M/D/M/D/M...), adjusting the NIR reflectance response depending on the climate.

For now, let us begin with the simplest three-layer DMD design as shown in Figure 2.3 with the following architecture:  $\text{TiO}_2$  / Ag (11 nm) /  $\text{TiO}_2$ . The refractive index of the  $\text{TiO}_2$  layers is 2.35 (at 550 nm) with their thicknesses being optimized to maximise the luminous transmittance. The transmittance and reflectance spectra, calculated using *OpenFilters*, an open-source software for the design of interference filters, are also shown. The calculated luminous transmittance reaches 94.4% and the reflectance is seen to increase from 50% to 80% between 1100 nm and 2100 nm, in agreement with the Drude model, predicting an increase in reflectivity with a decrease in frequency (higher wavelengths).

In fact, the thickness of the ML is extremely important to maximise the optical performance, especially the visible transmission. As they are metallic layers, an increase in their thickness necessarily equates to an increase in absorption and reflectance in the visible region. Figure 2.4 shows this behavior with two figures: the first one, on the left, shows the reflection and transmission spectra for Ag films as a function of thickness ranging from 5 nm to 106 nm at 633 nm and the

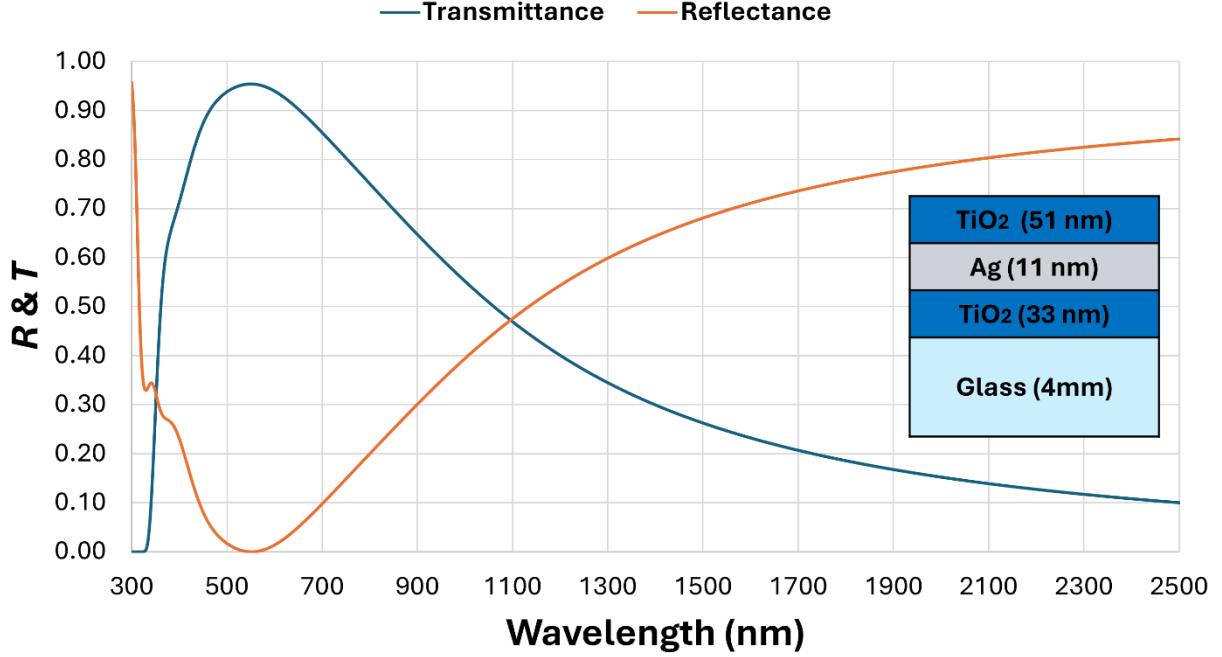


**Figure 2.3:** Simplest DMD architecture schematic (inset) and modeled  $R$  and  $T$  response for a TiO<sub>2</sub> / Ag (11 nm) / TiO<sub>2</sub> coating, using *OpenFilters*.

second one, on the right, shows the evolution of the transmittance of an AZO / Ag / AZO DMD stack as a function of Ag thickness with the AZO thickness kept constant [4], [24]. We observe, on this first plot, that the reflectance increases to 80% when the thickness exceeds 25 nm. Inversely, we observe the highest transmission at the lowest Ag thickness of 5 nm. On the second graph, we see that we achieve  $\approx 90\%$  transmission in the visible region with an Ag thickness of 10 nm (comparable to what is achieved with the previously presented TiO<sub>2</sub> / Ag / TiO<sub>2</sub> DMD stack with an Ag thickness of 11 nm). Again, when gradually increasing the Ag thickness to 40 nm, we observe a large decrease in the transmission to a value around 30%. The optical performance of Ag-based low-e coatings is ruled by the thickness of the Ag layer, with lower thicknesses allowing for a higher transmission in the visible region and broader transmission peaks.

Moreover, using multiple MLs within a single low-e coating, a higher near infrared reflectance can be achieved, while maintaining a high visible transmittance [7], [25]. Ag-based low-e designs with various numbers of Ag layers are commonly referred to in the literature as single (D/M/D), double (D/M/D/M/D), or triple (D/M/D/M/D/M/D) Ag low-e coatings, or simply, SAG, DAG, or TAG

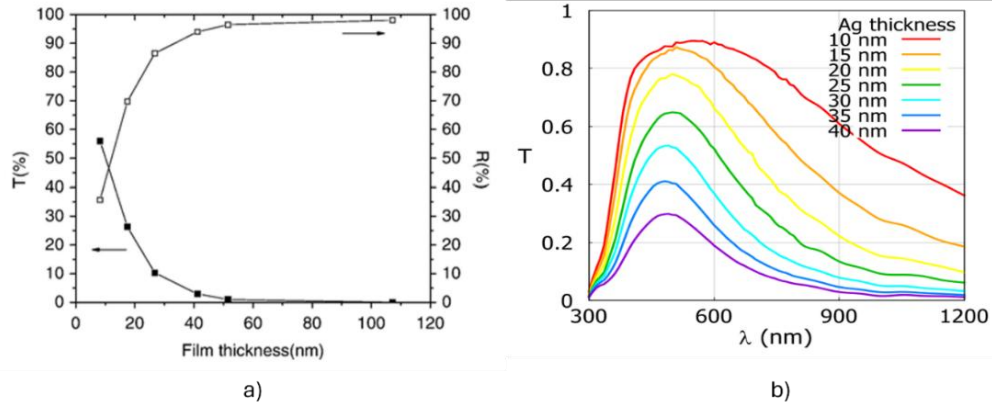


**Figure 2.4:** a) Reflection and transmission spectra for Ag films as a function of thickness ranging from 5 nm to 106 nm [24]. b) Evolution of the transmittance of a DMD stack as a function of Ag thickness ranging from 10 nm to 40 nm [4].

low-e coatings [4]. Figure 2.5 shows a representation of these low-e configurations using Ag as the MLs and AZO as the DLs on the left. On the right side of the figure, the optical response in the visible region as well as the near infrared is shown for the three configurations, where the total thickness of the Ag layers is kept at 40 nm and the thicknesses of the DLs are adjusted to maximize the overall  $T_{Vis}$ . We confirm, here again, the poorer optical performance observed in the visible region for SAG low-e coatings with the transmission capping at 30% due to the high Ag thickness. Nonetheless, comparing the different optical responses between the SAG, DAG and TAG low-e architectures, one can be convinced of the impact of the multiple ML architectures, producing a sharper rise and fall of the transmittance and increasing the reflectance selectivity in the NIR (a preferred behavior for the ideal case in warm climates, see Figure 1.2) every time we increase the number of Ag layers [7]. The visible transmittance increase observed in DAG and TAG coatings compared to SAG coatings arise from the separation of the single 40 nm-thick Ag layer into multiple thinner layers. Paired with the fact that the DLs thicknesses are optimised for  $T_{Vis}$ , this allows for a better management of the reflection in the visible region without sacrificing the reflective selectivity in the NIR. Here, the peak transmittance of the TAG architecture is inferior to the one measured for the DAG architecture, however, the wider peak for the TAG architecture makes up for its slightly lower peak intensity, ensuring higher total  $T_{Vis}$  [4].

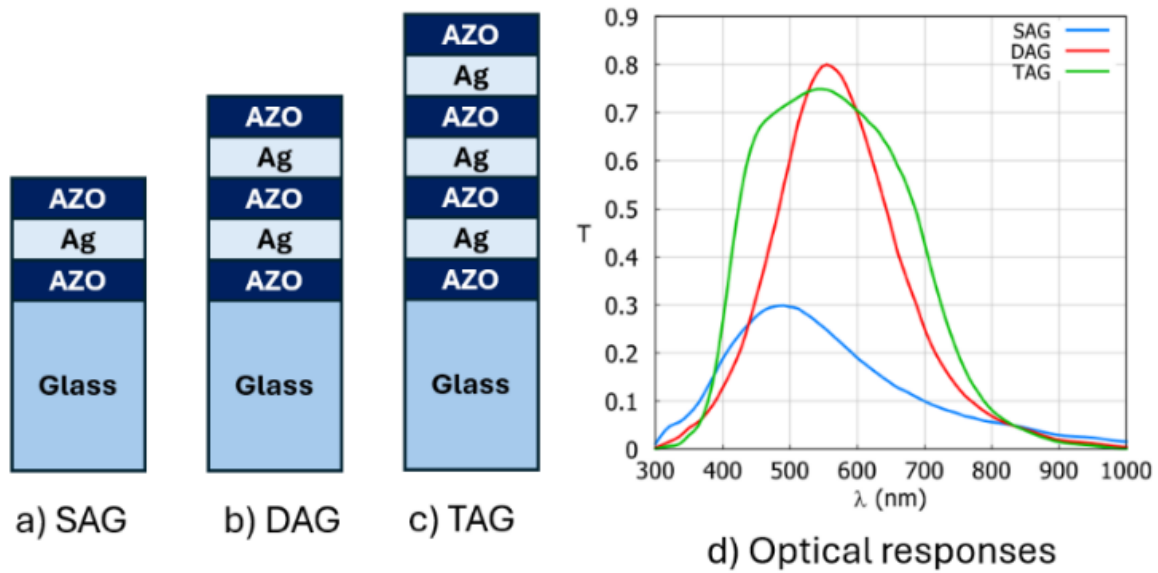


**Figure 2.5:** DMD representation of a) single, b) double and c) triple Ag low-e coating alongside d) their respective optical responses with identical total Ag thickness (40 nm) and AZO thickness adjusted to maximize  $T_{Vis}$  [4].

The core principle explaining this selectivity in NIR reflectance with the increase in the number of MLs is that each additional layer enhances the coating's ability to reflect infrared radiation. Double and triple Ag-based low-e coatings provide a better reduction in the emissivity of the coating (lower U-Values), increasing the insulation performance. Similarly, double, and triple Ag-based low-e coatings provide lower SHGC values indicating better performance in blocking unwanted solar heat, a crucial aspect of energy efficiency in cooling-dominated regions [7], [8]. Figure 2.6 shows the impact of lowering the SGHC value on the transmission spectra of low-e coatings, reminiscent of the modification from a SAG to a TAG low-e coating from Figure 2.5 [8]. As observed, a lower SGHC value (obtainable with a TAG low-e coating for example) creates a sharper decrease in transmittance after the visible region.



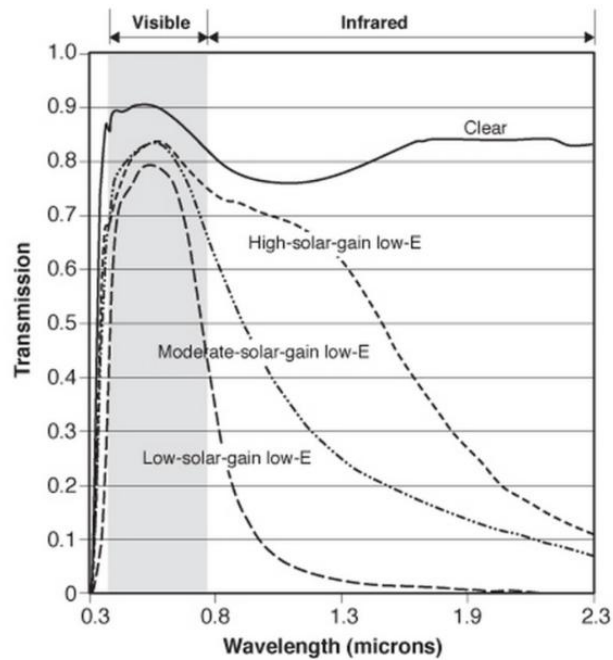


**Figure 2.6:** Transmission spectra of low-e coatings used in commercial windows [8].

### 2.1.2 Design considerations

As previously stated, efforts are made to optimize the deposition process of the Ag layer in order to achieve a smooth and conductive film. Generally speaking, for the deposition of ultra-thin metallic films, two growth modes are typically observed. The first one being the layer-by-layer growth mode (or Frank-van der Merve growth mode, FDM), where during the deposition, incoming metallic atoms will tend to bind more strongly with the underlying substrate than with themselves, creating a full layer of atoms before creating another one. This creates a thin, uniform, and conductive layer [25], [26]. Inversely, if the incoming atoms bind more with themselves than with the substrate, they will tend to grow in island-like structures that gradually increase in size over time and eventually coalesce later in the deposition process, when the percolation threshold is reached [7], [26]. This second growth mode is known as the Volmer-Weber (VW) growth mode. In fact, the percolation threshold refers to the point in the deposition process where the film is sufficiently continuous such that it becomes conductive. It is often identified when an abrupt change in conductivity (or sheet resistance) is observed. In the case of Ag, for our low-e purposes, the FDM growth mode would be favorable but not really applicable in reality due to silver's relatively high surface energy. Thus, thicker layers are required for continuous Ag films, leading

to a lower transmission, while for lower thicknesses, discontinuous Ag with island structures will lead to higher absorption and poorer electrical conductivity. The higher absorption is predominantly caused by localized surface plasmonic resonance (LSPR), where the free electrons, confined within the nanoscale islands, oscillate collectively in response to light at given resonant frequencies. It is the presence of island structures that enables LSPRs and thus, the energy absorbed by the metal during this process, increases significantly around the resonance frequency, that lead to enhanced light absorption. This effect is usually observed in the visible or NIR region, depending on the size, shape, and spacing of the islands.

The goal is then to discourage the VW growth mode, promoting layer-by-layer growth. Building on the initial DMD arrangement, the encapsulation of the Ag can then be further optimized with the addition of ultra-thin ‘seed’ layers ensuring the formation of a continuous and conductive Ag film at low thicknesses and improving the crystallinity of Ag. Figure 2.7. shows the typical island-like growth mode for the deposition of pure Ag on a SiO<sub>2</sub> substrate (without a seed layer). It is seen that, when the thickness is increased, Ag atoms diffuse along the surface, joining other Ag agglomerates. In turn, larger clusters coalesce into island-like structures, and into larger and larger formations, enabling continuity in the film. As such, seed layers are used as a way to reduce the percolation threshold during the deposition. Zn alloys, ZnO, and AZO have been used as seed layers in the industry for their high surface energy and capacity to improve the crystallinity, and thus the optoelectronic properties, of the deposited Ag [27], [28].. Ries *et al.* found that the lowest percolation threshold for Ag films was found when depositing it on ZnO, compared to NiO and Si seed layers, reported to have similar surface free energies. In the present case, the

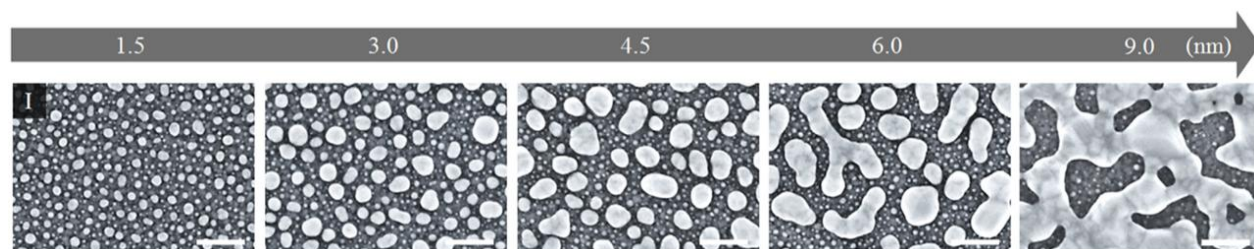


**Figure 2.7:** Planar FE-SEM images showing the morphological evolution of pure Ag, deposited on a SiO<sub>2</sub> substrate as a function of the nominal thickness. The scale bars represent 50 nm. Adapted from [29].

lowest percolation threshold was observed on ZnO at only 5 nm of Ag thickness [26], [27]. TiO<sub>2</sub>, although presenting a lower adhesion than ZnO, could also be a potential candidate for a seed layer as it has been shown to have very little orientation mismatch with Ag (110 TiO<sub>2</sub> with 111 Ag), which helps in terms of improving Ag crystallinity and quality [26], [30].

Furthermore, ‘blocking’ (or barrier) layers aim to protect the Ag from degradation resulting from multiple sources: environmental contaminants, moisture, scratches and surface defects, substrate’s contaminant diffusion and interlayer diffusion as well as protecting it from oxidation during the deposition process [5], [7], [25]. In fact, when depositing material onto the unprotected, newly formed Ag layer, the presence of possible oxygen radicals in the highly reactive sputtering process can damage the Ag layer and cause it to oxidize [31]. As the optical performance and the overall quality of the coating are heavily based on the integrity and uniformity of the Ag layer, this damage created during the deposition process can be detrimental. As such, an extremely thin blocking layer, often also metallic, is typically deposited onto the silver layer, to ensure high performance. This layer can also help block the interdiffusion within the different layers of the coating that can occur during HT. Some examples of such layers include NiTi and NiTi oxides, which have been found to generally improve the chemical and mechanical durability of low-e coatings. NiCr films have been reported as having excellent durability and thermal stability while having little impact on the optical performance when used in low-e films [25]. A Ti film, which was used as a barrier layer in a TiO<sub>2</sub> / Ti / Ag / TiO<sub>2</sub> arrangement, was found to reduce the interlayer diffusion during the annealing process (300°C for 30 minutes) [32]. As metallic layers, choosing the appropriate thicknesses of these barrier layers is an important task due to absorption considerations. Thinner layers will be fully oxidized, reducing overall adsorption, while thicker layers will remain partly metallic, increasing absorption but fully protecting the Ag film, a desirable outcome for increased durability in the coating.

Furthermore, optional overcoat or undercoat layers can be added to the overall architecture for further protection of the ML from other sources. Two common sources of contamination during the heat treatment process are, apart from internal diffusion from the coating’s own materials, Na diffusion from the soda-lime glass substrate, and O<sub>2</sub> diffusion from the environment. The barrier layers chosen to mitigate these contaminants have low permeability to these elements and thus reduce their diffusion. Good examples are Si<sub>3</sub>N<sub>4</sub> to mitigate Na diffusion or the use of overcoated

SiAlN<sub>x</sub> for blocking O<sub>2</sub>. The following sub-sections will address the various degradation mechanisms and implemented methods to ensure the durability of Ag-based low-e coatings in detail and thus will not be further discussed here.

## **2.2 Durability of silver-based low-e coatings**

As mentioned, in order to discuss the durability of Ag-based low-e coatings, one needs to touch upon the mechanical properties of such stacks after deposition as well as post-thermal annealing. As previously indicated, for thermal toughening of the glass, high temperature heat treatments going up to 700°C are required to increase the impact resistance and induce specific fracture behavior, via the rapid hardening of the glass created by quickly cooling post-HT. This technique will ensure that the glass shatters into small pebble-like pieces, rather than sharp, jagged edges. Many applications require this annealing to be performed post-deposition of the coating, meaning that the coating will also be submitted to this hostile environment. The assessment of key mechanical properties such as the hardness, the Young's modulus, and the stress levels pre-annealing helps define the fragility of the coating and its ability to intake damage. As will be discussed later, damaged regions created on the coating pre-annealing act as nucleation centers for degradation during annealing, thus, defect formation and scratch resistance are also points of interest. Finally, the degradation mechanisms of Ag and Ag-based low-e coatings, via high temperature heat treatments, the presence of moisture, and the type of annealing environment will be discussed from a literature point of view.

### **2.2.1 Mechanical properties**

It has been shown that for typical SAG low-e coatings, with thicknesses ranging between 80 nm to 150 nm, the effective hardness and Young's modulus values are mainly governed by the choice of the glass substrate. Naturally, the choice of material within the low-e stack affects the overall mechanical properties, but as their thicknesses are fairly low, their impact is much reduced. Usually, low-e coatings will always have lower effective hardness and elastic modulus than their substrate [12], [33]. Firstly, many of the materials used for the deposition of metallic, dielectric, and metal oxide layers inherently possess a lower hardness and modulus than the bulk glass substrate, especially when they are deposited at such low thicknesses, where a bulk material

typically shows higher mechanical durability than ultra-thin layers [34]. Moreover, many layers within the coating are amorphous or have a very fine crystalline structure, further leading to lower mechanical properties. Soda-lime glass, a commonly used bulk substrate for low-e products, was shown to have a hardness of 5.8–6.9 GPa as well as an elastic modulus of 72 GPa [33], [35], [36].

During the thermal annealing step, it has been shown that the hardness of SAG coatings tends to slightly increase, approaching the value of the bulk glass substrate. Figure 2.8 shows the hardness and Young's modulus as a function of the indentation depth of a SAG low-e coating, as-coated and annealed. The low-e coating in question is a stack of  $\text{MeO}_x$  (30 nm) / NiCr (3 nm) / Ag (10 nm) / NiCr (3 nm) /  $\text{MeO}_x$  (55 nm) with  $\text{MeO}_x$  being itself a stack of  $\text{SiO}_2$ , ZnO,  $\text{TiO}_2$  and SnO of varying thicknesses [12].

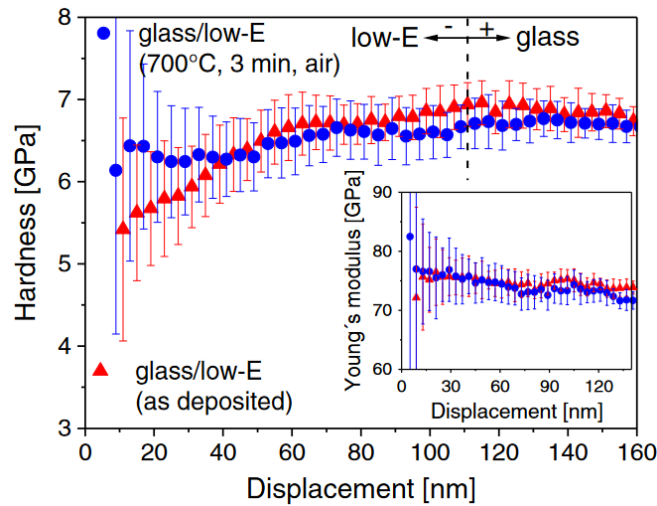


**Figure 2.8:** Apparent hardness and Young's modulus (inset) as a function of indentation depth for a low-e coating on glass before and after heat treatment at 700°C for 3 min in air [12].

As can be seen in Fig. 2.8, the total thickness of the coating is 110 nm, and when looking at hardness values for indentation depths below 110 nm for the as-deposited sample (red markers), it is seen that the values are systematically lower than the value for the glass substrate ( $\approx 6.8$  GPa here). However, looking at the same data points for the annealed sample (blue circles), the hardness values have increased and approach the hardness of the substrate with more significant changes observed further away from the substrate and closer to the sample's surface. As shown in the inset,

the Young's modulus values as a function of depth are practically unchanged when comparing the as-deposited and heat-treated samples.

Additionally, stress levels and residual stress profiles are of interest when inspecting the mechanical properties of low-e coatings. Stresses in thin films are usually separated into three categories: intrinsic, thermal, and external mechanical stress. Mechanical stresses are a result of external mechanical loading on the films, while intrinsic and thermal stresses (often both referred to as residual stresses) are a result of internal changes occurring within the stack. Intrinsic stresses in thin films are highly dependent on the deposition process and parameters, and are driven by elastic strain accommodations of the material being deposited as it bonds with its substrate [37]. Thermal stresses, however, emerge due to temperature changes when films in a multilayer coating have different coefficients of thermal expansion (CTEs) but are physically constrained by being attached to another film or substrate. It is known that for sputtered low-e coatings, high interfacial intrinsic compressive stresses are expected at the early stages of deposition from the high energy of the incoming particles and the rapid cooling of the deposited material [38], [39]. Thus, typical low-e stacks present in plane residual compressive stress in their as-coated state post-deposition, which can help mitigate defect formation and increase scratch resistance since compressive stresses help attenuate crack propagation [37].

During the annealing process, thermal stress arises. The CTEs of materials within the coatings (metals and metal oxides) are usually higher than the CTE of glass substrates [40], [41], which creates thermal stresses during annealing. During the heating phase, the coating may initially experience compressive stress as it tries to expand but is constrained by the glass. However, upon cooling, the materials contract. Since the coating has a higher CTE, it then wants to contract more than the glass. The glass, being stiffer, resists this contraction, leading to the development of tensile stresses in the coating, counterbalancing the initial compressive stress that was created upon heating. [37], [39]. This behavior is accurate only if no change in the material occurs during this heating/cooling phase. Oftentimes, phase structure changes occur in certain layers during the heat treatment causing changes in the final residual stresses of the coating post-HT. Figure 2.9 shows the parabolic deflection curves for an AC and HT (500°C, 4 min) SAG low-e coating alongside the as-received glass substrate deflection [12].

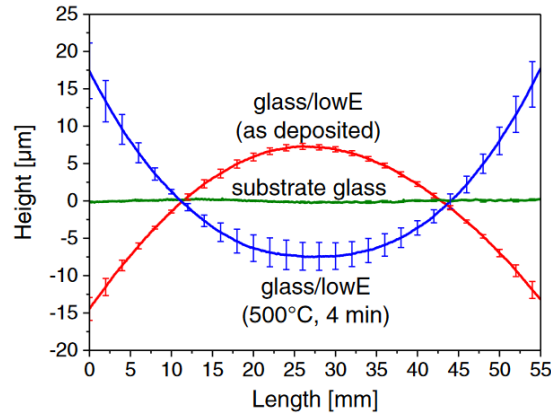


**Figure 2.9:** Parabolic deflection curves for an as-received glass substrate, an as-deposited low-e coating, and a heat-treated (500°C, 4 min) low-e coating [12].

This figure shows the overall trend of the stress transition in low-e coatings during HT, starting from a clear compressive state, with a negative deflection (red curve), to a tensile state, with a positive deflection value (blue curve). Furthermore, these stress changes might not be uniform throughout the thickness of the coating itself. Figure 2.10 shows a detailed analysis of the surface residual stress gradient as a function of depth for a TAG low-e coating of 270 nm in thickness in its AC (left) and HT (right) state from Sebastiani *et al* [37]. The method for the residual stress depth profiling used a combination of focused ion beam with digital image correlation (FIB-DIC) to measure the relaxation strain distribution of the surface area at each milling depth. With this calculation method, different percentages of the surface area were chosen to increase the sensitivity to specific layers in the coating, achieving a resolution of the stress profiling of 20 nm as well as capturing the non-equiaxial stresses (i.e. anisotropic stresses,  $\sigma_1 \neq \sigma_2$ ) usually present in multilayer coatings. Here, in the AC state, a clear non-equibiaxial compressive stress is observed at the surface of the film and remains compressive throughout the low-e's thickness. Note the comparison of the presented data with the equivalent stresses calculated from the curvature method (black markers) that shows similar results. After heat treatment, again, we see a very significant change in residual

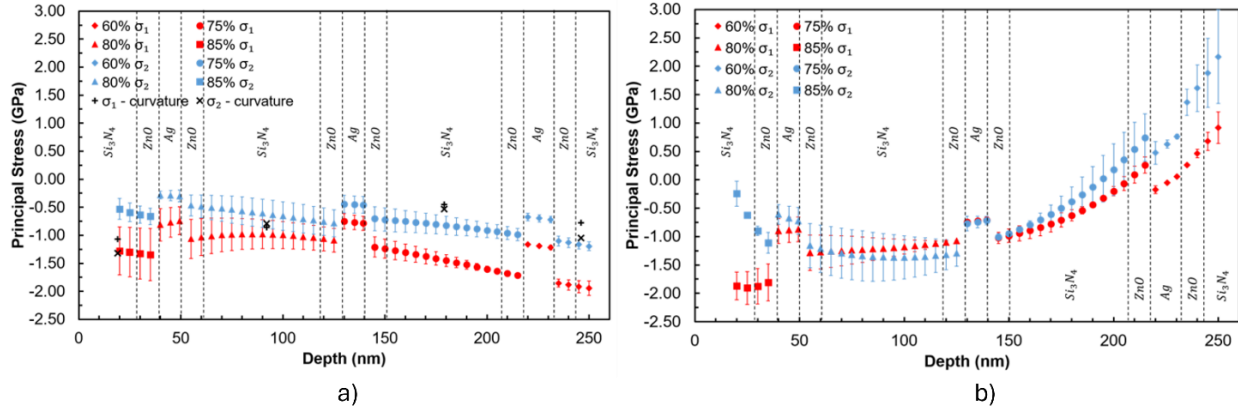


**Figure 2.10:** Principal residual stress profiles ( $\sigma_1$  and  $\sigma_2$ ) as a function of depth: (a) before heat treatment and (b) after heat treatment (540°C, 12 min) [37].

stress. The stresses become almost equibiaxial for most of the film thickness, most probably due to microstructural rearrangement and relaxation of the films following heat treatment [37]. Most notably, residual stresses become tensile near the surface as well as near the coating/substrate interface. In fact, during the heat treatment, some of the materials in the coating may undergo crystallization or changes in phase structure. These changes can alter the stress state within the coating, potentially converting compressive stress to tensile stress [5], [42]. Moreover, high temperatures can lead to stress relaxation in the coating, where pre-existing compressive stresses (due to deposition) are reduced or eliminated. In addition, atoms in the coating layers may also diffuse, or small grains may coalesce, leading to changes in density and residual stress [15], [37].

Overall, residual stresses in low-e coatings and their evolution during heat treatments are a complex system that depends on multiple parameters such as temperature, nature, and thicknesses of the coating's layers and substrate, thus, predicting the overall stress behavior and profile is a nontrivial matter. However, they are important in the sense that they can have a significant impact on the coating's integrity and its resistance to defect formation as it will be discussed in the next subsection.



### 2.2.2 Scratch resistance

The evaluation of scratch resistance of coatings is mostly a measurement of the adhesion of the coating on the substrate and an assessment of the possible damage that can occur on said coating. As different coatings have different and specific modes of damage and failure (that depend on material, thickness, and test method), one of the most difficult aspects of assessing scratch resistance is the definition and classification of the progressive damage that is observed on the coating [43]. Several researchers have provided general models and categorisations of coating damage that aim to organise the different types of observed damage. In particular, S. J. Bull's classification system, is both clear and comprehensive. He identifies four primary categories of scratch damage and correlates them with the ratio of the quasi-static hardness of the coating to that of the substrate, Figure 2.11 shows these regimes [44].

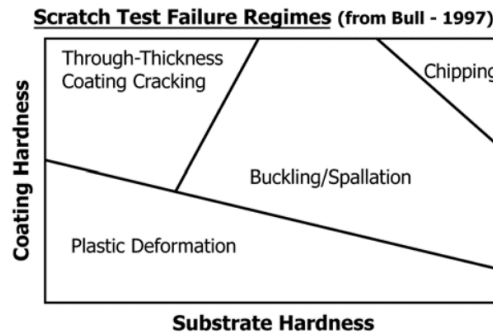


**Figure 2.11:** Scratch test failure regimes in terms of substrate and coating hardness as defined by S. J. Bull [44].

Plastic deformation, although often seen in the adhesion scratch testing of many coatings, is not typically used to define the critical scratch loads ( $L_{ci}$ ), i.e. the specific loads at which we begin to see significant damage, aiding in the quantification of scratch resistance. The other three failure regimes (through-thickness coating cracking, buckling/spallation, and chipping) are characteristic damage for critical scratch load definitions [43], [44]. As mentioned in the last section, low- $e$  coatings usually present lower hardness values than their glass substrate in their as-coated state. This combination of coating/substrate hardness value often permits the appearance of plastic deformation and through-thickness cracking followed by buckling and spalling failures in the coating undergoing progressive load scratching [43]. Plastic deformation and through-thickness cracking are cohesive failures that normally occur at lower scratching loads. Cracking is often the

result of a concentration of tensile stresses in the coating just behind the moving tip: when the tensile stress exceeds the tensile strength of the coating, it causes the material to crack. They often appear as a series of micro-cracks, some of which are semicircular, open toward the direction of the scratch, and are generated just behind the scratch tip during scratching. On the other hand, adhesive failures exhibit a behavior where the coating separates from the substrate via cracking and lifting (i.e. buckling) or by full separation (delamination, spalling, and chipping) [44], [45], [46].

Figure 2.12 shows a representation of an assignment of the critical loads  $L_{c1}$ ,  $L_{c2}$ , and  $L_{c3}$  to the respective coating failure patterns [47]. In this case, the first critical load ( $L_{c1}$ ) was chosen to be where the first tensile crack appears during the scratch test,  $L_{c2}$  is where we first witness delamination and  $L_{c3}$ , where we see full delamination of the coating. Therefore, the critical loads represent the loads at which we see these pre-defined specific failures in the coating. It is common practice to define the  $L_{c1}$ ,  $L_{c2}$ , and  $L_{c3}$  critical loads similar to what is defined in Figure 2.12, however, it is occasionally seen that the definition of these critical loads can vary from author to author, depending on the test method, the nature of the coating and the interests of the research.

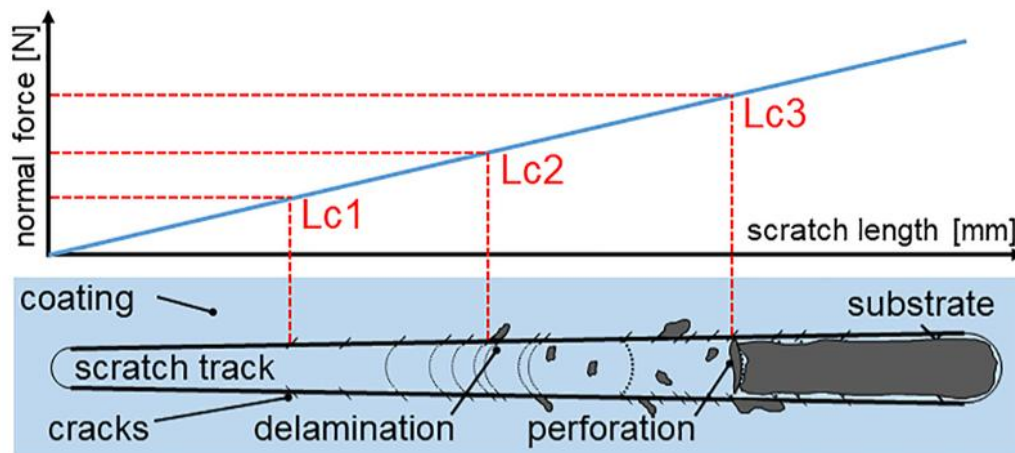


**Figure 2.12:** Schematic assignment of the critical loads  $L_{c1}$ -  $L_{c3}$  to the respective coating failure patterns [47].

It is important to note that the assessment of these critical loads evidently depends on the specific coating studied (materials and thicknesses), but also highly depends on the test method, i.e. the chosen indenter tip and load used during the scratch test experiment as these parameters greatly impact the contact stresses. Consequently, scratch resistance assessment is most accurate when comparing critical loads with similar, if not, identical tests parameters.

Most importantly, it is believed that the transition from residual compressive to residual tensile stress is responsible for the decrease in the scratch resistance following heat treatments of low-e coatings. In fact, a high tensile interfacial stress paired with strong stress gradients (both observed on heat-treated low-e coatings, see Figure 2.10) are likely to cause a significant reduction in interfacial adhesion within the coating, leading to lower scratch resistance [25], [37], [44]. Table 2.1 shows the averaged critical loads  $L_{c2}$  (first delamination) and  $L_{c3}$  (full delamination) for the TAG introduced in the previous section, taken on the as coated and heat-treated samples [37].

**Table 2.1:** Result summary of nanoscratch testing on a TAG low-e coating. Average values of 5 scratches of 100  $\mu\text{m}$  length with a progressive maximum load of 20 mN. Recreated from [37].

Sample	Critical load $L_{c2}$	Critical load $L_{c3}$
	(First delamination, mN)	(Full delamination, mN)
BEFORE heat treatment	$4.39 \pm 0.36$	$17.66 \pm 0.76$
AFTER heat treatment	$2.25 \pm 0.13$	$15.80 \pm 0.09$

In this case, 5 scratches of 100  $\mu\text{m}$  in length were made on each sample (as-coated and heat-treated) with progressive load testing (where the scratch load is increased from 0 to a pre-defined value) to a maximum load of 20 mN. The average values of the critical loads  $L_{c2}$  and  $L_{c3}$  are depicted here. The fact that both critical load values are lower for the heat-treated sample, meaning that both failure modes happen sooner in the progressive scratch tests performed on the HT sample, clearly shows the loss in scratch resistance following the HT.

### 2.2.3 Degradation mechanisms

The durability of the thin silver film remains one of the critical issues at hand when studying the degradation of low-e coatings. Its chemical reactivity, mechanical softness, and inherent vulnerability due to its extremely low thickness make it susceptible to various degradation mechanisms throughout the deposition to installation process of the final product [25], [26]. As expected, the degradation of the Ag layer leads to numerous problems such as a significant decrease in optical properties, mechanical integrity, structural integrity, and adhesion [31], [48]. This section will aim to separate these mechanisms into categories of interest for this study: Ag diffusion and agglomeration during tempering, atmospheric corrosion of Ag, and humidity-induced degradation.

First, during the heat treatment, Ag atoms diffuse and aggregate within the coating contributing to its degradation. In fact, the Ag layer will tend to dewet and rearrange into droplets of agglomerates as a means of minimizing the silver-air (or silver-encapsulant) interface [49]. More precisely, assuming a system in local thermodynamic equilibrium, the system is driven to minimize its free energy. A continuous Ag film will have a specific amount of surface energy associated with the surfaces it forms (silver-encapsulant interface, silver-air interface, etc.). Wetting, i.e. uniform spreading of the material on the substrate, will be favored if the interfacial energy is lower than the combined surface energies of the silver and substrate independently. Dewetting, however, i.e. the breaking up of the material into smaller droplets, will typically happen when the interfacial energy is not low enough to keep the film continuous [25], [26], [49]. Relating this to the previous discussion regarding the choice of the seed layer, the same behavior will determine if the deposited material completely covers the substrate before creating subsequent layers (Frank-van der Merve growth) or if it will tend to cluster into island-like structures, minimizing the surface-volume free energy ratio (Volmer-Weber growth mode). P. Jacquet *et al.* proposed an in-depth dewetting process of silver thin films separated into three distinct steps derived from real-time high-temperature *in-situ* SEM measurements of 20 nm and 40 nm Ag films heated from 25°C to 400°C [49], [50]. First, the induction step favors specific grains within the Ag film that will grow by accumulating neighboring Ag atoms. Second, the hole propagation step is observed, where surface diffusion of Ag and shrinkage of un-selected grains is observed. Finally, the sintering step, where the Ag grains slowly reach a shape closer to their equilibrium is entered. Figure 2.13 shows the beginning of the hole propagation step as well as the end of the sintering step in a comparison between two SEM mages taken on a 40 nm thick Ag layer held at 390 °C under 400 Pa of O<sub>2</sub> for

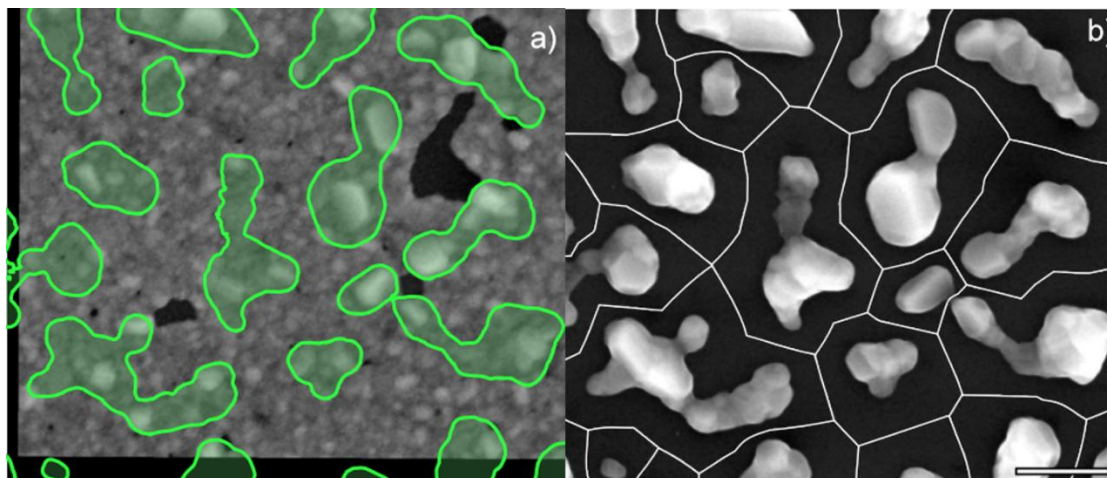


**Figure 2.13:** Comparison of two *in situ* SEM pictures: a) at the beginning of the hole propagation step. b) at the end of the sintering step. The shape of grains present in b) are superposed in green in a). Zones delimited with white lines in b) represent the ensemble of points closer to the grain inside the zone than any other grain, the so-called “zone of influence” [50]. Scale bar is 1  $\mu\text{m}$ .

40 minutes (time at which the image from Figure 2.13b was taken) [50]. The superimposition of the final grains in Figure 2.13a in green highlights the pre-existence of preferential grains at the end of the induction step. During the hole propagation step, these pre-selected grains will grow via the diffusion of Ag atoms from the unselected grains, thus creating voids surrounding the selected grains. Finally at the end of the sintering step, the clustered Ag atoms are fully agglomerated and separated from the rest. The dewetting process thus promotes agglomeration and clustering of Ag atoms with the process being accelerated at higher temperatures. This agglomeration, within the encapsulated Ag layer in low-e coatings most probably disrupts the adhesion between adjacent layers, reducing the mechanical integrity of the stack that is now more susceptible to deformation and collapse of layers following stress changes during the HT [12], [51], [52].

Furthermore, it has been shown that increasing annealing temperature increases the diffusion coefficient of Ag: Table 2.2, recreated from J. Kulczyk-Malecka *et al.* shows this effect based on Fick’s second law of diffusion solved for a  $\text{TiO}_2$  (80 nm) / Ag (10 nm) /  $\text{TiO}_2$  (80 nm) stack annealed over the temperature range of 100 to 600  $^{\circ}\text{C}$  for 5 minutes [18]. As observed, when increasing the annealing temperature from 400  $^{\circ}\text{C}$  to 600  $^{\circ}\text{C}$  the diffusion coefficient increases by

**Table 2.2:** Diffusion coefficient values calculated for TiO<sub>2</sub>/Ag/TiO<sub>2</sub> stacks annealed over the temperature range of 100 °C – 600 °C for 5 min. Recreated from J. Kulczyk-Malecka *et al.* [18]

Annealing temperature (°C)	Ag diffusion coefficient (m <sup>2</sup> s <sup>-1</sup> )
100	$3.50 \times 10^{-21}$
250	$4.25 \times 10^{-21}$
400	$5.80 \times 10^{-21}$
600	$5.93 \times 10^{-20}$

a full order of magnitude. In general, diffusion is driven by concentration gradients where the diffusion of atoms is an attempt to achieve equilibrium of the system [18], [26]. Diffusivity is both a function of temperature as well as the material (and phase of the material) it diffuses through. In this case, the linear relation between diffusion coefficient and temperature expected from an Arrhenius plot was not obtained at the highest temperatures, implying significant phase changes of the adjacent materials neighboring the Ag [18]. Indeed, a phase change was observed and is also known to occur in TiO<sub>2</sub> films from the amorphous phase to the anatase phase for annealing temperatures exceeding 400 °C, confirming that diffusivity of Ag is also highly dependent on the phase change of adjacent layers in addition to high temperatures. Consequently, the pairing of diffusion with dewetting of silver can have unfavorable repercussions in terms of the integrity of the coating. Figure 2.14 shows a combination of Ag diffusion and agglomeration alongside EDS line scans for an Ag (51 nm) / TiO<sub>2</sub> (162 nm) bilayer coating in its as-coated and heat-treated state (400 °C for 3 h) [15]. It is observed that following the HT, the bilayer system (213 nm in total) has transformed into a single-layer system (245 nm in total). The expansion of the coating as well as Ag diffusion is confirmed with the EDS spectra and clear presence of Ag nanoparticles, 10 nm to 20 nm in size, appear scattered across the coating on the SEM image. Again, it was confirmed that larger Ag nanoparticles were formed following the 500 °C HT than the 400 °C HT, corroborating the impact of the temperature on the increase of the Ag agglomeration behavior.

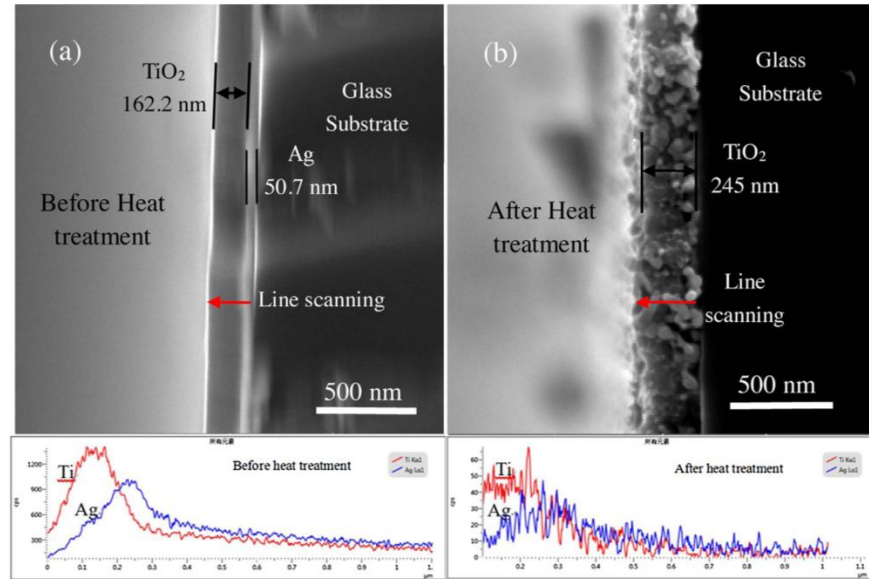


**Figure 2.14:** SEM images of Ag/TiO<sub>2</sub> nanofilms (a) before heat treatment and (b) after heat treatment with their corresponding EDS line profiles [15].

Additionally, Ag can also be susceptible to corrosion from the environment as well as humidity-induced degradation. Ag is known to react with various environmental elements which cause its corrosion, the most common being sulfur (S), chlorides, and oxygen (O) reacting with Ag producing corrosion products such as silver sulfide (Ag<sub>2</sub>S), silver chlorides (AgCl<sub>2</sub> and AgCl<sub>7</sub>) and silver oxide (Ag<sub>2</sub>O) [48], [53]. Specifically, Ag is highly sensitive to reactive oxygen that is present during subsequent deposition of oxides in reactive plasma-based processes. This reactive O<sub>2</sub> found in the deposition chamber facilitates the formation of a high-quality silver oxide when directly in contact with the newly formed silver layer, or can even partially oxidise an Ag layer that is protected with a too thin overcoat [26], [31]. In fact, in this case, the nanoscale Kirkendall effect, i.e. the interdiffusion that is observed between metals and materials via migration of adatoms and vacancies within the material, causes Ag atoms to reach the surface of the coating and degrade the film. If the Ag layer is not properly protected from the reactive oxygen, the resulting silver oxide layer has unwanted properties for low-e coating needs such as a poorer conductivity, possibly poor adhesion between the oxide layer and subsequent layers in the coating, non-uniform nature, potential higher corrosion susceptibility and increased reactivity [31]. Figure 2.15, taken from Hafezian *et al.*, shows the sheet resistance of a Ti (2 nm) / Ag (10 nm) bilayer subjected to an O<sub>2</sub>

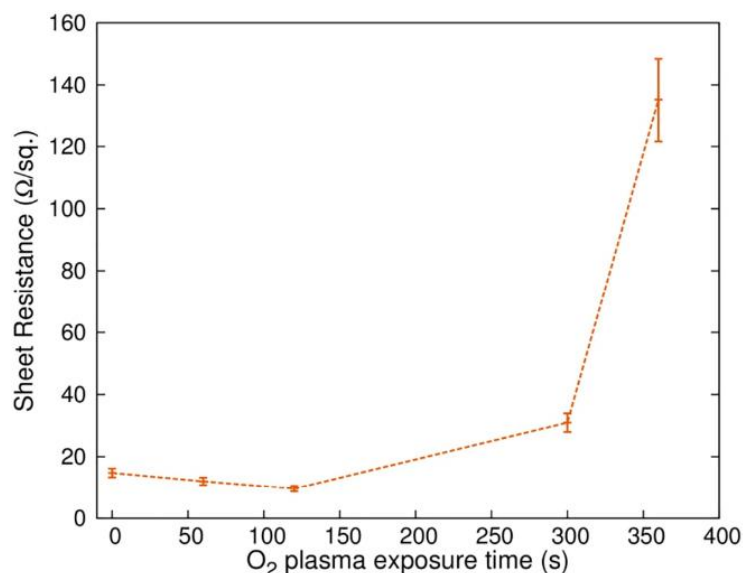


**Figure 2.15:** Sheet resistance of a Ti (2 nm) /Ag (10 nm) bilayer exposed to an O<sub>2</sub> plasma [31].

plasma exposure for up to 350 s. The figure shows an initial decrease in sheet resistance before 120 s (linked to the oxidation of the titanium barrier), but eventually, as the Ti layer becomes more and more oxidized and oxygen diffuses into the Ag layer, its degradation is quickly increased, detected with the significant decrease in conductivity (increase in sheet resistance). Moreover, atmospheric corrosion of Ag is always accelerated in the presence of moisture [51]. Water vapor sorption on Ag layers is a function of both relative humidity and temperature, where at temperatures of storage of 10 – 20 °C, a reported amount of about eight monolayers of water is present on the Ag layer when it is stored in 90 % relative humidity [48].

Silver corrosion is evidently present on nonencapsulated Ag films where the Ag is directly exposed to humidity from the environment but is also reported on encapsulated films, where degradation related to corrosion is found to begin through breaks and breaches in the film where direct contact between H<sub>2</sub>O and Ag can occur [51]. These adsorbed water layers are crucial for the corrosion mechanisms as they provide a medium for the absorption of environmental contaminants and atmospheric gases that react with the underlying Ag as well as being detrimental during the tempering process, even more so if the tempering environment is in atmospheric conditions [48], [51], [53]. The degradation of Ag-based coatings during tempering with the presence of H<sub>2</sub>O is also a result of the restructuration of Ag paired with H<sub>2</sub>O penetration [51]. The first Ag



agglomerates during the HT lead to physical discontinuities (adhesion failures) between the two neighbouring layers in the coating [12], [52]. Deformation of these layers allows for water to penetrate further along the interface to the agglomerated Ag. The separation of the layers can also be accelerated via electrochemical corrosion. For example, a Zn barrier layer has been observed to interact with H<sub>2</sub>O and Ag to produce ZnO, H<sub>2</sub>, and Ag, oxidizing the barrier layer and weakening the adhesion between itself and the Ag layer [51].

As a result, it is found that Ag degradation is essentially a function of heat treatment temperature and the Ag's direct exposure to either a humid environment or atmospheric contaminants that can lead to its corrosion, either during storage of the coating or during the tempering process [15], [18], [26]. Ag degradation manifests itself by restructuring into agglomerates and clusters as well as conversion into corrosion byproducts depending on the present reactants, both manifestations being detrimental to the efficiency of the coating. While agglomerates lead to scattering, plasmonic absorption, mechanical integrity, and adhesion issues within the different layers, corrosion reduces the optical efficiency of the Ag layer [48], [49], [50].

#### **2.2.4 Enhanced durability of Ag**

The first obvious consideration, in order to mitigate the degradation or increase the durability of Ag films, is the question of the choice of the protective layer and the seed layer: the former one being crucial in limiting O<sub>2</sub> diffusion and protecting the Ag during subsequent oxide deposition and the latter one offering a favorable substrate environment for the deposition of smooth and conductive Ag.

In addition to confirming the degradation of metal / Ag bilayer systems when exposed to reactive O<sub>2</sub>, Hafezian *et al.* also studied the impact of the seed layer on the degradation of the Ag by looking at the presence of Ag at the surface of various protective / Ag / seed layer systems, which confirm Ag diffusion through the coating [31]. When comparing three three-layered systems with SiO<sub>2</sub>, ZnO, and a monolayer of (3-mercaptopropyl) trimethoxysilane (MPTMS) as seed layers (all with a top Ti protective layer of 2 nm and an Ag ML), it was found that the two latter seed layers showed a significantly reduced amount of Ag at the surface of the samples. Similarly, both these sets of samples showed the most visible Ti2p peak from surface XPS measurements, all confirming less Ag diffusion and degradation. The choice of the ZnO metal-oxide as a seed layer was based on its

high surface energy, improving the wettability of Ag during its deposition. The lack of chemical bonding between Ag and ZnO after deposition prompted the authors to test out an MPTMS layer, creating sulfur bonds during deposition and leading to a faster coalescence of the silver nano islands and stronger adhesion [31].

In a similar fashion, the diffusivity of Ag within the stack and of Na atoms from the glass substrate during HT all can be mitigated with appropriate barrier layers, ensuring the integrity of the Ag film. Kulczyk-Malecka presented an extensive study comparing the silver and sodium diffusion coefficients through various dielectrics layers and exploring the correlation between the observed diffusion coefficients and the dielectrics' parameters such as its microstructure (controlled by the operating parameters during deposition), annealing time and temperature. It was found that Al-doped ZnO (AZO), silicon nitride ( $\text{Si}_3\text{N}_4$ ) and zinc stannate films ( $\text{Zn}_2\text{SnO}_2$ , ZTO) all provide an efficient Ag diffusion barrier layer when deposited adjacent to silver in low-e coatings showing that Ag diffusion rates through these barrier layers were two orders of magnitude lower in comparison to titanium oxide barrier layers, with AZO layers showing the lowest diffusivity [54]. These results were correlated with the fact that all three films did not show any significant structural changes during tempering while the known  $\text{TiO}_2$  structural change from amorphous to crystalline was related to the increase in Ag diffusivity. Moreover, diffusion studies on each of these films all showed that Na diffusion greatly increases with temperature, as expected, regardless of the chosen barrier layer.  $\text{Si}_3\text{N}_4$  provided the best protection against Na diffusion compared to the other tested layers. It was also found to have a barrier efficiency which was dependent on the deposition conditions where  $\text{Si}_3\text{N}_4$  films that were deposited at lower energy of incident ions and annealed post-deposition at  $650^\circ\text{C}$  showed Na diffusivity values as low as the as-deposited sample [54].

Finally, it is worth mentioning that some researchers propose to increase the durability of Ag films, and low-e coatings in general, with the doping of the Ag ML. In fact, alloying Ag with other metals is a common strategy to improve its durability: in the jewelry industry, for example, it is common practice to add small percentages of Cu, Au, Zn and Pd to the silver to improve its longevity [55], [56], [57]. Similarly, in the energy-saving applications of Ag, doping of Ag with Au was found by Ming Zhou *et al.* to improve its resistance to oxidation in comparison to pure silver [58]. Ando *et al.* found that moisture induced degradation seen in Ag-based coatings could be greatly mitigated with the addition of small amounts of Pd [59]. Similarly, small additions of Pd, Au, Cu or Nd in

Ag have also been reported by Koike *et al.* to mitigate the agglomeration of Ag when exposed to chlorides [60]. Most notoriously, regarding the mechanical durability of such coatings, Dirk *et al.* demonstrated an increase in hardness, and conductivity, on low-e coatings with Ag layers doped with Al and Cu, with  $\text{Ag}_{\text{Cu}}$  being the hardest [61]. As the mechanical properties of the Ag layer are of utmost importance when considering its scratch resistance, this doping technique could greatly improve the poor mechanical properties encountered when working with soft and ductile Ag films. A great example of improved scratch resistance on doped-Ag low-e coatings was reported by Wan Noor Sofia *et al.* when doping Ag with various amounts of Cu (10 – 30 at%). It was also found that adding Au improved the coatings' durability, with high corrosion and abrasion resistance, without compromising the optical properties of the coating [62]. Figure 2.16 shows a schematic representation of a coating scratch with qualitative critical loads paired with microscope images of scratch tests performed on pure Ag,  $\text{Ag}_{70}\text{Cu}_{30}$ , and pure Cu coatings.

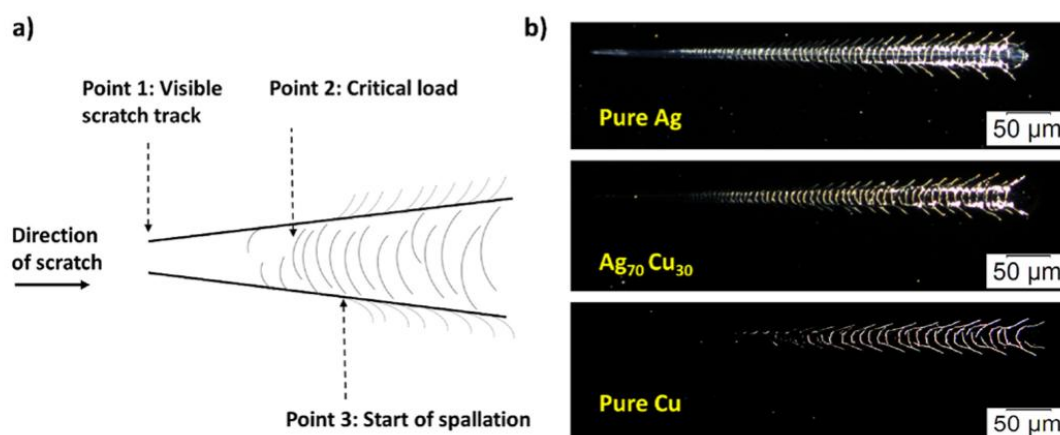


**Figure 2.16:** a) Schematic image of a coating scratch by means of arc-shaped tensile cracks and recovery spallation failure of the coating. b) Dark field microscope images for 100-nm-thick pure Ag,  $\text{Ag}_{70}\text{Cu}_{30}$ , and pure Cu films [62].

The microscope images clearly show a better scratch resistance of the doped-Ag coating compared to the pure Ag coating with the spallation failure occurring at 26 mN on the pure Ag coating versus 37 mN on the doped coating, indicating a higher adhesion of the film to the substrate. Comparing these results with the pure Cu coating (critical failure measured at 40 mN), one can be

convinced of the benefit of adding Cu to the Ag ML. In this case, the underlayer is a  $\text{TiO}_2$  layer and Cu additives are often used to increase the adhesion to oxides compared to Ag due to their passivation into  $\text{CuO}_x$  creating strong O-O bonds with the substrate, again, improving adhesion [62].

Therefore, the main way in which one can improve the overall durability of the Ag layer, as well as Ag-based coatings, is simply through the protection of said layer, either with appropriate and favorable seed layers, adequate protection from diffusion from various sources or directly altering the Ag layer in order to achieve the desired mechanical properties such as higher scratch resistance or better substrate adhesion. As one would expect, directly altering the Ag layer for increased durability will most probably alter the optoelectronic properties of the said layer, consequently modifying the optical response as well. As such, a trade-off of the optical and mechanical properties always needs to be kept in mind depending on one's desired characteristics of the overall coating.

## CHAPTER 3      METHODOLOGY

This chapter will focus on presenting the overall methodology regarding all of the experiments performed during this project. The general methodology for the assessment of scratch visibility and intensification following heat treatment (HT) goes as follows: scratch tests are performed on the sample of interest, the as-coated scratches are characterized via topography and chemical analysis techniques as well as with the visibility setup (quantifying the scratch visibility), the sample is heat-treated, and the heat-treated scratches are characterized once again. This way, a clear comparison can be drawn between what is seen on the coating in its as-coated (AC) state vs. after HT. Based on the specific conducted experiment (storing the sample pre-HT in humidity, scratching of different architectures, etc.), the intensification behavior of the surface defects can then be analysed and discussed. As such, this chapter will start with a brief presentation of the overall sample preparation, as the low-e coatings used in this project were not deposited locally. Then, mechanical characterization techniques will be addressed and, most importantly, the developed methodology to evaluate and quantify defect visibility, namely, the visibility setup and the *Python* analysis code, will be detailed here as well. Finally, complementary topography and chemical analysis techniques that were used throughout the project (SEM, EDS, XPS, etc.) as well as the specific experiments regarding the heat treatments and the storage in humidity will be presented.

### 3.1      Sample preparation

#### 3.1.1    Coating deposition

As mentioned previously, the low-e coatings used in this project were deposited industrially by our partner Guardian Glass. The goal was to use the same products that are presently being applied to buildings and that are subjected to surface defect formation and scratching during manipulation after deposition (wet cleaning brushes, automatic robotic manipulation of the glass, shipping, etc.). Deciding not to deposit these coatings ourselves allowed us to rapidly focus on the issues at hand, namely, benefiting from the fact that the optical and mechanical properties of the coatings pertained to an industrial-level while considering that the studied samples were comparable throughout the whole project, and that the response of the coatings to scratching, performed locally, would reflect what was being observed in real-life applications.

Firstly, the glass used as the substrate for the low-e coatings is typically float glass, that is made by “floating” molten glass on top of molten metal (tin). Briefly, the raw materials (a mixture of silica, soda-ash, limestone and dolomite) are molten at very high temperatures (over 1500 °C) and the molten glass ribbon (typically 3.2 m wide) floated on top of a bath of liquid tin to allow the formation of flat parallel surfaces and control the desired final thickness of the substrate (4 mm in our case) as tin is chemically unreactive with glass. The glass is then cooled and cut into large glass panes (6 m × 3.2 m) and transferred to the vacuum coating line, ready for deposition. Just before deposition of the materials, the glass substrate is cleaned with high intensity scrubbing, rinsed and air-knife-dried inside industrial washers, the large glass panes are then moved into pressure chambers creating a suitable vacuum environment for deposition.

The industrial deposition process is based on magnetron sputtering, a physical vapor deposition (PVD) technique that involves ejecting material from a target via the collision of energetic particles (ions) from a plasma with the target. The plasma is generated in the high vacuum deposition chamber by flowing in a sputtering gas (such as Ar) and applying a high voltage between the cathode (the sputtering target) and the anode (all surfaces connected to the electrical ground of the chamber). The generated electric field causes the electrons within the chamber to be accelerated to higher energies and collide with the sputtering gas atoms leading to their ionisation. The positive ions are then accelerated towards the negatively charged cathode/target, leading to collisions with the target’s surface and removal (sputtering) of the material by momentum transfer. The sputtered atoms move through the plasma and reach the substrate’s surface, where they form a coating. As the name implies, magnetron sputtering employs magnetrons that benefit from crossed magnetic and electric fields to confine the electrons near the target’s surface and enhance the ionisation rate. This gives rise to a higher plasma density thus improving the efficiency of the sputtering process and increasing the rate of deposition. The plasma can be generated in various ways, using either direct current (DC) applied to the cathode, pulsed DC, where a high voltage pulse is applied followed by a period with no voltage or alternating current (AC), continuously alternating between positive and negative voltage cycles. The way that the plasma is generated affects its properties and hence the resulting deposited film’s characteristics.

Industrial coaters are equipped with large cylindrical magnetrons and cylindrical targets (typically 4m long and 150 mm in diameter) for in-line deposition using numerous “bays”, each of them

dedicated to a specific layer. As these industrial coaters provide a continuous coating process on large substrates, the line speed, or the speed at which the substrate moves through the sputtering chamber becomes a crucial parameter in the deposition determining the deposition rate and the thickness uniformity of the coating. The coated glass is then progressively brought up to atmospheric pressure, exits the coaters, and is ready for inspection and shipping.

As a means for the reader to appreciate the substantial scale of the industrial deposition process for architectural glass glazing, additional technical details are shared here. Guardian Glass coaters expand over 100 m in length and can accommodate up to 35 different sputter bays (i.e. sub-sections of the overall coater with cylindrical magnetrons in a closed field configuration), that each contains two cylindrical targets allowing for the depositions of multiple materials and alloys. The scale of the deposition capabilities enables the coating of 3.2 m  $\times$  6.0 m float glass substrates. Equipped with multiple large industrial coaters running uninterrupted day and night around the world, Guardian Glass is able to produce 75 000 000 square meters of coated glass per year.

### **3.1.2 Preparation of samples**

The preparation of the samples in house was straightforward. The coated glass products were sent to the laboratory in various sizes (4 in  $\times$  4 in or 12 in  $\times$  12 in glass panes). The samples were then cut into 2 in  $\times$  2 in pieces to meet the requirements of the various instruments in the laboratory (sample holder for scratch testing and visibility assessment). The samples were scribed by pressing firmly along a line using a cutting wheel with a V-shape profile. The glass, now weakened, can be easily and precisely broken by applying a small pressure on both sides of the sheet using glass pliers. The glass samples were always scribed on the float side of the glass (the side that is uncoated) in an effort to protect the coated side of the glass and avoid inadvertently creating defects. The cut samples were then wrapped with a lint free tissue paper and placed in a small sample plastic bag, ready for testing. No extra cleaning steps were performed to mitigate any potential contact with the low-e coating. Whenever manipulations were required, a dry cleaning was performed with an air-knife to remove any glass or dust particles that may have been left on the sample after its manipulation.

### 3.2 Mechanical characterization

In order to discuss the defects and mechanical failure mechanisms in low-emissivity coatings, some time was spent on the mechanical characterisation of such coatings within this project. Typical mechanical properties such as hardness and Young's modulus were characterized using nanoindentation testing and, more importantly, scratch testing was performed to, on one hand, characterize the scratch resistance as well as the adhesion of the coating on the substrate and, on the other hand, produce repeatable and controllable surface defects on low-e coatings. These next two sub-sections introduce the methodologies used for scratch and indentation testing.

#### 3.2.1 Scratch tests

Scratch testing is a technique used to mechanically characterize film-substrate systems to quantify properties such as scratch resistance, adhesive and cohesive strength, friction force, elastic recovery, deformation, viscoelastic behavior, etc. The technique consists in generating a controlled scratch (controlled load, scratch mode, scratch speed, length, and indenter tip) on a sample of interest. As mentioned in Section 2.2.2, during scratch testing, the sample under study will present different failure modes depending on its composition and the applied load. By recording data on multiple physical properties during the scratch test (normal, tangential and friction forces, penetration and residual depths, acoustic noise, etc.), the instrument allows for a precise analysis post-scratch, enabling the user to define the specific critical loads  $L_{c_i}$  and, consequently, information on the scratch resistance as well as the cohesive and adhesive properties of the sample with the help of video and microscope observations. Figure 3.1 shows the schematized methodology of a scratch test with the different key controllable test parameters as well as the pre- and post-scan methodology used by the instrument to calculate key variables such as the plastic and elastic deformation, the surface profile, and the penetration and residual depths post scratching.



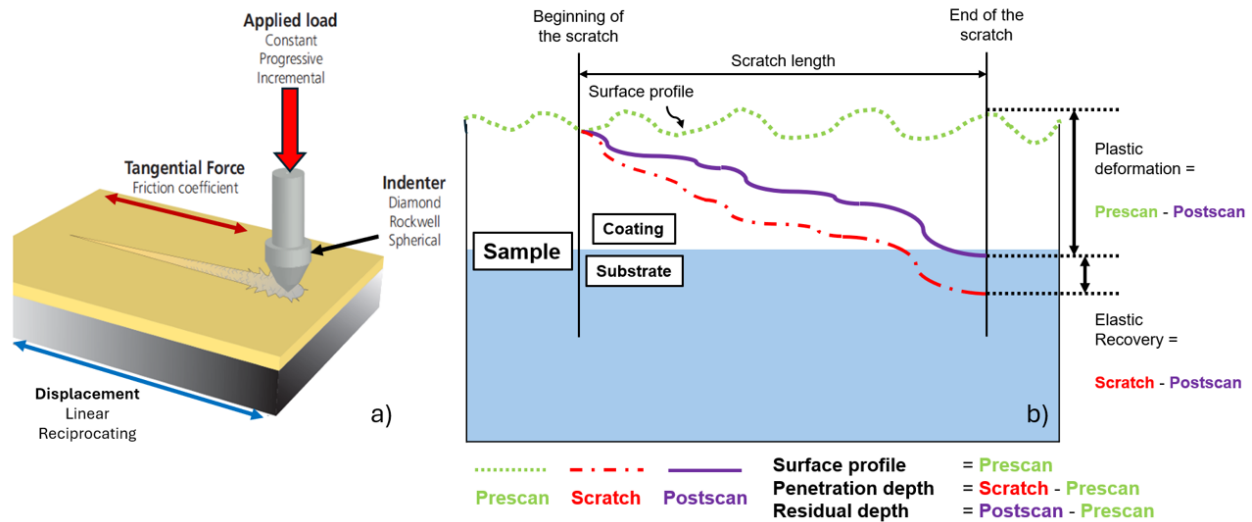


**Figure 3.1:** a) Schematic representation of a scratch test with the indenter passing over the surface of the sample, modified from [63]. The displacement and applied load can both be controlled to achieve the desired scratch morphology. b) Pre- and post-scan methodology used to calculate and derive key scratch test variables. Recreated from [64].

When trying to evaluate the scratch resistance and adhesive behavior of coatings in industry, many techniques are used, such as the brush test, consisting of a brush passing back and forth over the sample to produce multiple randomly oriented scratches, or even stylus testing, where an operator manually uses a stylus to create scratches on samples, to name a few. The brush test technique has the advantage of replicating the random conditions for scratch generation that is representative of real-life manipulation and application of these products. In our case, however, as the goal is to compare specific defects and link them to degradation mechanisms, a controllable and repeatable scratch testing approach was chosen.

More precisely, to quantify the scratch resistance of the coatings in this work, the Micro Scratch Tester (MST) from *CMS+ Instruments* was used. A Rockwell-C diamond indenter tip with a radius of 20  $\mu\text{m}$  was used with progressive load scratching (ramping of the applied load from 0 N to a defined maximum load) going up to 1.5 N with 1 mm in length (allowing the possibility to take panoramic images of the full scratch). This combination of indenter tip and maximum applied load was shown to enable the generation of multiple types of failure mechanisms such as cohesive failures (tensile cracking) as well as adhesive failures of the low-e coatings (partial and full

delamination of the coating). By doing so, specific critical loads could be defined, and the scratch resistance could be measured and compared between samples. For the analysis regarding the visibility of defects pre- and post-HT, matrices of constant load scratches were performed. The same tip was used in combination with constant load scratches (with loads ranging from 0.2 N to 0.8 N) of 1 cm in length (to be able to observe the visible scratches with the naked eye) to create a variety of scratches. The use of these constant load scratches permitted a more accurate comparison between various loads (types of failures) and degradation mechanisms in comparison to using progressive scratches where such a comparison would be more difficult.

### **3.2.2 Indentation**

Indentation testing is a widely used mechanical characterisation technique used to measure key mechanical properties such as hardness and reduced Young's modulus as well as other properties such as creep compliance, relaxation, stress-strain curves, fatigue of the material, etc. The testing consists in pressing an indenter (of known material and geometry) against the surface of the sample of interest followed by a release of the force. The corresponding load-displacement curve, measured and displayed by the instrument (plotting the normal load as a function of indentation depth), can then be used to calculate the mechanical properties of interests using calculations derived from Hertz's elastic theory between bodies in contact, and the methodology of Oliver and Pharr [65]. Figure 3.2 shows the schematic procedure for an indentation test, the corresponding geometrical parameters that can be derived from the indentation print (needed in the calculations for the mechanical properties) as well as the resulting force-displacement curve recorded by the instrument. This specific methodology is an indentation analysis method based on elastic contact theory, initially proposed by Oliver and Pharr in 1992, and is the most widely used technique in various commercial nanoindentation instruments.

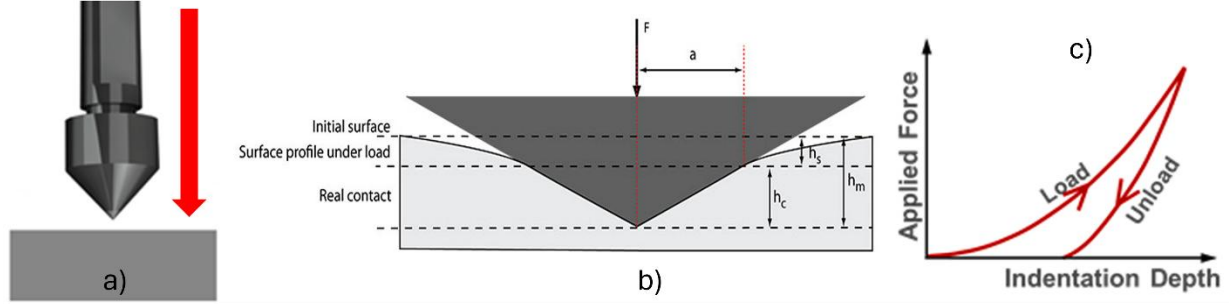


**Figure 3.2:** a) Schematic representation of an indentation test with the indenter pressing against the surface of the sample. b) Theoretical geometrical parameters derived from the indentation print used for calculations of the elastic modulus and hardness of the analysed specimen. c) Resulting load-displacement curve obtained from an indentation test.

The load-displacement curve gives information on the elasticity of the sample: for the extreme case in which the loading and unloading curves are completely superimposed, the sample presents complete elastic deformation (complete recovery of the indentation deformation). Inversely, no recovery at all (a completely vertical unloading curve) indicates complete plastic deformation. Most of the materials fall within the elasto-plastic recovery regimes, where both effects are at play as shown in Figure 3.2c. By taking the derivative of the beginning of the unloading curve, the stiffness  $S$  of the sample can be calculated. Finally, the instrumented values of the hardness  $H_{IT}$  and of the indentation modulus  $E_{IT}$  can be calculated:

$$H_{IT} = \frac{F_m}{A_p} \quad (3.1)$$

$$E_{IT} = \frac{(1 - \nu_s^2)}{\frac{1}{E_r} - \frac{(1 - \nu_i^2)}{E_i}} \quad (3.2)$$

where in the first equation,  $F_m$  refers to the known maximum force applied during the indentation test and  $A_p$  refers to the projected contact area, the area that is touching the indenter during maximum loading (proportional to  $h_c^2$  as seen in Figure 3.2b). The second equation calculates the instrumented Young's modulus, calculated from the reduced Young's modulus  $E_r$  (inversely

proportional to the square root of the projected contact area) also calculated by the instrument using contact mechanics and considering geometry. The reduced modulus inherently considers deformation of the indenter (even though it is extremely small compared to the deformation of the sample in most cases), thus is not completely representative of the modulus of the material of interest. This is why calibration of the instrument related to the system compliance, the modulus of the indenter  $E_i$  as well as the Poisson ratios of the indenter and sample,  $\nu_i$  and  $\nu_s$  respectively, are also considered in the final calculation for the instrumented, accurate modulus. The indentation experiments in this work were performed using the Hysitron TriboIndenter instrument from *Bruker* using a Berkovich diamond tip by creating three  $5 \times 5$  indentation matrices (10  $\mu\text{m}$  spacing) with loads incrementally decreasing from 2000 mN to 50 mN.

### 3.3 Heat treatments

Heat treatments of the pre-cut  $2 \text{ in} \times 2 \text{ in} \times 4 \text{ mm}$  low-e glass samples were carried out in a Barnstead Thermolyne 48000 furnace. This specific instrument was modified by Guardian Glass by adding a ZEISS spectrophotometer in order to measure and record transmission data in real-time during heat treatments. All heat treatments, unless stated otherwise, were performed at 650 °C for 12 minutes.

Heat-treating of the samples followed a specific methodology that was replicated identically for all HTs and heat protection gloves were worn at all times during the manipulations. The furnace was first preheated to 650 °C and allowed to stabilize. The sample was then placed on a custom sample holder, the oven door was opened, and the sample and sample holder were rapidly inserted into the furnace. Once the door closed, a timer was started for the desired duration of the heat treatment. Displacing the hot sample too soon after the HT or directly placing it on a cool surface may lead to the glass breaking. As such, once the desired amount of time was reached, the sample was directly removed from the furnace and allowed to cool in ambient air for 10 to 15 minutes on its sample holder. Finally, following the initial cooling phase, the sample was removed from the sample holder and placed on a Teflon mat, allowing for faster cooling (5 to 10 minutes).

Following these steps, the sample could then be manipulated safely by hand (always wearing protective gloves to prevent cuts and injuries from the sharp edges of the glass samples as well as to avoid contaminating the sample's surface) and was ready for further analyses. The customised

sample holder was designed to accommodate 4 in  $\times$  4 in glass samples, but since 2 in  $\times$  2 in samples were used in the present case, the samples were thus centered in the holder and the empty space was filled with unused soda lime glass in order to maintain a similar total mass of glass, as this was shown to impact the heat distribution on the sample during the heat treatment. Furthermore, the customised holder as well as the modified furnace ensured that the placement of the sample inside the furnace was always the same by centering the sample on the sample holder and fixing the sample holder in place inside the furnace. This ensured that the signal from the added spectrophotometer was always lined up with the sample of interest.

### **3.4 Assessment of defect visibility**

As stated previously, an important aspect of this research was to define a way to assess the visibility of various defects and quantify them. In fact, in industry, a majority of the quality control of defects on glass and coatings is often performed by a visual inspection by experts present on site who have years of experience in identifying and classifying the severity of surface defects following a given performance chart. This quality control assessment is critical in order to establish if a given batch of coatings meets performance requirements in terms of mechanical durability to be considered as a viable product. Here, focus was put on finding methods to partially automate the process and have a simpler, more objective and reliable assessment technique when it comes to the visibility of surface defects.

This next section will touch upon the development of such a technique. The implemented approach used an experimental imaging (photography) setup to take reproducible images with specific key parameters, in order to accurately compare the visibility between samples regardless of external environmental conditions. An image processing code was also developed to extract valuable metrics from the taken photos and thus quantify the scratches as well as their visibility.

#### **3.4.1 Visibility setup**

Figure 3.3 presents a schematic of the developed visibility setup with side and front views (on the left and center), and the final setup used in the laboratory (on the right). The setup is composed of

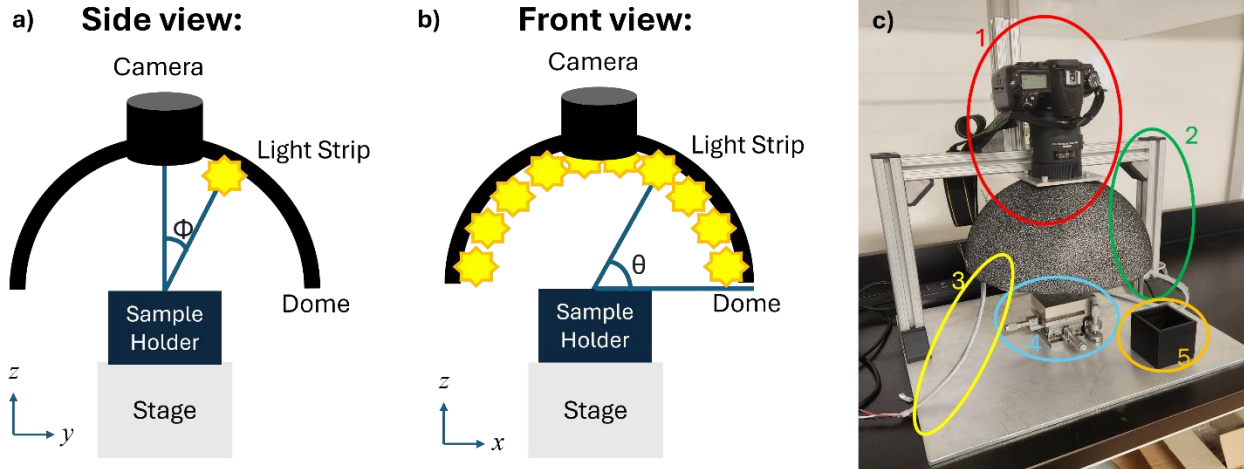


**Figure 3.3:** a) Side view and b) front view of a schematic representation of the visibility setup. c) Image of the completed visibility setup with key features. 1: Digital camera equipped with a macro lens; 2: Support bridge; 3: Light strip; 4: XYZ micrometric stage; 5: Sample holder.

a suspended digital camera fixed atop of a protective dome. The installed camera was a D7000 from Nikon equipped with a 105 mm macro lens (1) and was affixed onto an adjustable support bridge (adjustable in the  $z$  direction) (2). To control the lighting of the sample, a light strip composed of 144 LED lights was installed under the protective Styrofoam dome (3) and to control the exact position of the sample, a XYZ micrometric stage was used where the sample was placed (4). Finally, a sample holder, compatible with 2 in  $\times$  2 in glass samples, was 3D-printed and used for sample positioning (5).

The light strip installed under the dome was controlled via a *LabView* program made specifically for this task. With it, the color of the LEDs could be accurately controlled (with previously selected colors or by entering specific RGB values for a given color tint). Furthermore, the number of lit LEDs could be controlled as well as where those LED lights were lit along the strip. By doing so, multiple configurations of lighting could be achieved to obtain different images and representations of the same scratches. As seen on the Figures 3.3a and 3.3b, the  $\phi$  angle ( $\approx 30^\circ$ ) is fixed due to the way the light strip was installed so as not to cover the camera's lens, however the  $\theta$  angle could be completely controlled via the *LabView* program, offering specific illumination angles of the sample.

The camera, on the other hand, was connected to a nearby computer and could be controlled remotely. Key photo imaging parameters such as the ISO sensitivity, representing the camera's light sensitivity, the exposure time, the time span for which the camera's sensor is exposed to light and the aperture, the size of the opening of the camera's lens determining the depth of field by selecting how much light enters the camera and hits the image sensor could all be precisely controlled via the computer and a camera controlling software (in this case, the open source *digicamControl* software was used). The focus of the image could be initially adjusted directly on the camera manually and then finely tuned using the micrometric stage in the  $z$  direction.

Some additions were also made to the setup to further optimize the image taking experience. For instance, in order to eliminate most of the undesired reflections that could potentially be picked up by the camera, the interior of the dome was painted in MusuBlack, a water-based acrylic paint that can absorb up to 99.4% of visible light. Similarly, a custom and lab-deposited absorbing filter ( $\text{SiO}_2$  (88 nm) / Cr (9 nm) /  $\text{SiO}_2$  (60 nm)) was placed inside the sample holder at a 45-degree angle to absorb as much of the transmitted light as possible (up to 95% absorption in the visible region) and thus trap parasitic reflections which could make their way back to the camera sensor. Finally, various add-ons and accessories could be implemented on the camera lens for specific applications such as a polarizer to further eliminate unwanted reflections, an infrared filter to cut off the incident light in the visible spectrum and only analyze near-infrared signals as well as extension tubes which increased the spacing between the camera and the lens allowing for higher magnifications of the resulting image.

Consequently, the typical methodology for the image taking of scratches on a low-e sample consisted in first installing a clean sample on the sample holder and placing it on top of the XYZ stage. Then, with the use of the light strip and the camera control software, after adjusting the focus, one would choose the specific imaging parameters allowing for a proper assessment of the scratch visibility; for example, avoiding overly exposing the scratches. In this case, two main configurations of lighting were used.

The first one (configuration A) was to light up the 58 LEDs that were placed directly under the dome and to take images using minimal sensitivity (ISO 100 – highest signal-to-noise ratio), an aperture of f16.0 (for a high depth of field) and using exposure durations ranging from 0.5 s to 3 s depending on the sample. Usually, multiple images of the same sample were taken at different

exposure times because, naturally, once the sample is annealed, no more images can be taken of the same sample in its as-coated state. The goal here is to ensure that the analysis is made on AC and HT samples using photos taken with the same imaging parameters. This configuration is ideal for producing images with lighting coming from every angle permitting a global view of the majority of the surface defects as well as the overall appearance of the surface of the sample.

On the other hand, the second configuration (configuration B) used only a few LEDs lit at the same time (typically only 4) with different illumination angles, achieved by displacing the set of four LEDs at different positions along the light strip. By carefully choosing the position of the set of LEDs, one can calculate the angle at which the incident light of the LEDs is coming from in reference to the sample. In this manner, multiple angles of illumination (0, 30, 60, 90, 120, 150, 180 degrees) can be achieved. With this configuration, given the lesser amount of incident light, longer exposure times were needed (20 s to 30 s) to obtain usable images (with minimal ISO and f16.0 aperture as well). This configuration, especially at higher angles of illumination, highlighted scratches as most of the specular reflection was eliminated and scattered light was favored.

### 3.4.2 Image processing

As the visibility setup helped in *qualifying* the damage in the as-coated and heat-treated states, the second part of the visibility analysis consisted in running the previously taken images through a homemade *Python* code in order to perform image processing analysis and extract predefined visibility metrics that would help in the *quantification* of the defect visibility. This section will run through the main four sections of the code and detail their purpose for our analyses. The four libraries used for the code were as follows: *Pillow*, the *Python* image library, used for opening, manipulating and saving images in different formats, *NumPy*, used for multi-dimensional manipulation of arrays and matrices, *SciPy*, used for various mathematical tasks relevant in signal processing such as optimisation, linear algebra, integration, interpolation, Fourier transforms, etc. and finally, *Matplotlib*, a plotting library, essentially used in the present work as an object-oriented application programming interface (API) for plotting graphs, charts and diagrams. Note that the code is presented in its entirety in the appendix of this work.

The first section of the code consists in importing the desired image and converting the image into workable data. The 'jpg' images are imported and converted to grayscale (shades of gray) so that



every pixel in the image is assigned a value between 0 (complete black) and 255 (complete white). The grayscale images are then converted into a *NumPy* array. As a result, the value of every grayscale pixel can be read by specifying the  $x$ - $y$  coordinates of the image representing the position of the pixel. At this stage of the image processing, one can plot two initial graphs. The first one being an intensity map of the grayscale image, with the  $x$  and  $y$  axes being the  $x$  and  $y$  direction of the initial image respectively, and the intensity at every coordinate reflecting the corresponding grayscale value. The second one being the averaged intensity graph. In fact, when taking images of the scratched samples with the setup, efforts are taken to vertically align the scratches, with the use of horizontal and vertical pointers on the preview image displayed by the *digicamControl* software. Using this approach, all intense pixels are aligned in the  $y$  direction. By averaging the intensity values of the pixels in the  $y$  direction, one can plot a figure where the  $y$  axis represents these average values and the  $x$  axis, the position of the scratches. Figure 3.4. presents both graphs obtained on a typical sample. The average intensity graph on the right is the one that will be mainly used in the upcoming sections to derive quantifiable metrics for scratch visibility.

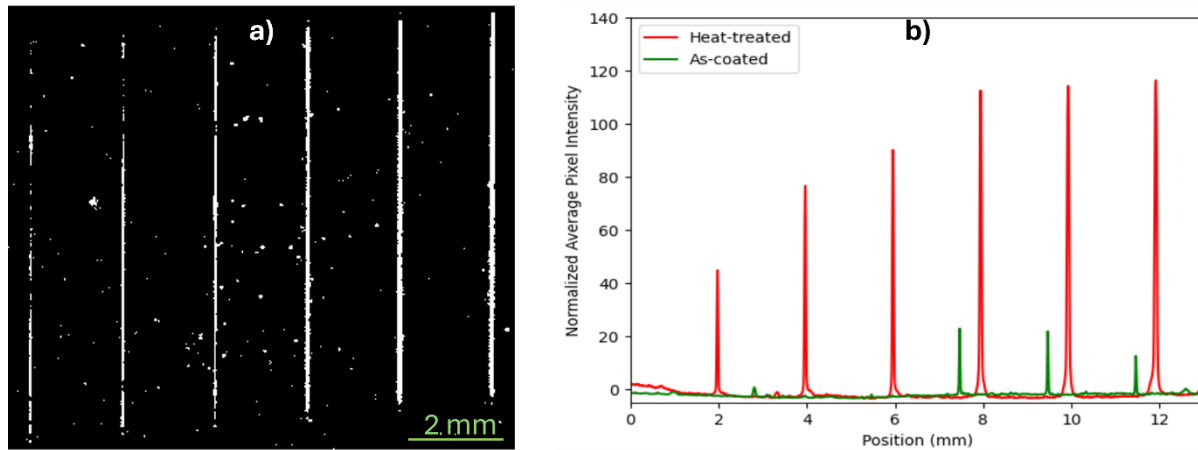


**Figure 3.4:** a) Grayscale image of a scratched and heat-treated low-e sample. b) Corresponding plot of the averaged pixel intensity (in the  $y$  direction of the original image) of the as-coated (green) and heat-treated (red) scratched low-e coating sample.

As observed and expected on the example images shown above, intense peaks are clearly visible and have significantly higher intensities than the background area of the image (the unscratched

area on the sample of interest), especially for heat-treated samples. However, the background is not always levelled and constant. In fact, artefact reflections, dust and specific image parameters such as the exposure time and the sensitivity can make it such that the unscratched area on the sample is not fully black (or does not have an intensity value of 0). This second section of the code is thus dedicated to correcting and leveling the background data to accurately compare datasets. An important note to make here is that the background data also offers valuable insight on the presence of haze, the cloudy or opaque appearance of the surface of the glass that can indicate surface contamination, manufacturing defects, degradation of the coating and presence of moisture. In some cases, the appearance of haze after the HT is very significant and a measure of the background intensity before and after heat treatment can help quantify this effect. As such, the average values of the intensities of the AC and HT backgrounds are also measured and stored. However, when trying to isolate intensity changes, i.e. the accentuation of scratches after HT, it is important to keep the AC and HT baselines constant to accurately compare and calculate the variation. As this baseline is not always constant on AC and HT images, a polynomial fit is calculated (usually of degree 3 or 4) and subtracted from the original average intensity plot so that a levelled plot is obtained. This correction can also account for slight changes to the sample and the scratch positioning.

The third section of the code includes all the calculations of the visibility metrics. The precise positions of the peaks (high intensity pixel region) are found, and the maximum average intensity values are calculated for those peaks. By subtracting this maximum intensity value of the AC sample from the maximum value of the HT sample (for the same load scratches), the first metric is calculated: the variation of peak intensity ( $\Delta PI$ ). By calculating the width in pixels of a desired peak at a given position in the peak (the full-width half-maximum (FWHM) value was used in this case), one can then convert the value in pixels to a value in microns, following a conversion from the total number of pixels in the image to an image measuring the total physical length of the same area in cm, to calculate the effective width of the scratches ( $S_w$ ). Calculations for  $\Delta S_w$  can also be performed using the same methodology as for  $\Delta PI$ . Finally, by manually creating a rectangular area surrounding a specific scratch (with the scratch always centered inside this area), and choosing a threshold intensity value, the coverage of the scratch ( $\% S_{Co}$ ) can then be obtained by calculating the ratio of the “intense pixels”, the pixels inside the area with intensity values higher than the chosen threshold, over the total number of pixels. A representation of the calculation of all relevant

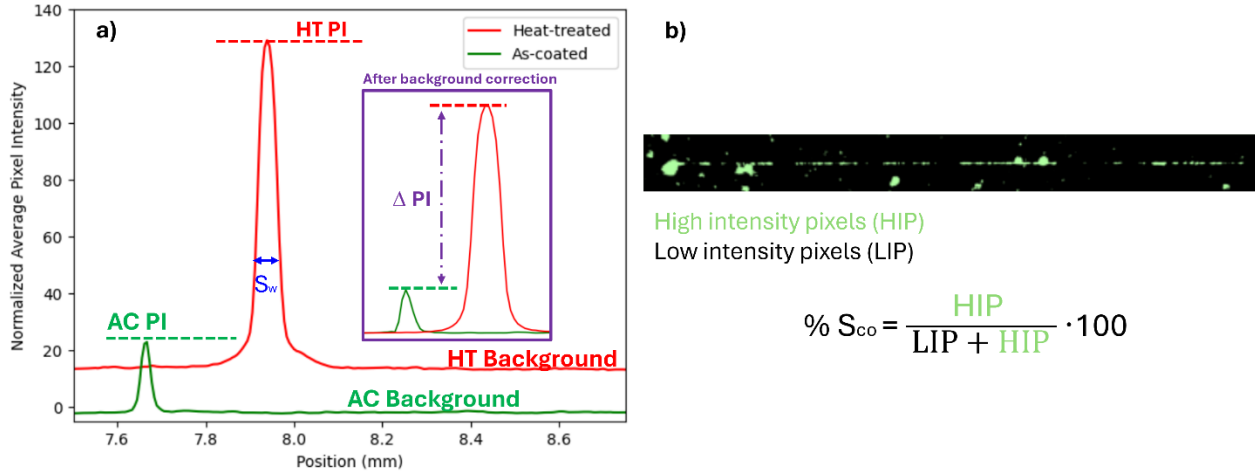


**Figure 3.5:** a) Calculation methodology of the key metrics used for scratch visibility assessment: as-coated and heat-treated peak intensity and background values (AC PI, AC Bkg, HT PI and HT Bkg), variation of peak intensity ( $\Delta PI$ ) and scratch width ( $S_w$ ). b) Calculation methodology for the percentage area of coverage of a scratch ( $\% S_{co}$ ), based on high and low intensity pixels within a predefined area.

metrics is presented in Figure 3.5.

Ultimately, the fourth and last section of the code is reserved for plotting and presentation of the desired graphs and histograms comparing these different calculated metrics between samples all at once with shifted axes to allow for easier interpretation, addition of legends, and color allocations.

### 3.5 Topography Analysis

In order to accurately characterize the morphology, depth and extent of the damage created on the low-e coatings, various topography analyses were performed throughout this work. This section will briefly introduce and contextualize the use of these characterization techniques.

#### 3.5.1 Scanning electron microscopy

Scanning electron microscopy (SEM), allows one to produce images of samples of interest via scanning the surface of a sample with a focused beam of electrons. The interaction between the

electrons from the beam atoms in the sample and provides valuable information not only on the topography and morphology present on the sample, but also its composition.

The electrons are typically thermionically emitted from an electron gun equipped with a metal filament cathode, enabling charged particles to be liberated from the surface of the metal or with the use of a field emission gun (FEG) that uses a strong electric field to extract electrons from a metallic sharp tip. These electrons are then accelerated and focused into a beam directed towards the sample of interest with the help of condenser lens; typical energies range from 1 to 30 kV with a beam size of 1-10 nm. Scanning of the specimen is achieved with a beam deflection system incorporated in the last lens of the SEM, moving the probe on the surface along a line, then to a position on the next line creating a raster scan pattern sweep. When contacting the sample, the electrons interact with its atoms at various depths and produce multiple signals that can be detected using distinct detectors. Figure 3.6 presents these various interactions and signals. Among the most important signals are the secondary electrons (SE) that are ejected electrons from the atoms within the specimen that have overcome the binding energy holding them to their respective atoms. The SE have very low energies (in the order of 50 eV) and can only escape from the top few nanometers of the sample (5 - 50 nm). They are thus highly localised at the point of impact of the beam allowing for high-resolution images ( $\approx 1 - 20$  nm). As a result, the maximum distance over which the SE can travel within the material before they lose enough energy to become trapped or are scattered is small. This indicates that only the SE that are generated very close to the surface will be able to escape and reach the detector. If the surface is rough and has a lot of steep features, fewer secondary electrons will be able to escape from deep valleys or crevices, reducing the resulting signal and creating topographical contrast in the image. The other generated signal consists in back-scattered electrons (BSE), that are electrons deflected from the nuclei of atoms in the sample by elastic scattering. They have significantly higher energies than SE, but emerge from deeper locations within the sample (50 - 300 nm) resulting in a lower resolution. As it will be discussed further in section 3.6.2, BSE are often paired with the signal coming from characteristic X-rays due to their high sensitivity to the composition of the specimen under analysis.

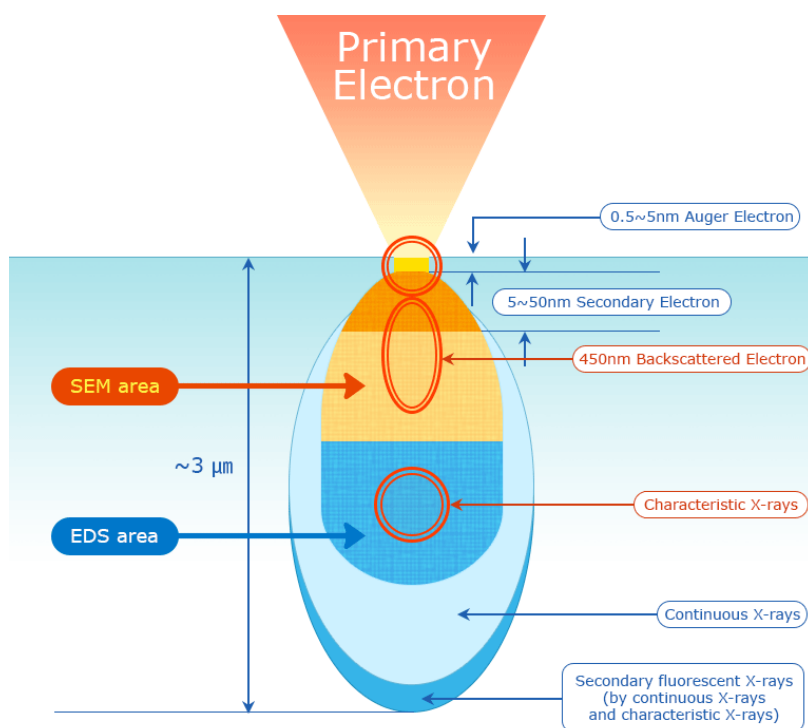


**Figure 3.6:** Various detectable signals derived from the electron-matter interactions when analyzing a specimen with a focused electron beam [66].

The instrument used was the Quattro SEM from *ThermoFisher Scientific*, permitting versatile and high resolution imagery as well as environmental capabilities such as *in-situ* heating via custom stages. The specific imaging parameters used in this work slightly vary from sample to sample in order to achieve the best possible resolution on a case-to-case basis (imaging of cross-sections very close to the electron beam, surface imaging of the morphology of the scratches, etc.). Consequently, the parameters used for imaging will be presented in parallel with the presented SEM images in Chapter 4.

### 3.5.2 Atomic force microscopy

Atomic force microscopy (AFM) is a high-resolution type of scanning probe microscopy (SPM) achieving up to atomic resolutions ( $\text{\AA}$ ), more than  $1000\times$  higher resolution than the optical diffraction limit. The topography is obtained by scanning a mechanical probe equipped with a sharp

tip at its end entering in close near-contact with the surface of the specimen. Figure 3.7 presents a schematic representation of a typical acquisition using such a technique.

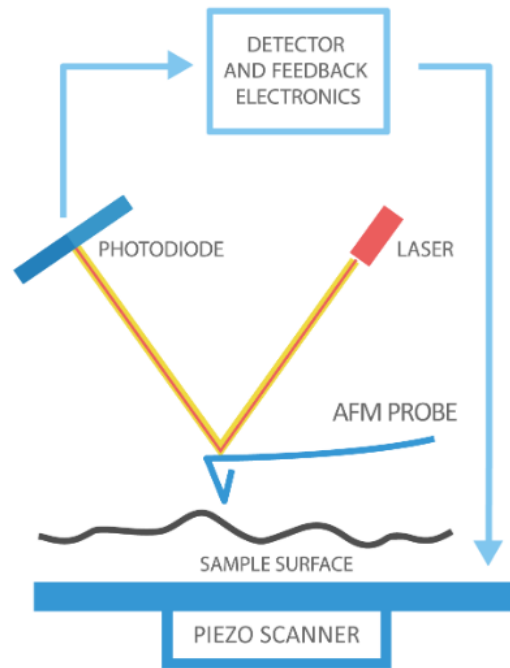


**Figure 3.7:** Schematic representation of atomic-force microscopy (AFM) [67].

The sharp tip at the very end of the probe reacts with the surface of the specimen and consequently bends the cantilever via attractive (Van der Waals and electrostatic forces) and repulsive (contact forces) interactions between the tip and the sample, depending on the operation mode. Simultaneously, the light coming from a laser that is directed toward the cantilever is redirected and collected with a photodiode. The bending of the cantilever affects the displacement of the light that is detected on the photodiode and can be linked to the corresponding displacement of the sharp tip. In the widely used contact mode, the height of the cantilever is adjusted to reset the signal and maintain a constant force between the tip and the surface that are in contact and are subject to repulsive forces, and by doing so, information on the topography of the surface of the specimen can be calculated. Therefore, with vertical and horizontal sweeping, the height of the surface inhomogeneities are arranged into a  $x$ - $y$ - $z$  topographical map.

AFM was used in this work to characterize the plastic deformation witnessed after scratching on studied samples following various constant load scratches. The experiments were carried out with the help of the Materials Characterization Laboratory (LCM) of the Université de Montréal (UdeM) with their tabletop *ICON FastScan* Bruker AFM (in static force contact mode) enabling fast and efficient AFM experiments, creating 3D mappings of nm-resolution of the deformations caused by scratching.

### **3.6 Elemental composition analysis**

Much like the techniques used for characterization of the morphology of the scratches performed on low-e coatings, elemental composition and chemical analyses were performed to identify key materials within the AC coatings and used to inspect the state of these materials after the heat treatments to confirm physical mechanisms present such as: diffusion, agglomeration, oxidation, etc. This section presents the two main techniques used in this work: X-ray photoelectron spectroscopy (XPS) and energy-dispersive X-ray spectroscopy (EDS).

#### **3.6.1 X-ray photoelectron spectroscopy**

X-ray photoelectron spectroscopy (XPS) is a surface-sensitive quantitative chemical analysis. The analysis is performed via the irradiation of the sample with an X-ray source that causes the ejection of photo-electrons from the specimen. By analysing the photoemission, three main types of chemical information can be extracted: the chemical elements, depending on the kinetic energy of the ejected electrons, the concentration of these elements, by integrating the area under the photoemission peaks, and the information on the chemical state of the elements, by analysing the relative position (chemical shift) of the photoemission peaks.

The instrument is composed of a vacuum chamber where a source of characteristic monochromatic X-rays, generated by a metal (e.g. aluminum), projects photons onto the surface of the specimen. Within the source, electrons generated from a metallic filament (from heating a metal) are accelerated towards the anode, made of a chosen metal for the generation of X-ray, and can collide with inner shell electrons of the metal atoms. Characteristic X-rays are then generated by the energy release due to the relaxation of electrons from outer to inner shells. Monochromatic X-rays (narrow

energy band of X-rays) are optimal to increase the precision of the measurement of photoelectron energies. Multilayer Bragg gratings, composed of alternating materials, act as highly selective X-ray filters such that only X-rays with the wavelength that satisfies Bragg's diffraction law at the angle used will be reflected, creating a monochromatic X-ray source. Using thus created monochromatic X-ray source, the specimen can now be irradiated and consequently release photoemitted electrons. The energy of the ejected electrons is then measured via an electron kinetic energy analyser. This analyser is typically a concentric hemispherical analyser (CHA) that allows one to measure the energy of incident electrons by assessing their radius of curvature when entering a hemispherical dome where the outer and inner hemispheres are set at different voltages. As mentioned, the main physical effect at play here is photoelectron emission. Figure 3.8 shows a summary schematic of this effect.

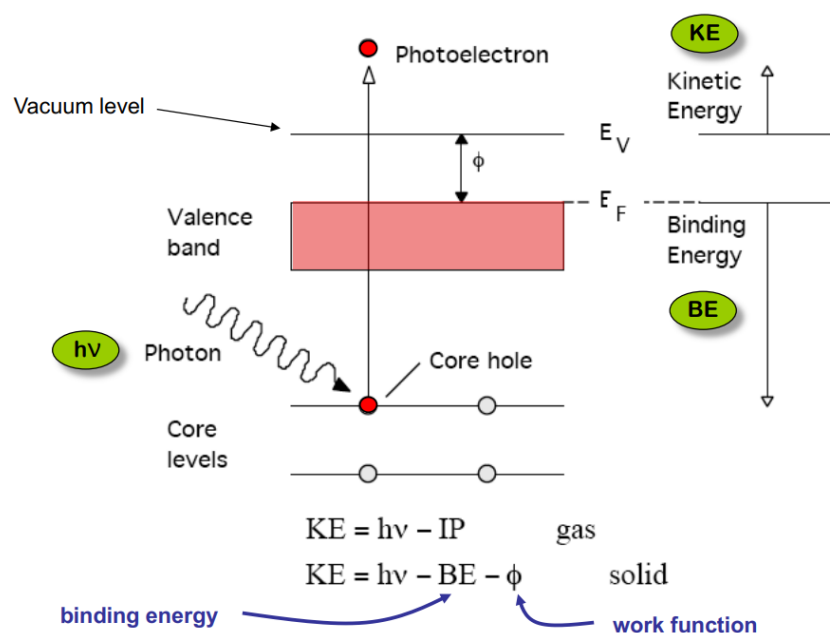


**Figure 3.8:** Schematic representation of the photoelectron emission effect [68].

Here, the photo-emitted electron, represented in red, is excited by the energy coming from the initial X-ray ( $h\nu$ ). Having obtained the kinetic energy (KE) of the emitted electron via the analyser, one can then isolate the contribution of the binding energy of the electron from the specific atom it



came from (BE). In reality, not all of the energy from the incoming photon goes into ejecting the electron, as some of it is required to overcome the material's surface potential. The contribution of the work function  $\phi$  is then also added to account for the energy needed to release the electron from the material into the vacuum. This parameter is specific to the material being analysed and is usually determined experimentally or with known values for specific elements. Therefore, the specific atoms of the specimen, known via the BE, can be found via the equation:

$$E_{Binding} = E_{Photon} - (E_{Kinetic} + \phi) \quad (3.3)$$

XPS is sensitive to the upper-most surface of the sample (top 1-10 nm) and is not effective to perform chemical analyses at higher depths. In the present case, since the aim was to chemically analyse the full 100 nm of the low-e coating, an additional step was implemented to proceed with compositional depth-profiling. In such case, an ion gun was used to sputter-etch the surface of the specimen. As each ion gun etch cycle exposes a new surface of the specimen, a new XPS spectrum was acquired to supply information on the chemical composition at each subsequent depth. The actual depth for each XPS measurement cycle is dependent on the parameters used for the ion etching and is also dependent on the specific material being etched as well. The result is a graph of the precise atomic concentrations of multiple atoms as a function of the etching rate (varying for each layer) and the chemical composition of the full low-e coating can be presented and analysed. For the XPS-depth analysis, an Escalab Xi<sup>+</sup> system from *ThermoFisher Scientific* was used. The etching was performed with an Ar monoenergetic ion source (1000 eV) on a 1.5 mm × 1.5 mm area. The X-ray source was an Al K $\alpha$  monochromator with a spot diameter of 300  $\mu$ m.

### 3.6.2 Energy-dispersive X-ray spectroscopy

Energy-dispersive X-ray spectroscopy (EDS) is a chemical analysis technique used to qualitatively and quantitatively determine which element is present on a sample of interest. With EDS, one analyses the emitted characteristic X-rays from the interaction of an electron beam with the sample. As mentioned in section 3.5.1, in SEM, the image is generated using a beam of electrons directed towards the specimen. Therefore, a significant advantage of EDS is that by adding an X-ray detector directly in the apparatus of the SEM, both measurements can be performed in tandem using the same sources and analysis area.

When the electron beam interacts with the specimen, X-rays are generated in a region of the scattered electron envelope (the effective region, where there are interactions between the incident electrons and the atoms from the sample, see Figure 3.6) for which the average electron energy exceeds the threshold energy for the excitation of X-rays. The volume of this region depends on the energy of the incident beam, the mass density of the specimen and the atomic number of the elements present in the sample. It is the excess energy of the electron transition into an inner shell of an atom that releases a characteristic X-ray, specific to the element and the particular relaxation occurring between the different K, L, M and N shells of the atom in question. The EDS X-ray detector is most often composed of a p-n junction, where incident X-photons create a number of electron-hole pairs which is proportional to the initial energy of the photon. The current generated between two gold plates is then recorded as a short pulse ( $< 1 \mu\text{s}$ ), amplified and identified according to its energy. Qualitative assessment of the chemical distribution can be made by analysing the wavelength or energy of those characteristic X-rays, and quantitative assessment is made by recording the intensity of X-rays emitted per second on the detector. False peaks can often be detected, e.g. escape peaks coming from the fluorescence of the detector, peak signal summation, when two photons arrive at the detector at the same time, etc., but these peaks are controlled and mitigated by the software via automated subtraction.

Similar to SEM imagery, EDS mapping is often used to create chemical maps of areas of interest of a sample, generating quick qualitative (distribution of elements via various colours) and quantitative (contrast between colours) images giving valuable information on its composition. Lateral resolution for EDS is, however, much lower than the one obtained with SEM. In fact, as seen in Figure 3.6, the interaction volume, region near the surface where the SE and X-rays are generated, is much larger for X-rays than for SE. The detected X-rays may be emitted from several micrometers below the surface, which means the signal originates from a larger region compared to the SE signal, leading to a lower lateral resolution. Moreover, the sensitivity to different elements is different for EDS compared to XPS and stems from the use of their complementary methodologies. The intensity of the X-ray emission depends on the atomic number ( $Z$ ) and the probability of X-ray production. As high  $Z$  elements, generally present a stronger X-ray emission, they will appear more intense in the EDS spectrum, meaning that the EDS methodology will be more sensitive to them and inversely for low  $Z$  elements. The effect of the large interaction volume will also make EDS sensitive to surface as well as bulk regions of the specimen, creating

overlapping signals from various elements in the case of multilayer thin films. For XPS, the sensitivity to lower Z elements is higher due to the binding energies of electrons in the lower orbitals being often relatively small, thus leading to a photoelectron signal easier to detect. Again, in this case, the emitted photoelectrons are generated from the top nanometers of the samples, creating a highly surface sensitive detection for XPS.

EDS was used in this work in conjunction with SEM imagery in order to retrieve chemical mapping data on areas imaged with SEM. By comparing the relative concentrations of various elements from the low-e coating, one can deduce various results from the EDS maps, for example, full delamination of the coating if the main detected element inside the scratch track are the ones present in the substrate or Ag agglomeration with the presence of small Ag clusters to name a few.

### **3.7 Additional characterization techniques**

Throughout this work, other important additional characterization techniques have also been used to further investigate the scratches performed on the low-e coatings and their evolution during HT. Among the most notable ones is the focused ion beam milling paired with transmission electron microscopy (FIB/TEM). The goal here was to create cross-sections of damaged coatings and analyze the composition and the morphology of the degraded coating at high resolution with TEM imagery. Humidity tests were performed as well to characterize the effect of the storage of the damaged coating in high humidity environments. This section presents the methodologies used for these techniques.

#### **3.7.1 Focused ion beam milling/Transmission electron microscopy**

Transmission electron microscopy (TEM) images specimens via the transmission of electrons through the sample. The main difference between the SEM and TEM arises from, the high-resolution capabilities of TEM imagery, down to the atomic levels (0.1 nm, compared to 1-10 nm for SEM), due to the limited scattering of electrons in the sample for TEM analysis, and careful preparation steps required for TEM measurements. All generated signals in TEM originate from either elastic or inelastic scattering. Elastically scattered electrons, involving no energy loss to the incident electrons stem from interactions with electron clouds from the sample, resulting in low

angle scattering and Coulombic attraction to the positively charged nuclei from the sample, resulting in high angle scattering. This scattering will occur at specific angles (Bragg angles) representative of the specimen's unique lattice spacing. As such, the resulting diffraction patterns contain information about the crystalline nature of the sample (symmetry, strain, defects). Variations in the specimen's mass and thickness will modify the amplitude of the transmitted electrons and depending on the angle at which the objective aperture is positioned, an image can be formed. In bright-field (BF) imaging, the high scattering angles are excluded creating mass-thickness contrast and inversely, in dark-field (DF) imaging, a specific Bragg angle is chosen for the position of the objective, creating a diffraction contrast. Inelastic scattering is characterised by a measurable loss in incident energy of the electron beam. Most notably, this scattering enables X-ray emission and energy-loss electrons that can be measured and analysed to characterise a number of phenomena occurring in the specimen. These include de-excitation events with X-ray spectroscopy or core-shell transitions and band structures with electron energy loss spectroscopy (EELS). In TEM, as the image is created from the interaction with transmitted electrons through the sample, the specimen is required to be extremely thin ( $\approx 100$  nm or less) to acquire adequate images. To prepare such samples, focused ion beam (FIB) milling was used in order to extract thin lamella of the sample to be used for TEM.

FIB uses a focused beam of ions at high beam currents in order to perform precise sputtering or milling of the specimen down to a nano-scale level. For our purposes, FIB was used in two scenarios. On the one hand, milling of one side of the low-e coating sample was performed by FIB operators to expose a cross-section of the coating to be analysed by SEM. By revealing a cross-section, one could observe what was occurring within the coating after scratching and after heat treatments. On the other hand, using precise procedures involving coating the surface of the low-e sample with a tungsten and carbon layer for protection, a 100 nm thick lamella was completely extracted from the original sample to be affixed to a sample holder (copper grid) for subsequent TEM observations. Thus, a cross-section of the sample was extracted to be analysed at very high-resolution giving information on the degradation occurring in AC and HT states of the coatings.

### 3.7.2 Humidity tests

In order to study the impact of moisture and humidity on the degradation of low-e coatings in this work, additional time was spent on developing a methodology for humidity storage tests. These tests involved storing the scratched samples in a humid environment prior to the heat treatment to evaluate the influence of the adsorption of water and elongated exposure to moisture on damaged coatings on defect intensification.

The coatings were stored for pre-defined amounts of time (2, 24, 48 and 96 hours) inside a glass desiccator containing a few hundreds of milliliters of water at the bottom, the water occupying approximately a third of the jar's volume. The samples were placed vertically on a rack, leaning on the side of the glass bell, with the coated side of the samples facing the center of the container. The bell was then closed with a glass cover sealing the container from the exterior environment. The humidity inside the container was measured with a TAYLOR digital humiguide and values above 90% of relative humidity were obtained. As a way of comparing the humidity stored samples with ones that were not stored in humidity, the other reference samples were placed inside a desiccator connected to the laboratory's vacuum (approximately 90 Torr, or 1.74 Psi). This was performed as the relative humidity in the laboratory could be quite significant, especially during the summer, reaching above 50% RH at room temperature.

## CHAPTER 4 RESULTS & DISCUSSION

This chapter aims to present the totality of the relevant results and experiments accomplished during this project. As stated, one of the most critical objectives of this thesis is to develop a degradation model for low-e coatings undergoing heat treatments, explaining the intensification of highly visible defects. The presented experiments stem from hypotheses of multiple parameters that could affect the visibility and the intensification of scratches during HT, namely, the duration of heat treatment, the impact of the storage environment, and the role of specific layers in the evolution of scratches.

As such, the first part of this chapter will present, in detail, the main characteristics of the low-e sample used predominantly in this project, presenting its architecture and main features as well as its mechanical properties. Secondly, we will present and analyse the specific failure modes that occur in this coating after scratching. A comparison and an introduction to the intensification of the scratches post-HT will be presented in this part as well, highlighting what is observed on damaged, heat-treated stacks on a macro-scale level with the aid of the visibility setup but also on a micro and nano-scale level using SEM and TEM images. Finally, the third and final part of this chapter will present and discuss the results of the aforementioned experiments aiming to affect the intensification of scratches in order to determine the main intervening parameters controlling its behavior.

### 4.1 Preliminary characterization

#### 4.1.1 Design & architecture

The low-e coating used in this project is referred to as the reference sample (or REF) that represents an industrial product. Figure 4.1 shows the coating architecture on the left and the corresponding XPS depth-profile spectra on the right, providing information on the relative thicknesses of the layers as well as relative concentrations of material within each layer. The Ag layer has a thickness of 11 nm, and the coating has a total thickness of 91.5 nm. The color code used in the XPS plot is reused in the presentation of the architecture for a simpler comparison. As detailed in Chapter 2, each layer serves specific roles; in this case, ZnO is used as a seed layer for the deposition of the Ag ML and the NiCr layer is used as a pinning layer (and protective layer) protecting Ag from

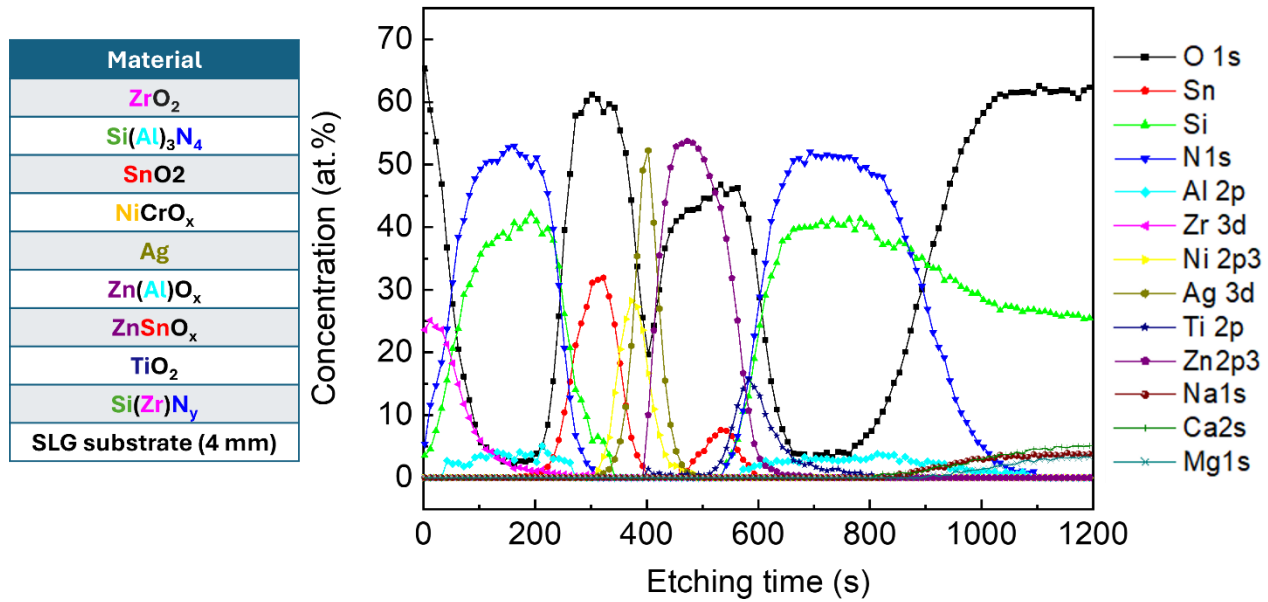


**Figure 4.1:** Architecture of the low-e coating reference sample used in this project (left) and corresponding compositional XPS depth-profiles (right).

oxidation during deposition, corrosion in air during the HT, as well as enhancing adhesion with the Ag layer and limiting Ag mobility. The  $\text{ZrO}_2$  topcoat is used to increase the scratch resistance of the coating by decreasing the COF of the surface when entering in contact with a sharp tip (a bristle of a brush or a scratch indenter tip, for example).

Experiments were carried out using different variants of architectures of this reference sample; this includes removing or changing the thickness of key layers within the reference stack. The experiments and specific architectures will be detailed in Section 4.3.3, however, for all other experiments, this reference stack has been used.

#### 4.1.1 Mechanical performance

The mechanical characterisation of the REF sample consisted in measuring the as-coated hardness ( $H$ ) and reduced modulus ( $E_r$ ) using depth-sensing indentation as presented in Section 3.2.2, as well in evaluating the scratch characteristics of the as-received coating ( $L_{Ci}$  values). Figure 4.2 shows  $H$  and  $E_r$  for the REF sample as well as for bare soda-lime glass (SLG) that was used as the substrate. Comparing this graph to the one presented in Section 2.1.2, taken on a 101-nm-thick

low-e coating, one can observe a similar trend behavior, where  $E_r$  decreases and  $H$  increases as a function of depth [12]. Here, notably higher values are obtained than what was seen in Section 2.1.2 ( $\approx 85$  GPa instead of  $\approx 75$  GPa for the  $E_r$  and  $\approx 8$  GPa instead of  $\approx 7$  GPa for the  $H$ ). Although both architectures are similar in their total thicknesses and their chosen materials, this effect can be linked to the presence of two layers of SiN (one in the topcoat and one in the bottom) that are present in the REF architecture but not in the coating from the cited article. As SiN is a ceramic material known for its high intrinsic hardness, stiffness, and resistance to deformation (both increasing the elastic modulus), both layers are expected to increase the  $H$  and  $E$  values of the coating as a whole. The use of SiN is therefore adequate in an attempt to increase the resistance to wear or scratching. The SLG substrate presents an overall lower  $E_r$  and  $H$  values comparable to the coating. Naturally, higher  $E_r$  and  $H$  values are favorable for mechanical resistance, however, the presence of a coating deposited on the substrate can enable a number of unwanted effects when both are exposed to mechanical loading, leading to cracking and delamination.

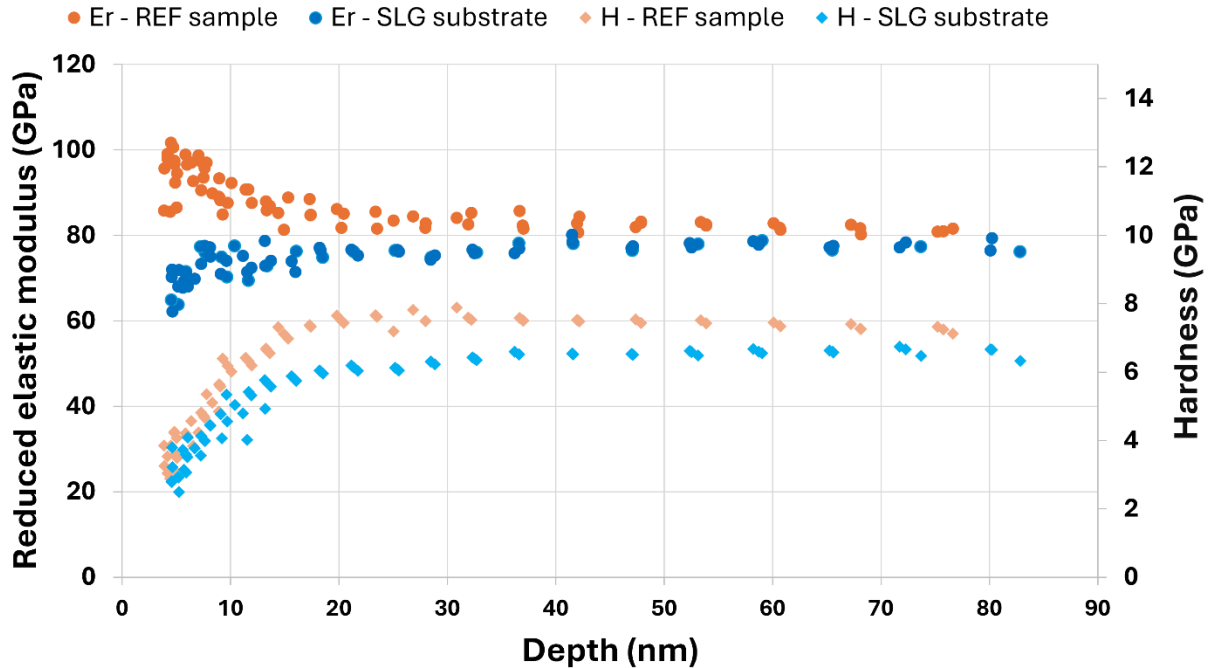


**Figure 4.2:** Measured  $E_r$  and  $H$  on a REF sample as well as on a bare SLG substrate.



The scratch resistance was evaluated with the scratch testing methodology presented in Section 3.2.1. As a reminder,  $L_{c1}$  represents the tensile cracking failure mode,  $L_{c2}$  represents the partial delamination failure and  $L_{c3}$ , indicates the full delamination of the coating. Table 4.1 summarises the results, taken on the REF sample using a forward mode of scratching (progressive loading from 0 N to 1.5 N) and a backward mode of scratching (from 1.5 N to 0 N). Forward mode scratching leads to a high standard deviation witnessed for the  $L_{c3}$  failure mode compared to the other two failure modes, reaching nearly 25% of the recorded value. This indicates that the beginning of the total delamination of the coating is irregular and less reproducible than the first occurrence of tensile cracking or partial delamination, which appear quite consistent throughout more than the 20 performed scratches. Thomas Poirié *et al.* suggested, when studying the influence of internal stress in optical films on their failure modes, that this variable behavior seen in  $L_{c3}$  characterization stems from the dependence of the delamination of the coating to the presence of small surface defects in front of the scratch tip [69]. In fact, *in situ* observations from the article showed that the failure starts far in front of the tip by a cohesive fracture of the coating, originating at a defect site, leading to delamination (adhesive failure). As such, the first appearance of  $L_{c3}$  is anticipated to be variable depending on the presence of defects on the pristine coating. As this research found a cohesive contribution to the full delamination of the coating, which is generally due to adhesive failure, one can produce scratches in a backward

**Table 4.1:** Summary of micro scratch testing on a REF sample depicting the average and standard deviation values of the three critical loads ( $L_{ci}$ ). The scratches were performed with a Rockwell-C diamond 20  $\mu\text{m}$  indenter tip with forward (23 scratches) and backward (10 scratches) mode scratching, were 1 mm in length and produced with a maximum load of 1.5 N.

Sample	Scratch mode	$L_{c1}$ (N)	$L_{c2}$ (N)	$L_{c3}$ (N)
REF sample	Forward	$0.315 \pm 0.054$	$0.499 \pm 0.028$	$0.850 \pm 0.214$
	Backward	$0.313 \pm 0.012$	$0.523 \pm 0.084$	$0.631 \pm 0.087$

scratching mode, allowing one to isolate the adhesion mechanism of the coating alone. As pointed out in the article, the morphology and the load at the beginning of the full delamination ( $L_{c3}$  in forward mode) is quite different than the one observed at the end of the full delamination ( $L_{c3}$  in backward mode). This result indicates that both delamination occurrences stem from different

failure modes and that the backward scratching mode removes the cohesive contribution of the delamination, as the load is regressive and no longer reliant on the present defects.

Backward mode scratches were, therefore, also performed, to isolate the adhesion contribution of the delamination and compare it to the usual forward scratching mode. Consequently, it is seen in Table 4.1 that the standard deviation of the  $LC_3$  failure mode for backward scratching is substantially lower than for forward scratching, becoming comparable to the ones recorded for the  $LC_1$  and  $LC_2$  failure modes. Moreover, the near-identical values recorded for  $LC_1$  and  $LC_2$  in each scratching mode confirm the reproducibility and precise nature of the appearance of both failure modes in the coating. This scratch resistance analysis prompted the use of constant loading (between 0.2 N and 1.2 N) in order to create scratches that presented all the different types of failure modes (cracking as well as partial and full delamination) to be analyzed post-HT of the sample.

## **4.2 Reproducing noticeable surface defects**

### **4.2.1 As-coated scratches**

As mentioned, when performing scratch tests on the studied low-e samples, various defects (cohesive and adhesive failure modes) are created and observed on the sample. Figure 4.3 shows a panoramic microscope image of a 1 mm scratch performed with progressive loading (0 N to 1 N) on the top as well as microscope and SEM images showing the micro-scale representation of the failure modes occurring at the different  $LC_i$  on the bottom.

It is seen that at the first critical load, the first appearance of tensile cracking of the coating is observed. Concentric cracks opened towards the direction of the scratch arise due to the tensile forces applied by the tip during scratching and are cohesive in the sense that they are occurring within the material (the low-e coating) itself and not in the substrate per say. At the  $LC_2$ , a higher concentration of tensile cracking is observed, expected due to the higher loading, as well as partial delamination of the layers of the coating initiating near the edges of the scratch track. Here, it is seen that the upmost surface of the coating is starting to lift and peel off from the rest of the sample. Finally, at the  $LC_3$ , significant and total delamination of the coating is observed, where most of the material from the coating has been removed from the surface.

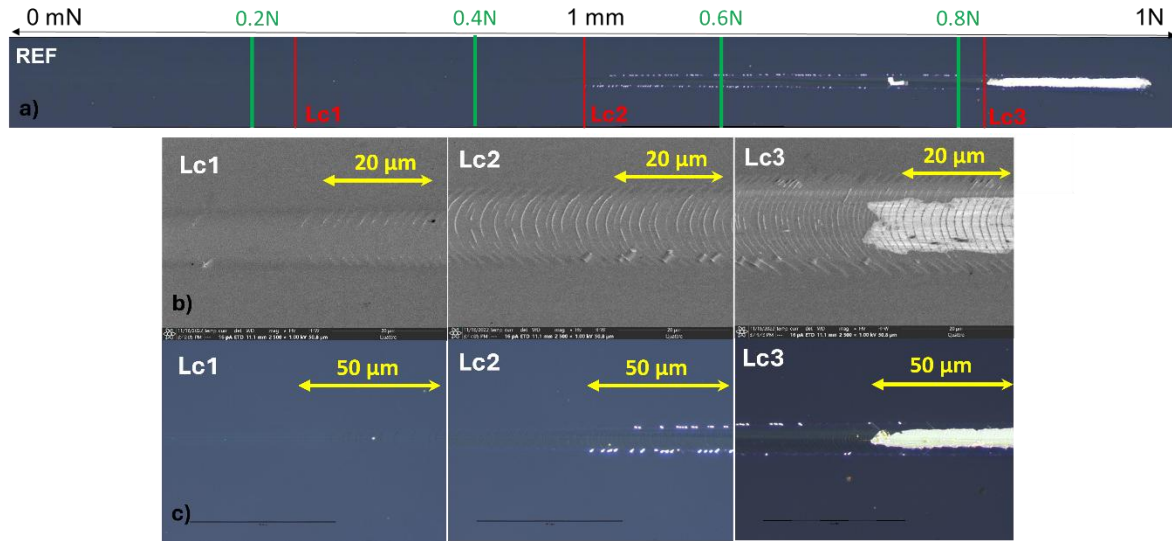


**Figure 4.3:** a) Microscope panoramic image of a progressive loading scratch (from 0 N to 1 N) with identified specific loads (in green) and critical loads (in red). b) SEM (2500× magnification) and c) microscope (500× magnification) images of the observed failure modes.

In addition to failure modes, plastic deformation of the coating is also observed. Figure 4.4 shows the plastic deformation depth of as-coated constant load scratches resulting from AFM analysis as well as 3D mappings of the morphology of a lower load scratch (0.4 N) and a higher load scratch (0.8 N). On the plastic deformation depth graph, an inset graph is shown to highlight the depth values for the lower loads. The maximum depth (in nm) for each load is also shown next to their respective curve lines. With these graphs and 3D mappings, three main observations can be made: with higher loading, scratches become wider, deeper, and show increasing pile-up at the edges of the scratch track. This behavior is consistent with the fact that stronger loading is expected to increase the area of contact of the 20 μm tip with the surface of the sample (increase in the scratch width) and apply a higher normal force on the coating (increase in maximum depth deformation) both dragging more coating material to the side of the scratching tip, increasing pile-up. TEM cross-section characterisation of high and low load scratches reveals that, at the tested loads, contrary to what may be assumed at first, the scratch tip does not penetrate the coating during scratching, but rather plastically deforms it into the substrate. Thus, the layers of the coating after scratching are deformed, conforming to the shape of the spherical diamond indenter tip. Finally,

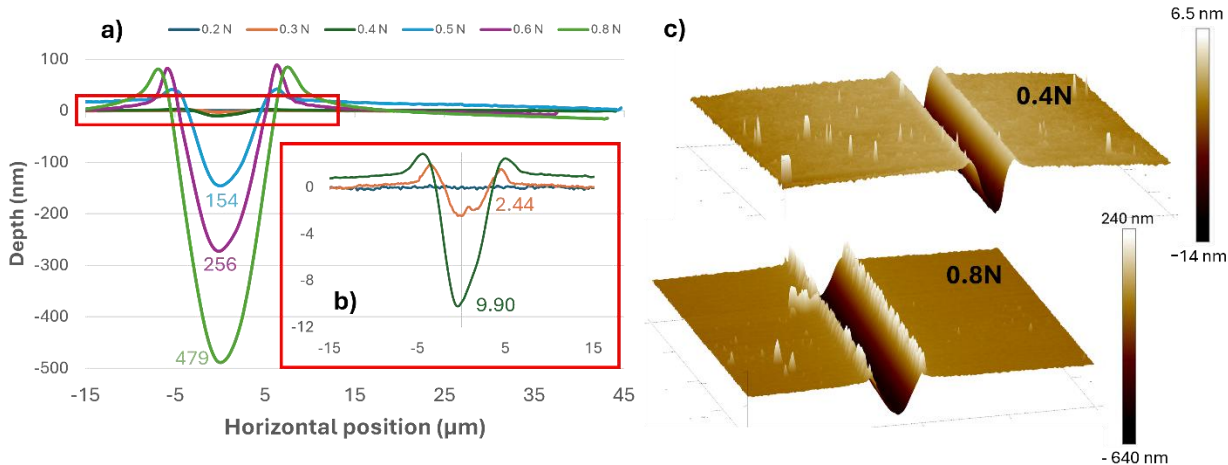


**Figure 4.4:** a) Plastic deformation depth profiles for various constant load scratches performed on a reference sample with b) inset graph representing the profiles of lower load scratches. c) AFM 3D mapping of a low load scratch (0.4 N on the top) and a higher load scratch (0.8 N on the bottom).

comparing Figures 4.4a and 4.4b reveals that the deformation present in “lower loads” (0.4 N and lower) is significantly lower than the deformation observed for “higher loads” (0.5 N and above). Here, the extent of the deformation at 0.4 N ( $\approx 10$  nm) is of the same order as the Ag layer thickness, meaning that the deformation is quite small and is not expected to notably disrupt the coating. At the highest load, 0.8 N, the maximum deformation depth is about five times the total thickness of the coating, thus the layers within the coating are expected to be significantly disrupted and deformed. With such a high deformation, adhesive failures (such as partial delamination of layers as seen with  $Lc_2$  failure modes) and weakening of the interfaces of the thin layers of the coating are expected.

From a visibility point of view, tensile cracks are completely invisible to the naked eye (and even quite faint with high magnification microscope imaging) and, thus, are undetectable by simply looking at the scratched sample. Partial delamination is detectable with microscope imaging (as seen with the white dots appearing near the scratch edges in the panoramic and microscope images of Figure 4.3) and can be detected visually with scattering of the light in reflection when tilting the sample in various directions, typically appearing as faint blue lines. Total delamination, however, given a long enough scratch (typically  $> 1$  mm), is visible with a naked eye by quick inspection of the sample and appear as bright straight white lines. Figure 4.5 demonstrates this behavior with

images taken with the visibility setup of a matrix of six 1-cm-long scratches at constant loads. The photography parameters as well as the scratch loads are presented directly in the figure. Image 4.5a was taken with the lighting configuration A (sample lit with 58 LED lights for a short period of exposure) and image 4.5b was taken with the lighting configuration B (sample lit with 4 LED lights for a longer period of exposure), both taken on the same reference sample.

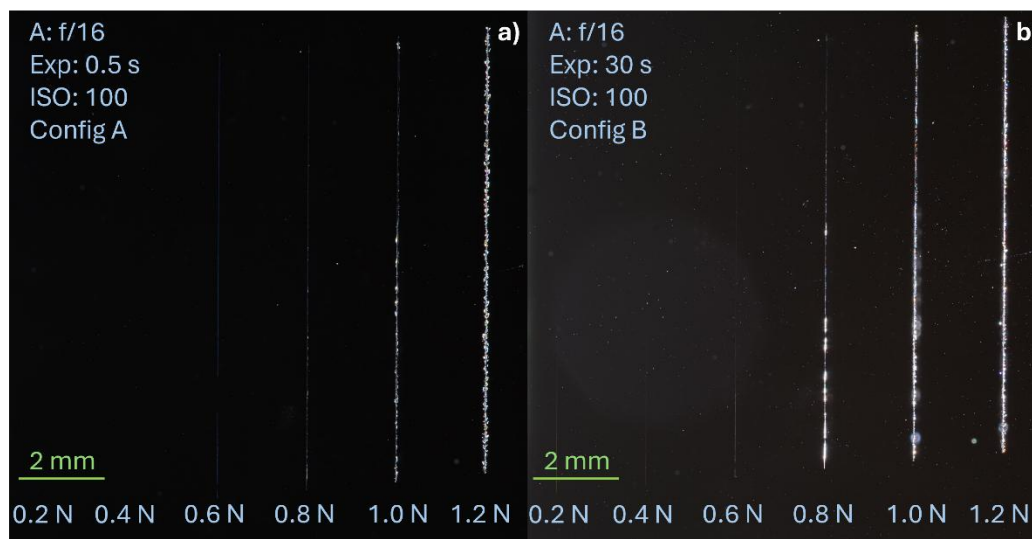


**Figure 4.5:** Visibility setup images of an as-coated, scratched reference sample (with various constant load scratches ranging from 0.2 N to 1.2 N) taken with a) lighting configuration A and b) lighting configuration B (see Section 3.4.1).

As can be seen in Figure 4.5a, at these loads, two regimes of scratches emerge. On the one hand, the lowest load (0.2 N and 0.4 N scratches in the figure) are totally invisible on the image taken with the setup. On the other hand, higher load scratches (0.6 N and above, in this case) are already visible (even if faintly) on the as-coated sample. The lighting configuration A enables a clear contrast between visible scratches as well as an even and low intensity background. However, the lowest load scratches cannot be captured using this configuration. By using high angles of illumination ( $\approx 175^\circ$  in this case) paired with less light and longer exposure times, the lowest load scratches can be revealed. This high angle configuration, however, creates noisier backgrounds, due to the longer exposure time, as well as undesirable reflections on the backside of the substrate for the analysis of the scratch visibility as seen in Figure 4.5b. For our purposes, the image taken

with configuration A is representative of the visibility of the scratches as seen visually as well as generates consistent images that can be adequately analyzed.

#### 4.2.2 Intensification following heat treatment

After performing heat treatments on the samples, the scratches become more visible. The focus was put on analyzing the intensification of scratches created with constant loads between 0.2 N and 0.8 N, highlighting the different visibility behavior witnessed for lower and higher load scratches. As the scratches of interests were the ones that presented little to no visibility in their AC state, higher load scratches (1.0 N and above) were not studied further as they were already too visible. Figure 4.6 shows the AC and HT images of the scratches taken on a reference sample. In this case, the sample was heat-treated right after the scratches were performed. Again, in the as-coated state, high loads scratches are visible (0.5 N and higher) while low load scratches are not (0.4 N and lower). Following the HT, high load scratches intensify significantly creating bright white lines, while the lower load scratches become slightly visible appearing as series of small white dots along the scratch track.

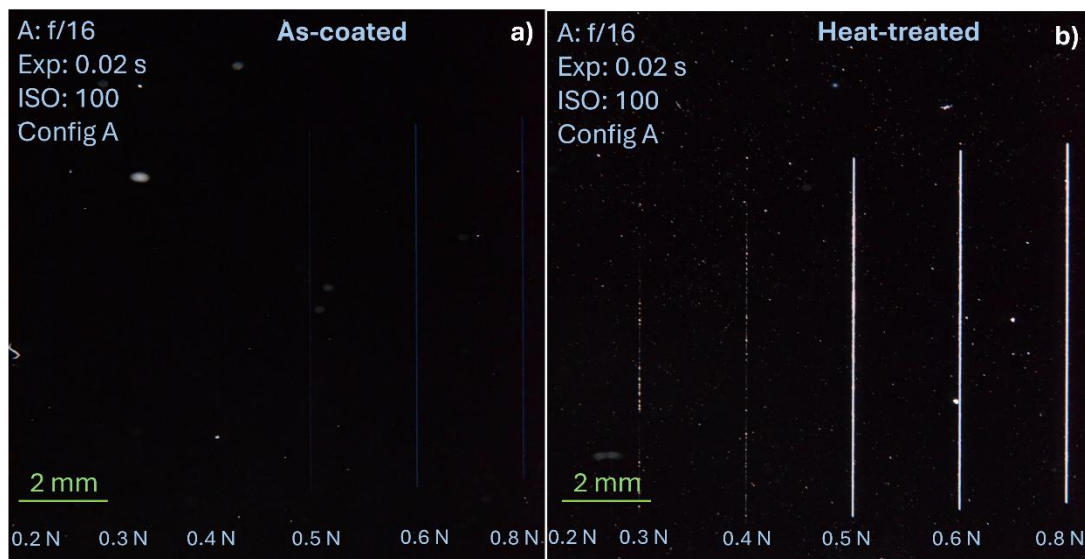


**Figure 4.6:** a) As-coated and b) heat-treated images of constant load scratches (ranging from 0.2 N to 0.8 N) taken on a reference sample with lighting configuration A.



This intensification behavior discrepancy in high and low loads was studied in more detail. Figure 4.7 shows microscope images of AC and HT scratches for a low (0.4 N) and a high (0.8 N) load. As seen on the microscope images, the edges of the scratch tracks following heat treatment appear brighter and interference fringes of various colors appear on oval-shaped morphologies. This behavior implies that the light is reflected and recombined from different travel paths hinting at a certain roughness of the surface of the HT scratch. This can indicate a variation in the thicknesses of the layer and delamination of the coating, which adds air interfaces. Between the two presented loads, the HT morphology appears similar, apart from the increased width and intensity of the higher load scratch. Looking back at the HT 0.4 N load scratch presented in Figure 4.6b, it can be seen that visible regions of the HT scratches are not uniformly distributed along the scratch track contrarily to what is seen in higher load HT scratches.

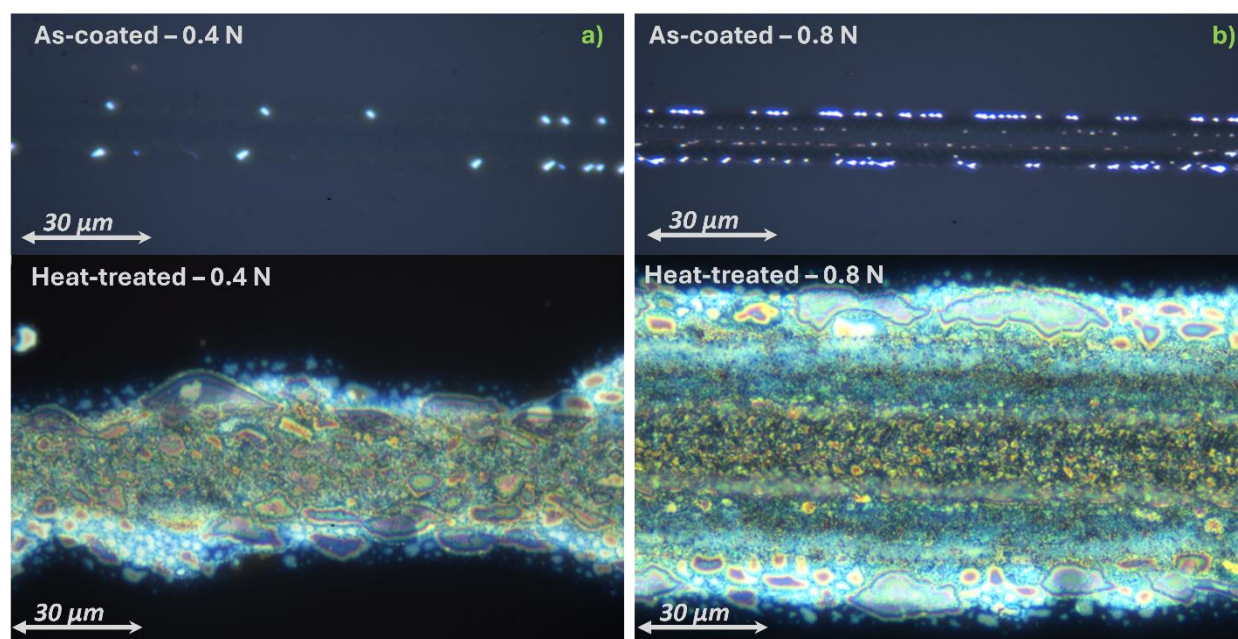


**Figure 4.7:** AC and HT microscope image (100× magnification) of a) low load scratched (0.4 N) and b) high load scratched (0.8 N) reference sample.

At a smaller scale, the degradation of the scratch track following heat treatment is clear. Figure 4.8 shows SEM and EDS mapping images (for Ag) of heat-treated scratches for a low and high loading.

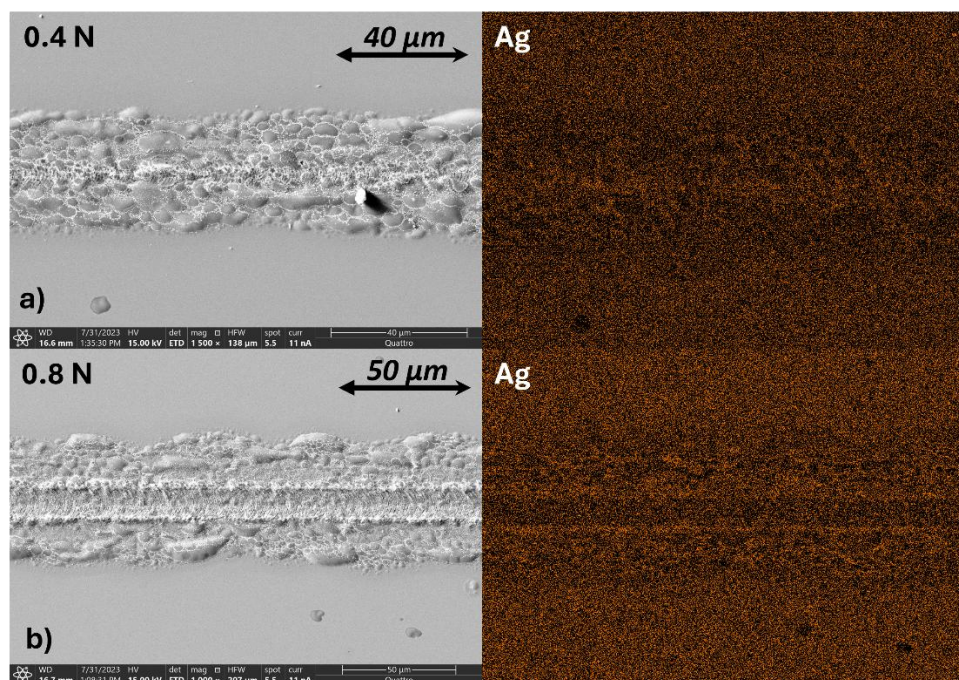


**Figure 4.8:** SEM and EDS mapping (Ag) image of a) low load (0.4 N) and b) high load (0.8 N) scratches following heat treatment.

Blistering features are seen to cover the scratch track, reminiscent of a localised delamination region in the coating; however, it is not clear with surface images at which specific depth of the coating the delamination occurs. Looking at the EDS mapping, the presence of Ag is observed, concentrated near the edge of the track (where partial delamination is observed on AC scratches as well) and surrounding the blister features. Given that the Ag signal is constant within the scratch track with surface SEM/EDS imagery in the AC state (not shown here, also at 0.8 N loading we are still within the  $Lc_2$  regime of failure), this observation reveals that the heat treatment has affected the Ag layer in such a way that it has found a way to diffuse towards the surface of the coating. The similar morphology of both HT scratches confirms that the mechanisms enabling the degradation of the coating (scratch intensification) are similar for both loading regimes, but it only manifests itself in a more significant manner for higher load scratches.

Finally, a cross section analysis was performed to analyse the heat-treated scratches from within, giving valuable information on the mechanisms enabling the coating degradation. Figure 4.9 shows the region that was selected for the cross-section analysis as well as SEM images of the cross-sections in question. A set of 0.4 N load scratches were performed on two separate samples. One



was used for the TEM characterization for the AC sample and the other was heat-treated as usual and used for the HT characterization. Figures 4.9a and 4.9b were taken after the milling of the first side of the sample to expose a cross-section that can then be analysed by SEM and to proceed with the preparation of the TEM lamellas. The images on the bottom are the SEM cross-sections taken before the lamella extraction. The scratch direction, scratch track and position of the low-e coatings are specified in the figures.

On the one hand, the damage observed on the as-coated sample is minimal as can be seen in the higher magnification SEM image from Figure 4.9a, where little to no significant deformation is observed near the center of the scratch track inside the cross-section. This observation is consistent with TEM imagery analysis as well. Figure 4.10 shows the full lamella prepared for high resolution imaging as well as multiple higher magnifications of regions of interest within the lamella. Two separate layers of C and one of W were deposited on the sample during the preparation of the

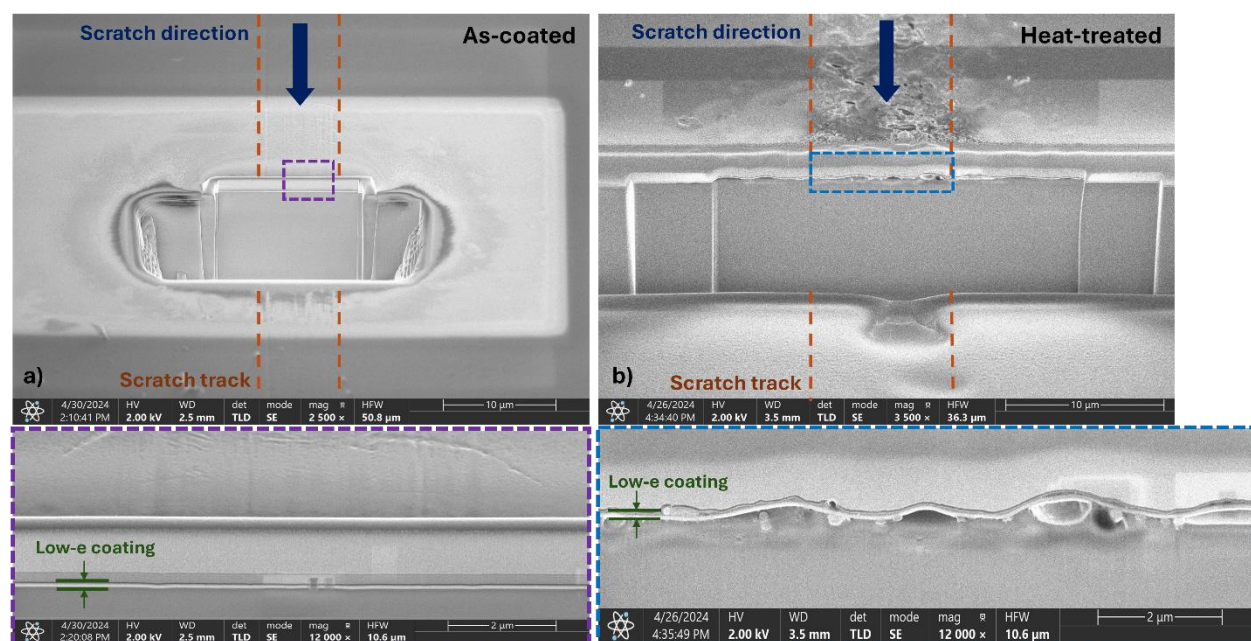


**Figure 4.9:** SEM images of the cross-section exposed for the TEM analysis as well as the corresponding higher magnification SEM images of the cross-section of a) an as-coated and b) heat-treated, 0.4 N scratch.

lamella to protect the coating from the ion beam milling to avoid surface damage and help prevent charging of the sample under the electron beam. The position of these materials as well as the upmost layer of the coating ( $\text{ZrO}_2$ ) and the Ag layer is presented directly on the figures. One can always refer to the full coating architecture presented in Figure 4.1 as a reference for the position of every layer in the stack.

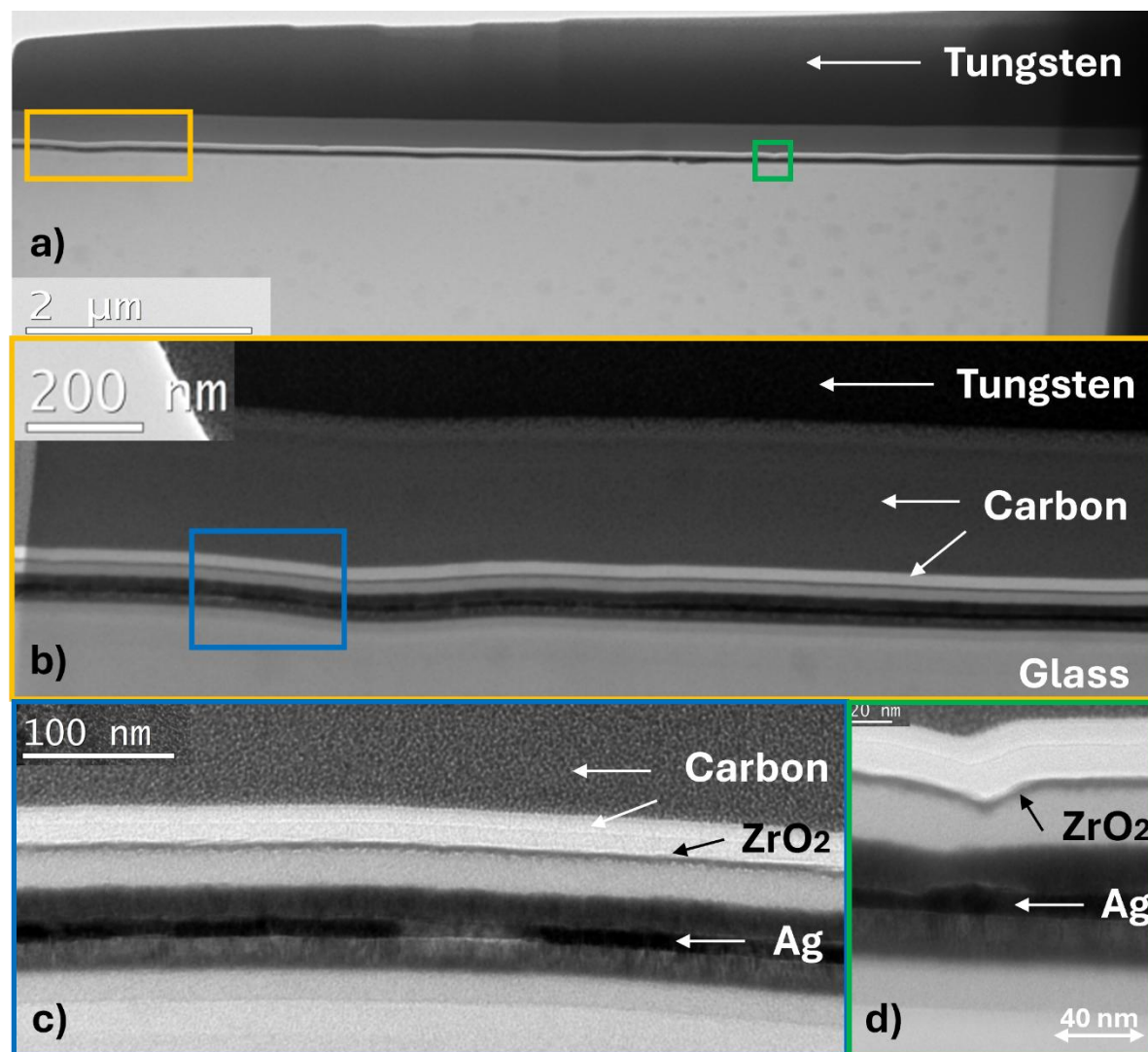


**Figure 4.10:** a) Full TEM images of a lamella taken from an as-coated scratched sample (0.4 N load) (see Figure 4.9a for SEM images). b), c) and d) correspond to higher magnification TEM images of regions of interest within the cross-section.

It is clear, here, that any type of failure on AC scratches is, in almost all cases, cohesive. The coating is not significantly disrupted and each layer above 5 nm can easily be identified in their order of appearance in the architecture. However, as seen in Figure 4.10c, an adhesive failure is observed between the Ag layer and its seed  $\text{ZnAlO}_x$ , where a slight separation of the layers is apparent (white area in the silver layer). In Figure 4.10d, an example of a more severe deformation of the layers is also observed. The three top layers of the coating are deformed inwards toward the inside of the coating, and it appears that this deformation causes an inverse effect on the Ag layer, where it is seen that the layer bulges outwards, toward the surface of the coating at the same location. On the sides of this bulge, the Ag layer appears pinched, and the effective thickness is slightly reduced. As mentioned previously, features such as the ones seen in Figure 4.10c and 4.10d can weaken the adhesion and create stress concentration near interfaces, facilitating delamination upon heating. As an example, the  $\text{SiN}_x$  layer located just below the top  $\text{ZrO}_2$  layer, is a material exhibiting high hardness and known to show lack of plastic deformation before failure. As no adhesive failure has been witnessed yet, stress is expected to accumulate near its interfaces. Nonetheless, as observed, the integrity of the Ag and its pinning  $\text{NiCrO}_x$  layer is kept mostly undisturbed. No TEM images were taken on higher load scratches in their AC state, however, the witnessed more intense plastic deformation is expected to increase the disruption on the layers of the coating (discussed in Chapter 5).

On the other hand, the damage and degradation seen after HT is clear and significant. Figure 4.11 shows TEM images similar to the one shown for the AC sample, where the first figure is a recombined panoramic image of the total lamella and where subsequent images are higher magnifications of regions of interest. Two main degradation features are observed here. Firstly, full delamination of the coating is present in various places throughout the lamella (observed at high magnification in Figure 4.11b, 4.11c and 4.11e. Identifying each layer of the coating confirms that the delamination occurs near the beginning of the first layers of the coating ( $\text{SiN}_x$ /Glass interface). Delamination of the coating creates large micro-scale voids and interstices between the coating and the glass substrate. Secondly, the Ag layer is now significantly disrupted and discontinuous throughout the analyzed lamella. Figures 4.11d and 4.11e show regions that appear completely depleted of Ag, and large dark nanoparticles are observed in various places within the coating, such as inside the voids created by the full delamination of the coating, below and above the depleted layer of Ag, and even in smaller quantities inside the glass substrate.

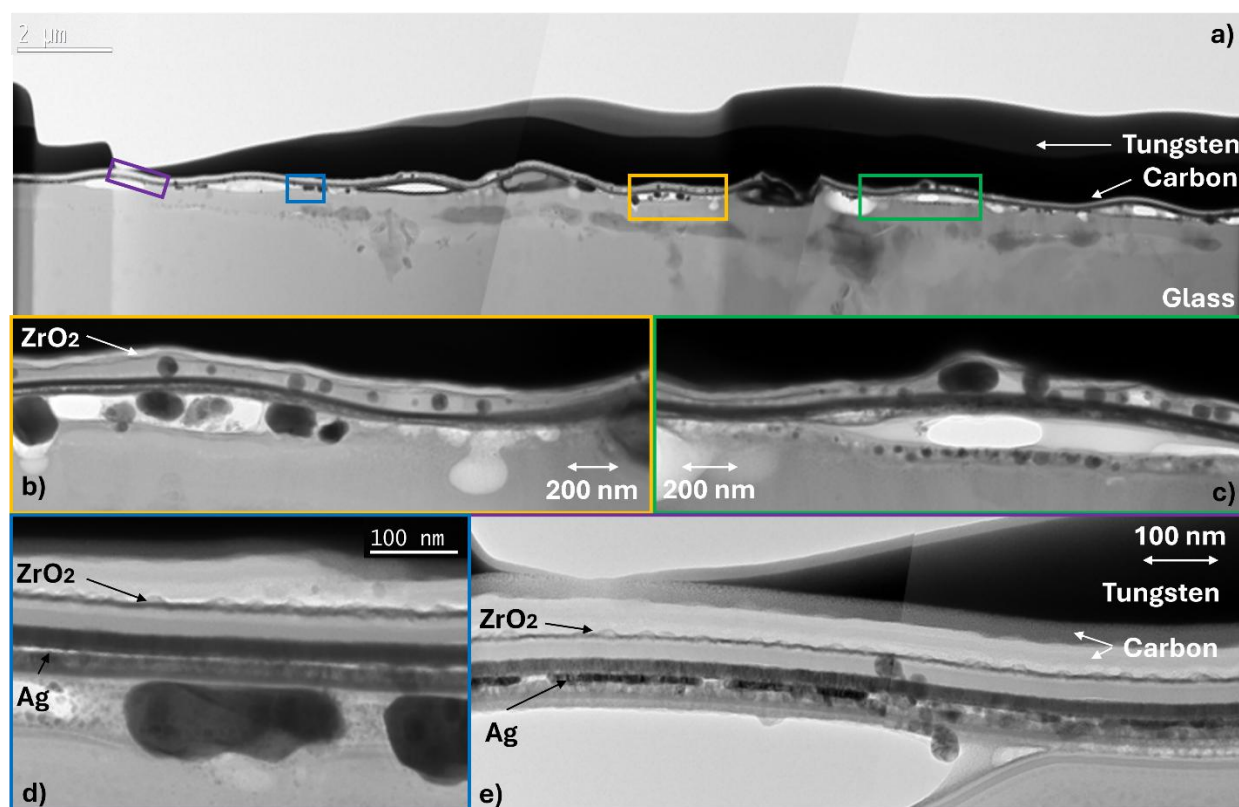


**Figure 4.11:** a) Full TEM images of a lamella taken from a heat-treated scratched sample (0.4 N load) (see Figure 4.9b for SEM images). b), c), d) and e) correspond to higher magnification TEM images of regions of interest within the cross-section.

Confirmation of both observed degradation features comes from EDS mapping of TEM images. Figure 4.12 shows two TEM images taken in dark-field (DF-TEM) mode with their respective EDS mappings of elements of interest. Whereas the previously presented TEM images were taken in the bright-field mode (BF), rendering heavier atoms darker in the resulting image due to the unscattered electron signal, the DF-TEM images using the scattered electrons and creating an inverse effect when heavier atoms (that scatter electrons more) appear brighter in the final image. In Figure 4.12a, the Ag EDS mapping clearly shows the presence of large Ag nanoparticles spread inside the delamination voids as well as in the top layers of the coating. Figure 4.12b shows the edge of a delamination void, and it is seen with the chemical mapping for N and Ti, namely materials present in the first ( $\text{SiN}_x$ ) and second ( $\text{TiO}_2$ ) layers of the stack, that the delamination seems to occur near the interface of both layers.



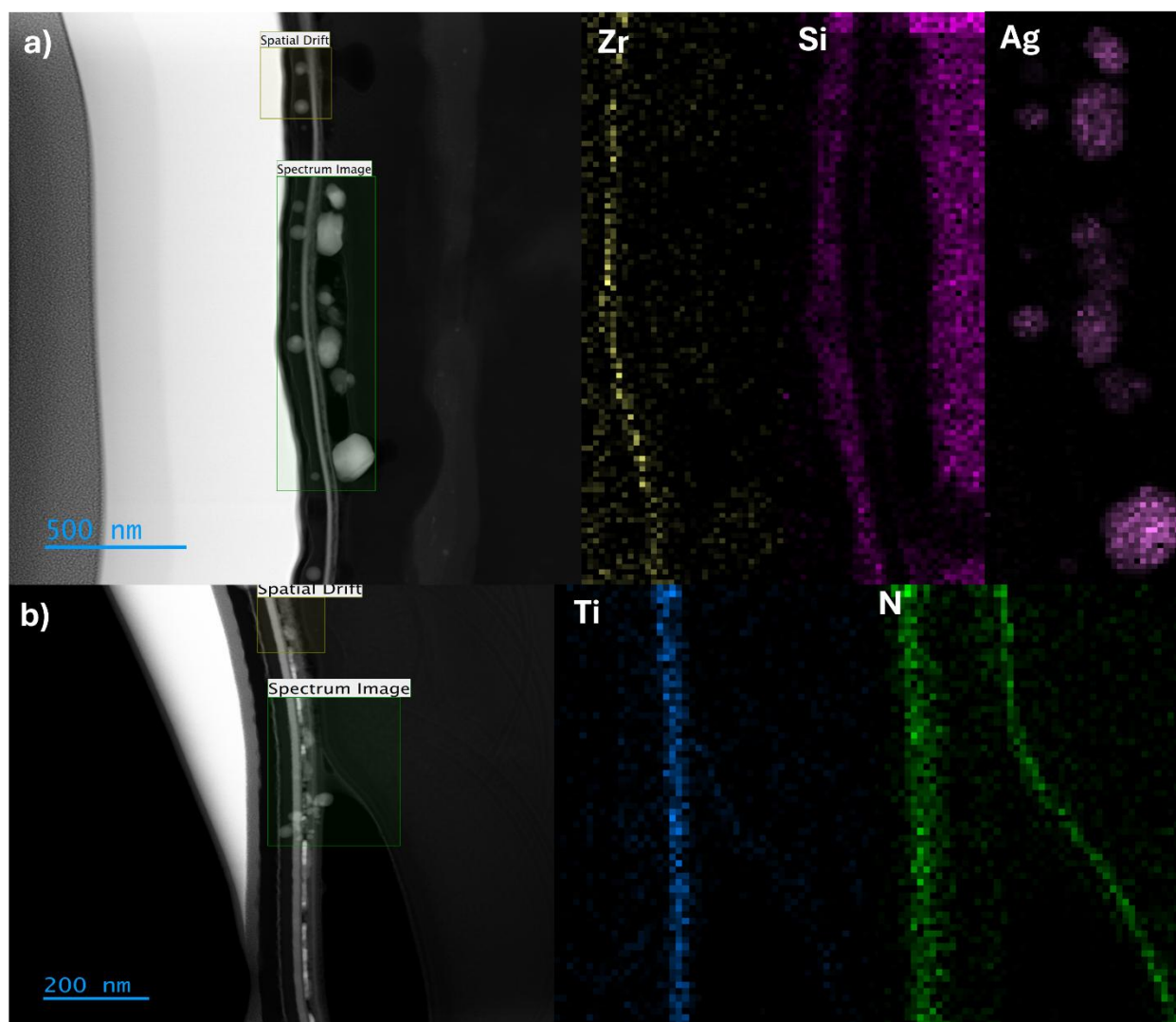


**Figure 4.12:** DF-TEM images taken from a heat-treated scratched sample (0.4 N load) paired with corresponding EDS mappings for chemical analysis highlighting a) Ag nanoparticle formation, and b) full delamination of the coating.

As a conclusion to this section, the morphology, visibility and intensification of scratches were introduced. It was shown that in their as-coated state after scratching, scratches present cohesive and adhesive failure modes (tensile cracking and delamination respectively), depending on the applied load. Paired with that, cohesive plastic deformation of the coating is witnessed at lower and higher magnitudes. Lower load scratches tend to be invisible in their AC state, whereas higher load scratches already appear visible. Following HT, scratches of both regimes intensify, and higher load scratches become highly visible. Blistering, degradation, delamination of the majority

of the coating and formation of large Ag nanoparticles are observed under a microscope, SEM, TEM and EDS imagery within the coating in the scratched region. At this point of the investigation, intensification and higher visibility following HT is most likely caused by two mechanisms. Firstly, the large micro-scale voids created from the delamination creates physical space between the coating and the substrate enabling light to travel multiple different paths and increasing reflection at specific wavelengths in the visible region, in contrast, to its antireflective nature in the pristine state of the coating. Secondly, degradation of the coating represented by the depletion, diffusion and agglomeration of Ag creates large Ag clusters (up to 150 nm in diameter) that also act as scattering centers for incoming light, again, increasing scratch visibility.

### **4.3 Influences on defect visibility**

Until now, the degradation and scratch intensification observed on low-e coatings were only analysed as a function of scratch load, where it was seen that low and high loading conditions resulted in different levels of visibility of the HT scratches, but were related to similar mechanisms, such as degradation of the coating through full coating delamination and Ag nanoparticle formation. This section aims to further study the intensification by varying additional key parameters, namely, altering the duration of the heat treatments of the sample, storing the sample, after scratching, in a high humidity environment, and finally, altering the architecture of the coating itself. This section summarises the main findings of these experiments.

#### **4.3.1 Heat treatment**

The conducted experiment consisted in evaluating the impact of the HT duration on the scratch visibility. Two sets of four scratches were performed on four REF samples. In the first set, the four scratches were performed using constant loading with a load of 0.4 N and a load on 0.6 N was used on the second set of scratches. Each sample was heat-treated for a different amount of time (6, 9, 12 and 15 minutes) at 650 °C. The HT images of the samples were taken with lighting configuration A. Figures 4.13 and 4.14 show the HT scratches for the four treated 0.4 N and 0.6 N scratches, respectively.

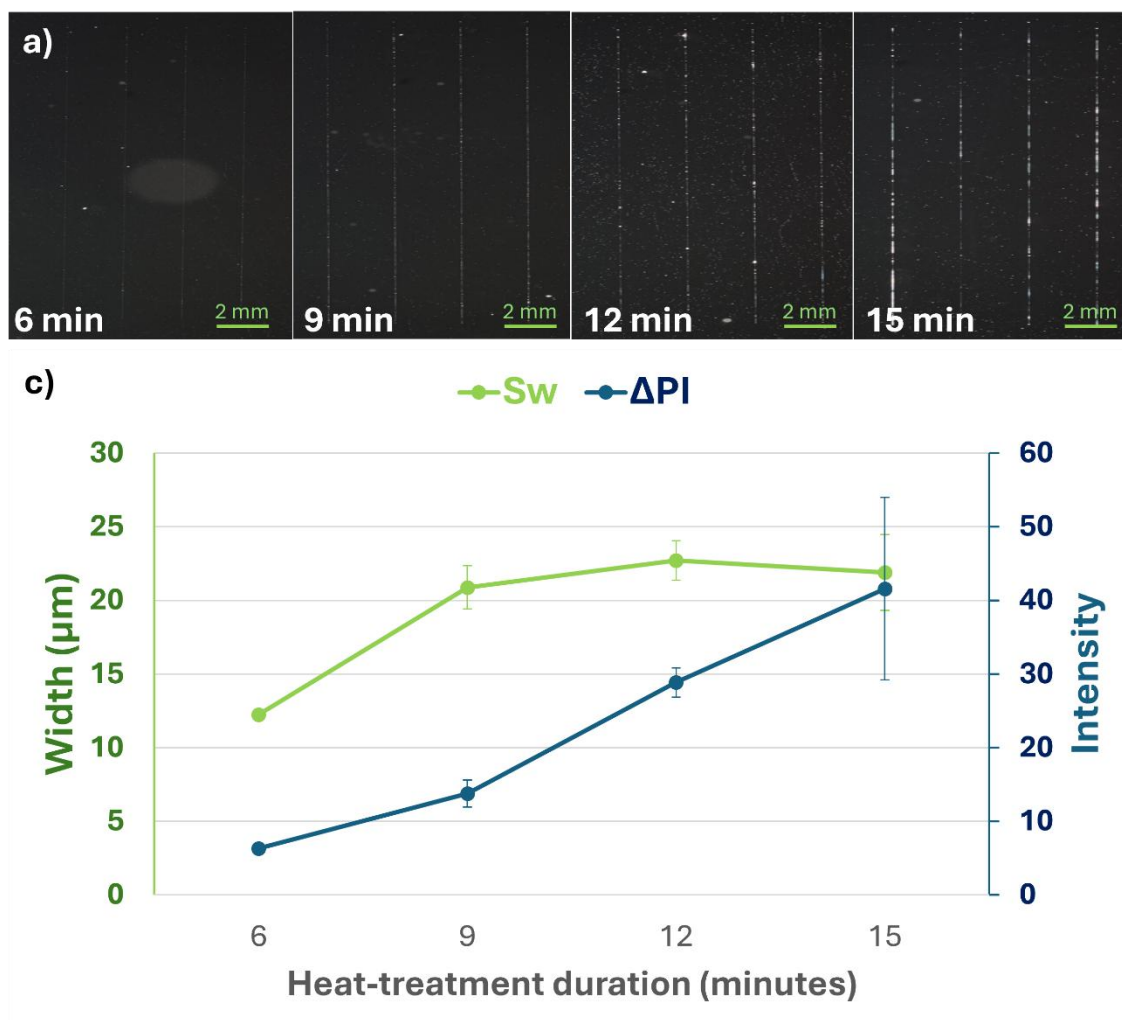


**Figure 4.13:** a) Images of the four REF samples, each scratched at four constant loads of 0.4 N and heat-treated with increasing durations at 650 °C (6, 9, 12 and 15 minutes). Images taken with f/16 for the aperture, 100 ISO and 2 s of exposure. b) Corresponding average scratch width ( $\bar{S}_w$ ) and variation of peak intensity ( $\Delta PI = HT PI - AC PI$ ) values extracted from the images.

Beginning with the lower load experiment, the visibility of the scratches appears to increase linearly with time. As the scratches are invisible pre-HT, no data can be recorded on the scratch width ( $S_w$ ) and the as-coated peak intensity (AC PI). As mentioned in Section 2.2.3, typical degradation in Ag-based low-e coatings during the heat treatment involves the diffusion and agglomeration of Ag within the coating as the diffusion power of Ag is greatly increased at annealing temperatures compared to room temperatures. Performing longer heat treatments thus increases the time for which the Ag layer can degrade and agglomerate within the scratch,

therefore, inevitably increasing scratch visibility.  $S_w$  tells a slightly different story however, where it nearly reaches its maximum value only after the first few minutes of the treatment (at 9 minutes of HT). This indicates that the increase in visibility that is witnessed between 9 and 12 minutes and again between 12 and 15 minutes of HT truly is a result of the degradation located inside the scratch track and not the result of lateral intensification (i.e. widening of the scratch). This first set of samples hints at the dynamics of the intensification during the HT for lower load scratches: scratches that are invisible AC will quickly increase in width and gradually increase in intensity over time.

Secondly, the effect for a higher loading is quite different, as seen in Figure 4.14. This time, as expected, the AC scratches were already visible, and the data showed an  $\overline{S_w}$  of  $36.28 \mu\text{m} \pm 11.27 \mu\text{m}$  and an  $\overline{\text{AC PI}}$  of  $28.00 \pm 6.42$ . Here, the data regarding the average intensity of the heat-treated background (HT Bkg) is added and is also identical to the one recorded for the low load scratches as all the sets of scratches, regardless of load, were performed on the same four samples. This metric is added to highlight an effect that arises when using the variation of peak intensity ( $\Delta\text{PI}$ ) values. As explained in Section 3.4.2, when performing the image processing analysis, the data is corrected for the background and the  $\Delta\text{PI}$  values are then calculated. This entails that, if significant changes are observed in the background of the sample following the HT, the correction on the data will affect the values of the HT PI as well, lowering the resulting  $\Delta\text{PI}$  value. This is what we observe here, where the variation of intensity for higher loading seems to decrease for increasing HT duration.

In reality, we see an increase in the haze of the sample, increasing the background intensity. By correcting for the presence of a more intense background, one can be convinced that the variation of the intensity on these higher load scratches are quite constant throughout the tested HT durations. This indicates that the majority of the degradation, on these AC visible scratches, is created in the few first minutes of the heat treatment (before 6 minutes). Moreover, on these same scratches, the  $S_w$  is mostly unchanged in the first minutes of the HT, with a  $\Delta S_w$  of  $2 \mu\text{m}$  to  $8 \mu\text{m}$  between 6 and 12 minutes, increasing to over  $50 \mu\text{m}$  at 15 minutes. Contrary to scratches that are invisible pre-HT, that gradually intensify over the tested durations, here with already visible AC scratches, we observe that they quickly become highly visible during HT and increase significantly in width following longer durations of HT.



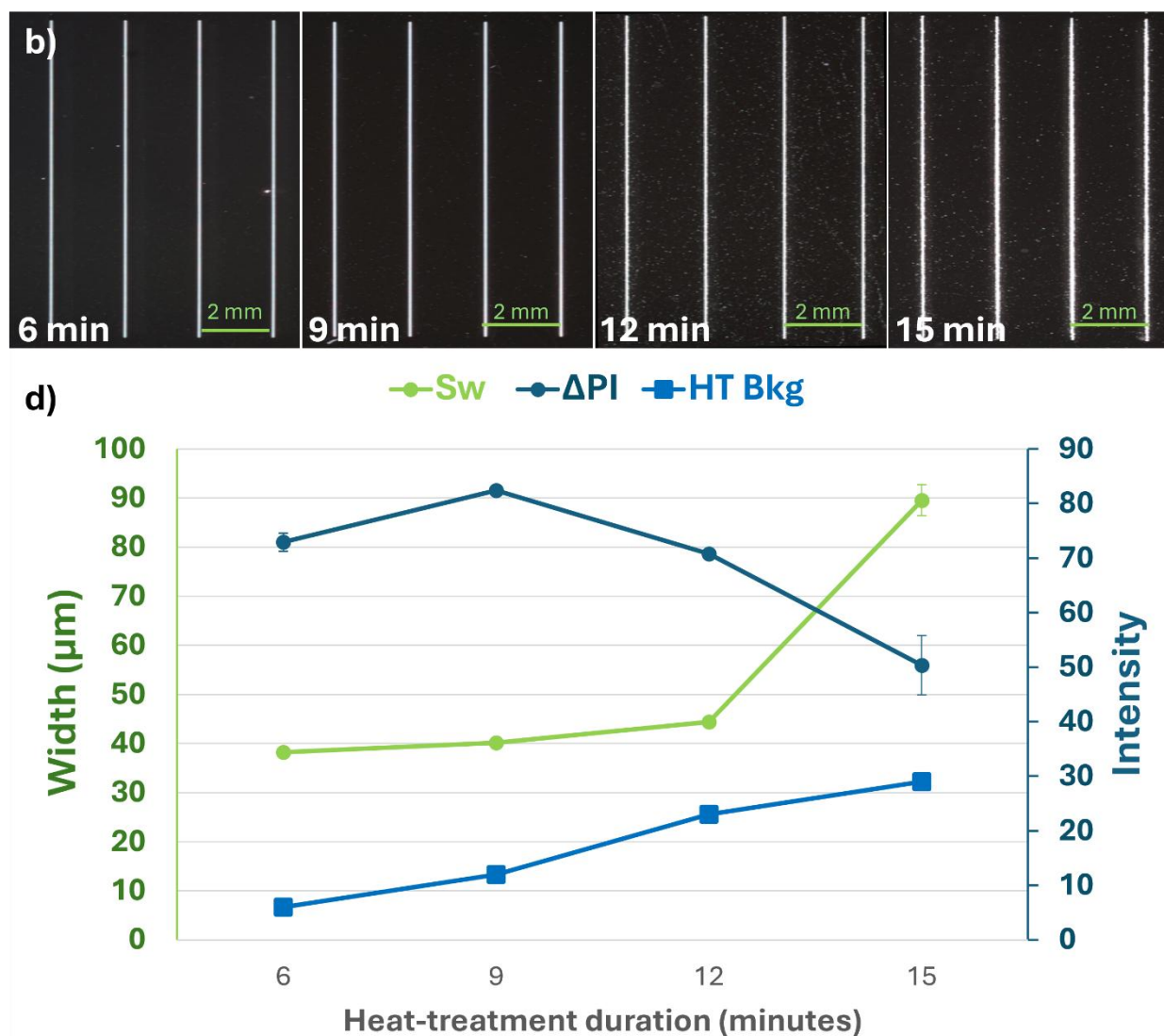


**Figure 4.14:** a) Images of the four REF samples, each scratched at four constant load of 0.6 N and heat-treated with increasing durations at 650 °C (6, 9, 12 and 15 minutes). Images taken with f/16 for the aperture, 100 ISO and 2 s of exposure. b) Corresponding average scratch width ( $\overline{S_w}$ ) and variation of peak intensity ( $\Delta PI = HT PI - AC PI$ ) values extracted from the images.

Linking these observations to the degradation mechanisms introduced in the previous section helps in detailing the mechanistic behavior of the degradation for different load regimes. At lower loading, scratches are invisible, present tensile cracking and slight plastic deformation, the degradation of the coating starts locally and develops radially within the scratch track while further

degradation, increasing with the duration of the HT, consequently, increases the overall visibility of the scratches.

The constant  $S_w$  seems to indicate that the lateral intensification of degraded regions is limited, while the increase in  $\Delta PI$  seems to indicate the generation of more of these regions in various locations within the scratch track. This  $S_w$  behavior for lower loading presumes that, during the HT, regions in the scratch track that are not yet degraded will be favored for degradation over lateral intensification of already degraded regions.

At higher loading, scratches are already visible and wide pre-HT (already wider than lower load HT scratches) and present a high density of tensile cracking, partial delamination, and significant plastic deformation. Because of this higher disruption in the film, degradation is speculated to quickly occur along the whole scratch (high  $\Delta PI$  observed in the lowest HT durations). Again, degradation in the track is believed to be favored over lateral intensification, explaining the near constant  $S_w$  at 6, 9 and 12 minutes. Eventually, the sudden increase in  $S_w$  for the 15 minutes HT experiment suggests that once the scratch track is fully degraded, longer heat exposure times will begin to widen the scratch further, creating an even more noticeable defect for an external observer.

#### 4.3.2 Effect of humidity

Based on the degradation mechanisms in Ag-based low-e coatings presented in Chapter 2, where it was found that contact or exposure to moisture resulted in significant degradation of the coating (even without performing heat treatments on the sample), experiments were carried out to investigate the effect of exposure to humidity on scratch intensification. The experiment consisted in scratching two REF samples and storing one of them for 20 h in a high humidity (> 85% RH) environment and the other in a desiccator connected to the low vacuum of the laboratory ( $\approx 90$  Torr) for the same amount of time to act as a buffer sample for accurate comparison.

Figure 4.15 shows the four analysed images taken with the visibility setup of both samples in their AC and HT state as well as the variation of peak intensity ( $\Delta PI$ ) and variation of width of the scratches ( $\Delta S_w$ ). Again, the constant scratches were performed from 0.2 N to 0.8 N and the images were taken using lighting configuration A.

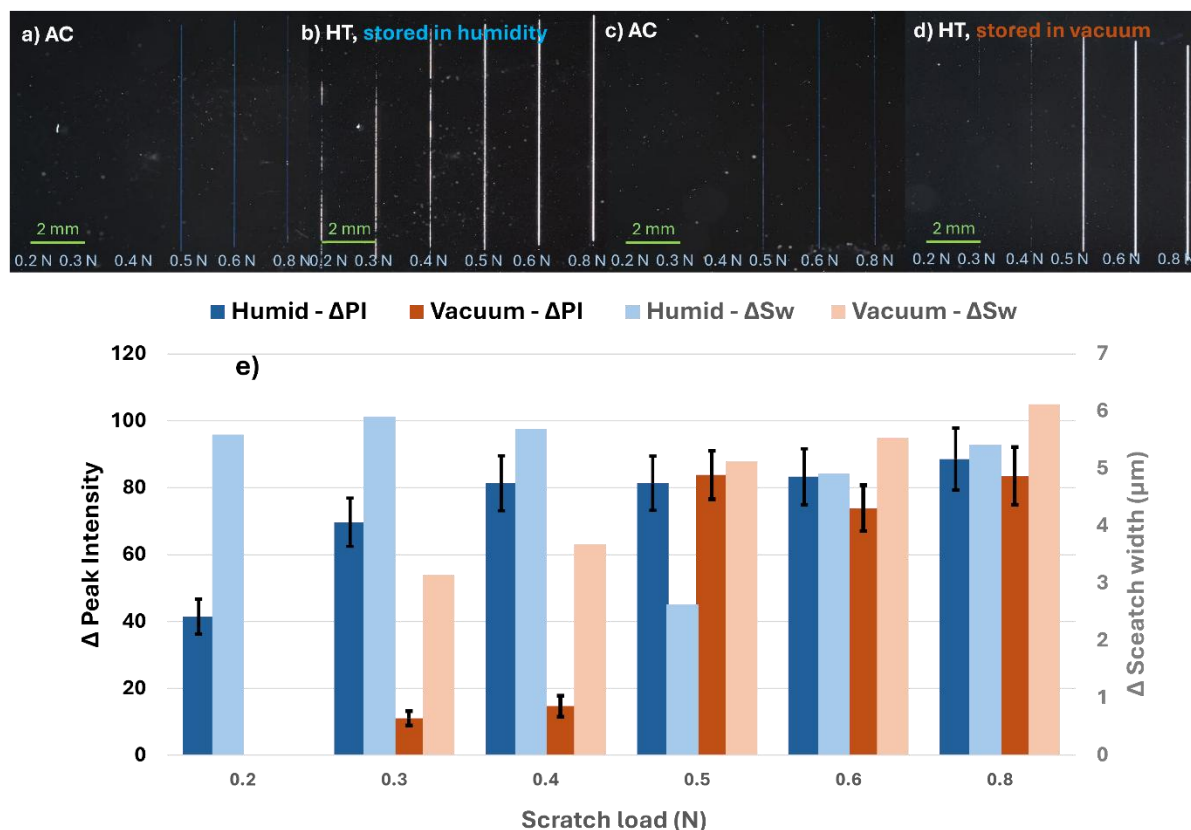


**Figure 4.15:** Visibility setup images of scratched coatings: a) as-coated, to be stored in a high humidity environment for 20 h; b) after storage and heat treatment; c) as-coated, to be stored in a low vacuum environment for 20 h; d) after storage and heat treatment. Images were taken with f/16 for the aperture, 100 for the ISO and exposed for 0.5 s. e) Corresponding  $\Delta PI$  (bold colors, left axis) and  $\Delta S_w$  (light colors, right axis) metrics obtained via the image processing code.

Firstly, from the setup images, one can witness the significant contrast in visibility occurring for lower load scratches stored in humidity compared to the buffer sample. Low loading on both samples is undetected in AC, but scratches that were exposed to moisture intensify greatly. The  $\Delta PI$  data in the graph (dark blue and orange data sets) for lower loads shows that the intensification for humid storage strengthens with the load and is multiple times larger than the intensification observed for the buffer samples. On this buffer sample, the intensification appears somewhat proportional to the load, where no intensification is observed for 0.2 N and a slight increase in intensification is observed between 0.3 N and 0.4 N. Higher loading presents a different behavior, where scratching with a 0.5 N load and above presents comparable intensification for both storage

conditions. It is important to note here, that similar images of the scratches were taken right after the storage in their respective conditions, but no noticeable differences were observed compared to the sample before storage. As such, they are not shown here and can be assumed to be identical to AC images. This behavior indicates that the storage in humidity and the exposure of the damaged coating to moisture enables degradation (significantly on lower load scratches), only upon heating and not in a discernable manner after the storage.

Chapter 2 presented instances where degradation was observed on both encapsulated and nonencapsulated Ag-based low-e coatings even without performing any type of heat treatments [48], [51], [53]. However, the degradation observed was often the result of multiple days of storage in very high humidity (and sometimes corrosive) environments and has been found to be mostly initiating near defects in the coatings, such as cracks or edges of the sample as also seen in samples presented here, where the degradation is apparent solely in the scratch track. The higher intensification observed for lower loading indicates that moisture and corrosive mechanisms affect lower load scratches more, as higher load scratches appear to behave similarly regardless of storage conditions.

Comparing  $\Delta PI$  and  $\Delta S_w$  for vacuum storage (dark and light orange datasets) indicates that both are highly correlated as both variations increase with respect to the other. Again, a higher variation is observed for lower loads and when stored in humidity. Contrary to the gradual increase of the  $\Delta PI$ ,  $\Delta S_w$  is high and constant, for lower loads, in humid storage conditions, and lower for higher loads. This could also be observed in the previous HT duration experiment where for a 12 minutes HT, the  $\Delta S_w$  found for the 0.4 N scratch (25.73  $\mu m$ ) was higher than the one found for the 0.6 N scratch (8.15  $\mu m$ ). This is most likely due to the fact that, as lower load scratches are invisible AC, the width transition is much more apparent when they become visible after HT, compared to higher load scratches that are already visible pre-HT. Consequently, the effect is mitigated for lower load scratches stored in vacuum, as they intensify to a lesser degree after HT.

In order to investigate the degradation following lower load scratches in more detail, SEM and EDS analyses were performed on the presented samples. Figures 4.16 and 4.17 both present SEM images of lower load scratches for samples stored in both storage conditions. Figure 4.17 adds EDS mapping images for Ag for the presented SEM images. The effect is clear when analyzing the images taken on the buffer sample. In Figures 4.16b and 4.17b, the observed degradation is very

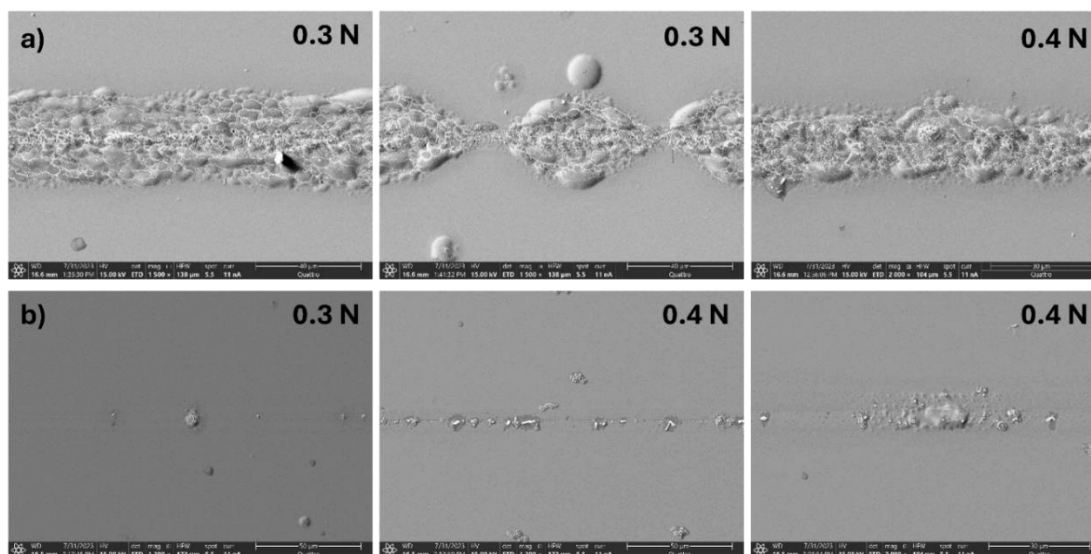


**Figure 4.16:** SEM images presenting the observed degradation features on a) a heat-treated sample stored in a high humidity for 0.3 N and 0.4 N load scratches, and b) a heat-treated sample stored in a low vacuum environment for 0.3 N and 0.4 N load scratches as well.

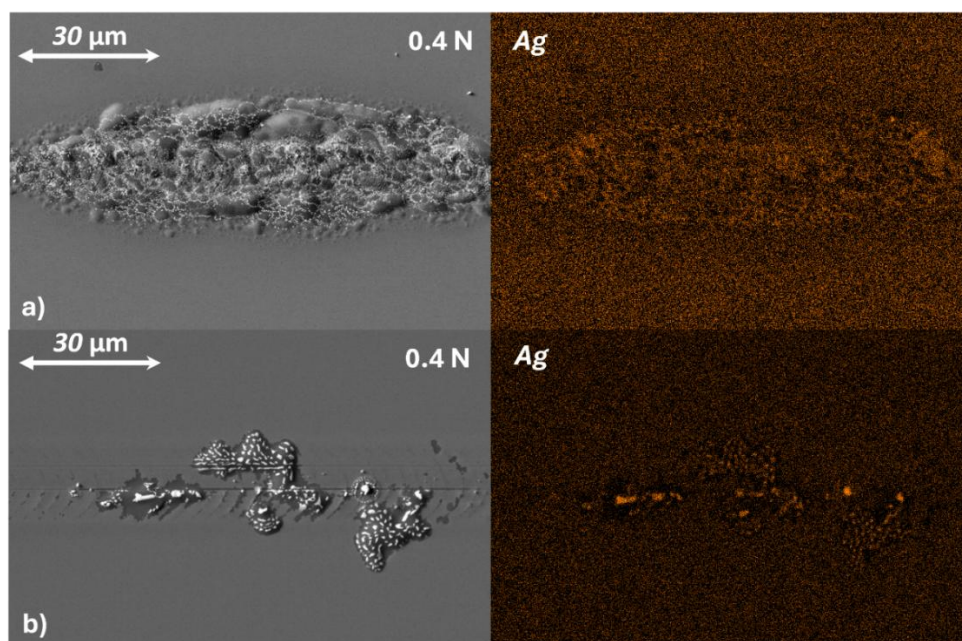


**Figure 4.17:** SEM images presenting an observed degradation feature of interest on a) a heat-treated sample stored in a high humidity for 0.4 N load scratches, and b) heat-treated sample stored in a low vacuum environment for 0.4 N load scratches as well as the respective EDS mapping for Ag elemental chemical composition analysis.

limited, and regions of Ag depletion are detected (dark grey zones) surrounding rich regions (white dots) indicating the diffusion of Ag from its uniform layer to clusters, but no severe delamination of the coating and important blistering such as can be seen in Figure 4.16a. No additional degradation features from the ones presented in Section 4.2.2 are observed on the humidity-stored sample for lower loading. This indicates that the effect of the exposure to humidity does not fundamentally change the degradation mechanisms present on these HT scratches, rather it enables them to occur on the lower load scratches, whereas a storage in an unreactive environment, similar to the one used for the buffer sample, largely mitigates the degradation.

Until now, the degradation was linked purely to disruptive changes in the films, that are present in a more significant manner following higher loading. This experiment revealed that exposure to humidity, for higher loading, didn't result in a more notable visibility of the scratches, contrary to lower loading. Therefore, degradation of the coating, enabling more visible scratches, must stem from the contribution of both factors, on one hand, the disrupted nature of the coating following scratching, and on the other, the exposure of this damaged coating to humidity. Lower load scratches stored in vacuum stay mostly invisible after HT, while higher load scratches stored in a humid environment present the highest visibility altogether.

### 4.3.3 Effect of the stack architecture

The final conducted experiment aimed to characterise the visibility and intensification of scratches made on variant architectures of the reference sample presented in Section 4.1.1 used during the project. The goal was to investigate which layers in the complex coating contributed the most to the observed increase in the visibility of the stack and which layers contributed to it less, in order to consider alterations that could be made on future architectures that would mitigate scratch intensification.

Figure 4.18 shows seven of the variant architectures that have been obtained from our industrial collaborator, detailing the order of the layers of the coatings alongside the used REF sample. Two variant stacks were tested to investigate changes in the topcoat of the coating: T-1 removing the top  $\text{ZrO}_2$  layer and T-2 removing both the top  $\text{ZrO}_2$  and  $\text{SiN}_x$  layer. Two stacks were tested in order to investigate the removal of the  $\text{NiCrO}_x$  pinning layer: T-5, as a new reference with only a  $\text{SiN}_x$  and a  $\text{NiCrO}_x$  layer on top of the Ag and T-6, without the  $\text{NiCrO}_x$ . Finally, two stacks were tested

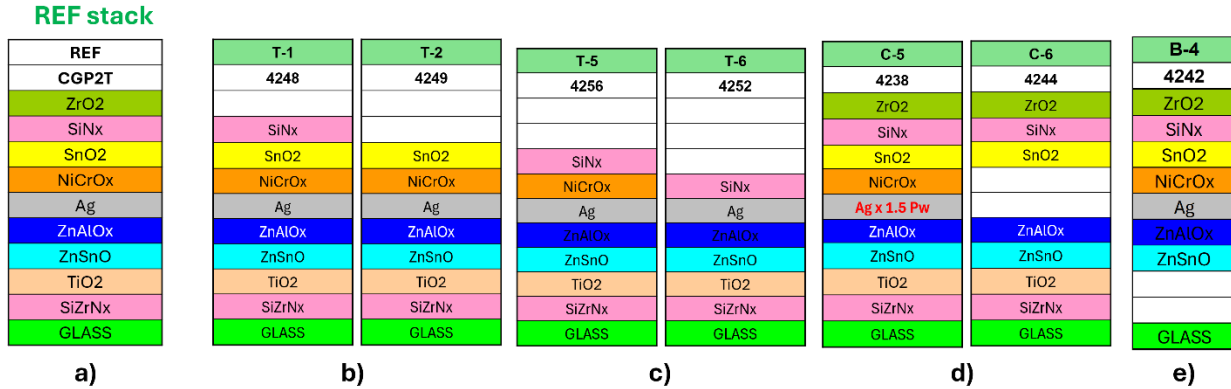


Figure 4.18: Architectures of a) the REF sample, b) coatings with changes in the topcoat: T-1 (no ZrO<sub>2</sub>) and T-2 (no SiN<sub>x</sub>), c) coatings with changes near the Ag layer: T-5 (NiCrO<sub>x</sub>) and T-6 (no NiCrO<sub>x</sub>), d) coatings with changes in the Ag layer: C-5 (thicker Ag) and C-6 (no Ag), and e) coatings with changes in the bottom layers: B-4 (no SiZrN<sub>x</sub>).

to examine the effect of the Ag layer: C-5 with a thicker Ag layer and C-6, without Ag, as well as a final stack for the examination of the bottom layers of the coating, with B-4, removing both TiO<sub>2</sub> and SiZrN<sub>x</sub> bottom layers.

Six scratches were performed on each variant sample (with constant loading of 0.2, 0.3, 0.4, 0.5, 0.6 and 0.8 N), as well as on a REF sample and all were heat-treated as usual for 12 minutes at 650 °C. Figure 4.19 shows the images taken on the AC and HT samples for the variant stacks that showed the most changes following HT (f/16 for the aperture, 100 for the ISO and exposed for 2 s) and Figure 4.20 shows the corresponding histograms, where the  $\Delta$ PI data is shown for all variant stacks tested for high and low loading.

It is important to note that contrary to previous experiments which were carried out all on a REF sample, for variant architectures different scratch resistance behaviors are expected on the various stacks. This means that where we could simply compare 0.4 N load scratches on multiple REF samples, now, a 0.4 N scratch on two variant architectures might present different visibility values for AC. This can become a problem when evaluating the resulting  $\Delta$ PI values. As such, based on the recorded data of the AC visibility of the 0.4 N and 0.8 N load scratches on the REF stack, an “equivalent load” was found for higher and lower loading on the variant stacks that presented similar AC visibility.



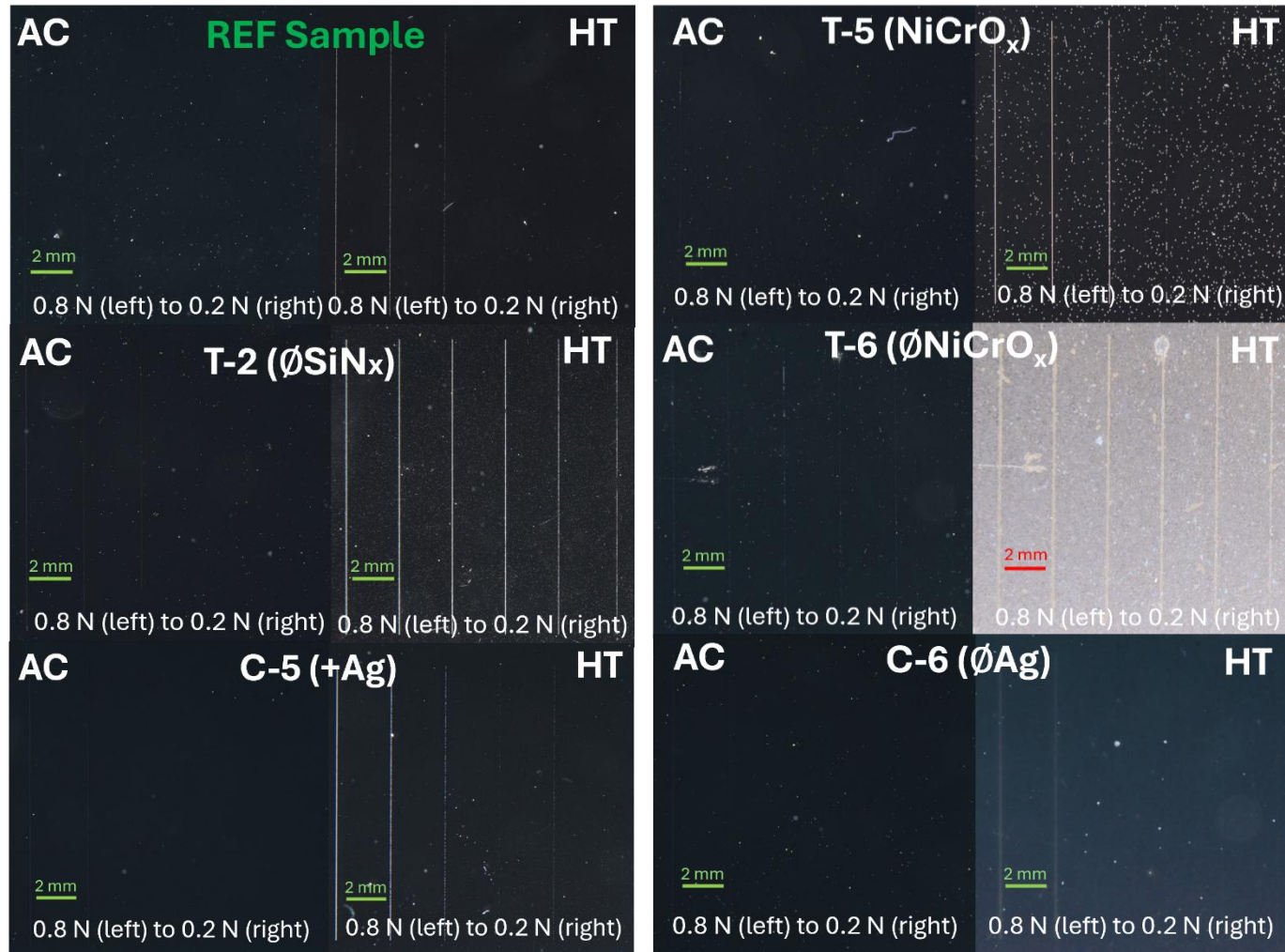


**Figure 4.19:** Visibility setup images of AC and HT scratches (constant load from 0.8 N to 0.2 N, left to right) on the REF sample as well as five variant stacks of interest: T-2 (no SiN<sub>x</sub>), T-5 (NiCrO<sub>x</sub>), T-6 (no NiCrO<sub>x</sub>), C-5 (thicker Ag) and C-6 (no Ag).



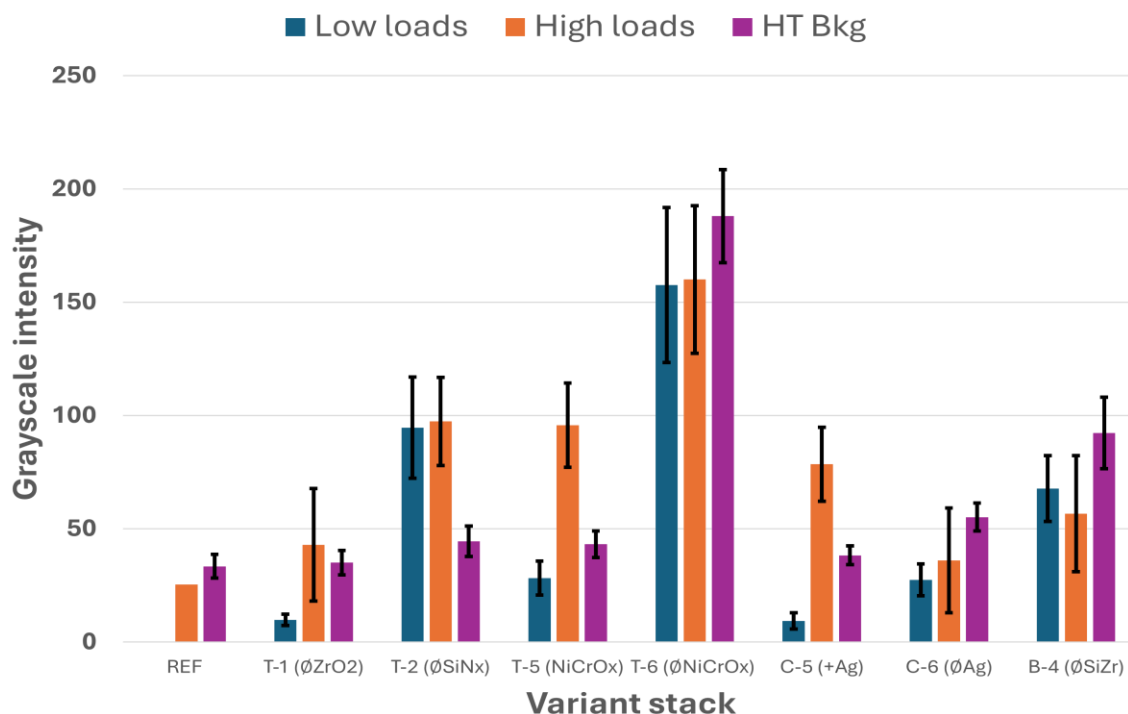


**Figure 4.20:** Histogram presenting the variation of peak intensity ( $\Delta PI$ ) for the different tested variant stacks for lower and higher equivalent loading as well as the heat-treated background intensity values (HT Bkg).

Figure 4.20 presents the visibility following low and high loading. In the same figure, multiple behaviors are observed. First, it is seen that, without great surprise, that the REF intensification is the lowest one recorded. The most notable changes occur on the T-2, T-6 and C-6 stacks. On T-2, all scratches become visible after HT, regardless of the load. In fact, removing both top layers in this variant stack corresponds in lowering the overall thickness of the coating by over 25%, creating a much thinner coating. The thickness difference of the T-2 stack compared to the REF stack is also the highest one for all the variant stacks tested. This entails that scratches that are performed at the same load on the REF sample, are expected to disrupt the coating, and the Ag layer in a more significant manner since the SiN<sub>x</sub> layer is no longer there to absorb some of the damage before reaching the Ag layer. As a result, the coating is more disrupted, and a higher intensification is expected, as seen typically in higher load scratches vs. lower load ones on the REF samples.

The T-6 variant presents a notably higher haze and higher visibility of lower loads compared to the reference stack, T-5. As presented in section 2.1.2, NiCr films are known to increase the adhesion and thermal stability in Ag-based low-e films. They reduce interdiffusion of Ag and other metallic materials present in the layers that can occur during HTs as well as protect the Ag layer from oxidation during the deposition process acting as a blocking layer [25]. Moreover, Ni is known to diffuse into the Ag, limited to the surface of the layer. This helps in limiting the surface Ag atoms ability to diffuse and forces Ag atoms from the bulk of the layer to diffuse, rather than the ones near the interfaces, inhibiting interface degradation [26]. Removing this NiCr layer, as seen with the T-6 variant, thus renders the coating more prone to Ag diffusion and corrosion during the HT. Consequently, the T-6 variant is expected to present more Ag nanoparticles and result in more overall degradation. As seen in the HT T-6 image from Figure 4.19, this degradation is seen within the scratches but is also observed even in non-scratched regions of the sample. This degradation is maximized when there is disruption in the coating, resulting in the highest intensity variation recorded for the tested variant stacks. In other words, even by correcting for the noisy background intensity of the images, the intensity within the scratches is still very high.

Furthermore, intensification behaviors for the stacks C-5 and C-6 agree with the mentioned degradation mechanisms. On stack C-5, the Ag thickness is higher by increasing the power during deposition (to 1.5×). Following the assumption that the increase in visibility is in part caused by the degradation of the Ag layer (with diffusion in the coating and agglomeration), more Ag would mean more instances of diffusion and perhaps larger Ag nanoparticles, increasing the visibility. This is what we observe on the HT images of the C-5 variant in Figure 4.19, where, compared to the REF sample, scratches are more visible. Similarly, on the histogram, one can witness that the intensification is higher, again, in a more noticeable way for higher loading, as seen on the REF sample. Although it presents higher variations of intensity, it is seen that a thicker Ag layer does not notably change the haze behavior, where the background of the sample remains similar to the REF sample as well as the intensification for lower loading, where multiple lower load scratches remain invisible following the HT.

In the same manner, removing the Ag layer altogether would be expected to considerably mitigate the intensification, as no Ag atoms are present for the degradation. Here, with the C-6 variant,

intensification is observed only on the high loading, indicating that high disruption of the coating with no presence of Ag can lead to more visible scratches following HT. However, the appearance of the visible scratches differs greatly from the ones seen in the REF samples and other variant stacks with the presence of an Ag layer: the scratches appear blurred in comparison to the usually observed sharp and high contrast scratches. This suggests that the morphology of the scratches is not similar to what was observed in Section 4.3.1 and that other mechanisms related to the dielectric layers in the coatings impact the visibility of the scratches as well. In the same fashion, haze formation is observed on C-6 and confirms that the degradation occurring in the coating is not solely reliant on Ag. In fact, the presence of a ductile metal such as Ag could help with the relaxation and stress changes noticed in the dielectric layers during the HT.

Finally, T-1 reacts similarly to the REF sample in terms of intensification. Removing the topmost layer, which is only a few nanometers thick, is expected to increase the COF between the coating and the tip when scratching, reducing the scratch resistance of the coating. With lower scratch resistance, higher disruption of the coating is expected at the same loads and thus, as seen in the HT images for the REF and the T-1 samples in Figure 4.19, a higher visibility is obtained. Finally, the B-4 stack exhibits important haze that can be linked to degradation occurring from the Na diffusion coming from the substrate. As presented in Section 2.1.2,  $\text{SiN}_x$  layers are often time used for their protective nature against Na diffusion, thus removing the layer is expected to increase its diffusion from the substrate inside the coating.

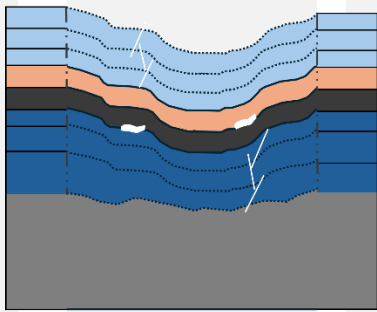
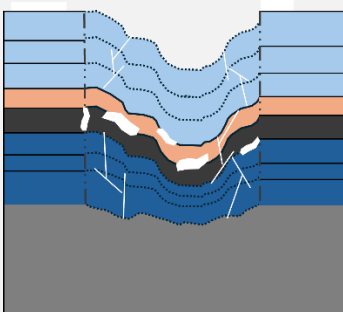
## CHAPTER 5      GENERAL DISCUSSION

This chapter aims to summarize the findings of the experiments and link them to the degradation model proposed for Ag-based low-e coatings undergoing heat treatment. A review of the different types of scratches performed, paired with the observed as-coated features for each, will be presented and the key mechanisms leading to degradation will be detailed.

Two main morphologies of scratches were studied in this project: the so-called lower load and the higher load scratches, categorized based on the different behaviors of their AC visibility. Scratch testing and structural analysis of both scratch regimes revealed that, apart from the AC visibility, they also presented different behaviors in other coating-related alterations, namely, the coatings and substrate plastic deformation, the crack formation as well as the expected Ag and NiCrO<sub>x</sub> layers' disruption. Table 5.2 summarizes these changes for both regimes and it shows a schematic representation of the expected morphology of the cross-section of a scratched coating, highlighting the crack formation and disruption observed and expected in the scratches. As mentioned previously, little attention was paid to scratches that would already appear highly visible in their AC state. In fact, as seen in Figure 4.3 from Section 4.2.1, performing scratch tests with loads above 0.8 N would possibly give rise to the  $Lc_3$  failure mode, the full delamination of the coating. As the  $Lc_3$  failure mode does not occur at the exact same load for each single scratch test, it is possible to observe it sooner, within the higher, or even the lower loading regime. This effect can also be seen in Section 4.1.1, from Table 5.1, where higher standard deviations were found for the  $Lc_3$ , compared to the  $Lc_1$  and  $Lc_2$ , indicating that the reproducibility of  $Lc_3$ , can vary much more than the other failure modes. As such, less focus was put on these delaminated scratches, compared to the higher and lower loading scratches that were confirmed to have kept most of their adhesive integrity in their as-coated state.

It is important to note here, that while the minimal disruption of the Ag and NiCrO<sub>x</sub> layer was directly observed in AC scratches at lower loads (see Figure 4.10), the disruption behavior at higher load was not directly observed. The additional TEM experiment which was performed seems to indicate the integrity of the stack following high load scratching. This experiment was performed on a high load 0.8 N scratch that was “heat-treated” under SEM. In fact, in an attempt to observe the surface degradation of the coating *in-situ* when heating, a custom heating stage was used inside

**Table 5.1:** Qualifiable observed changes in the coating's integrity for the two different load regimes of scratching.

CHANGES IN THE STACK	LOW LOADING	HIGH LOADING
<b>Coating and substrate plastic deformation</b>	Low, under 10 nm of total deformation depth	High, over 100 nm of total deformation depth
<b>Crack formation</b>	Observed from the surface, with lower density	Observed from the surface, with higher density
<b>Ag and NiCrO<sub>x</sub> disruption</b>	Minimal	Expected to be considerable
<b>AC visibility</b>	Modest visibility with the setup and practically invisible to the naked eye	Easily visible with the setup and variable to the naked eye
<b>Expected schematized cross-section morphology</b>	<div style="display: flex; justify-content: space-around; align-items: flex-start;"> <div style="text-align: center;"> <p><b>Top coat</b></p> <p><b>Bottom coat</b></p>  </div> <div style="text-align: center;"> <p><b>NiCrO<sub>x</sub> layer</b></p> <p><b>Ag layer</b></p> <p><b>Glass substrate</b></p>  </div> </div>	

the SEM chamber. The heating was performed in high vacuum through a heating plate that was set at 600°C. However, due to the thickness of the sample used, 4 mm, the temperature obtained at the surface of the sample, where the coating is situated and the scratch was performed, was expected to be significantly lower than the set temperature (predicted to reach maximum temperatures of 300-350°C). Moreover, the ramping speed used was 40°C/min, leading to a total ramping duration of 15 minutes. The temperature was set in place for 60 minutes and the ramp down was performed similarly to the ramp up. Consequently, the methodology of the SEM-HT differs from the faster

HT typically performed in air in a furnace and is expected to present less comparable features. Assumed to be a result of the lower surface temperature obtained, the SEM results obtained after the SEM-HT showed little change on the surface of the scratch and the few degradation features observed were depicted as small white patches located near the edges of the scratch track, where partial delamination was present in the AC state. The EDS resolution was too low to clearly decipher the chemical signal of the patches; however, they were assumed to be traces of Ag. The sample was then prepared for TEM for further investigation. Figure 4.21. shows, the full lamella prepared as well as high magnification regions of interest.

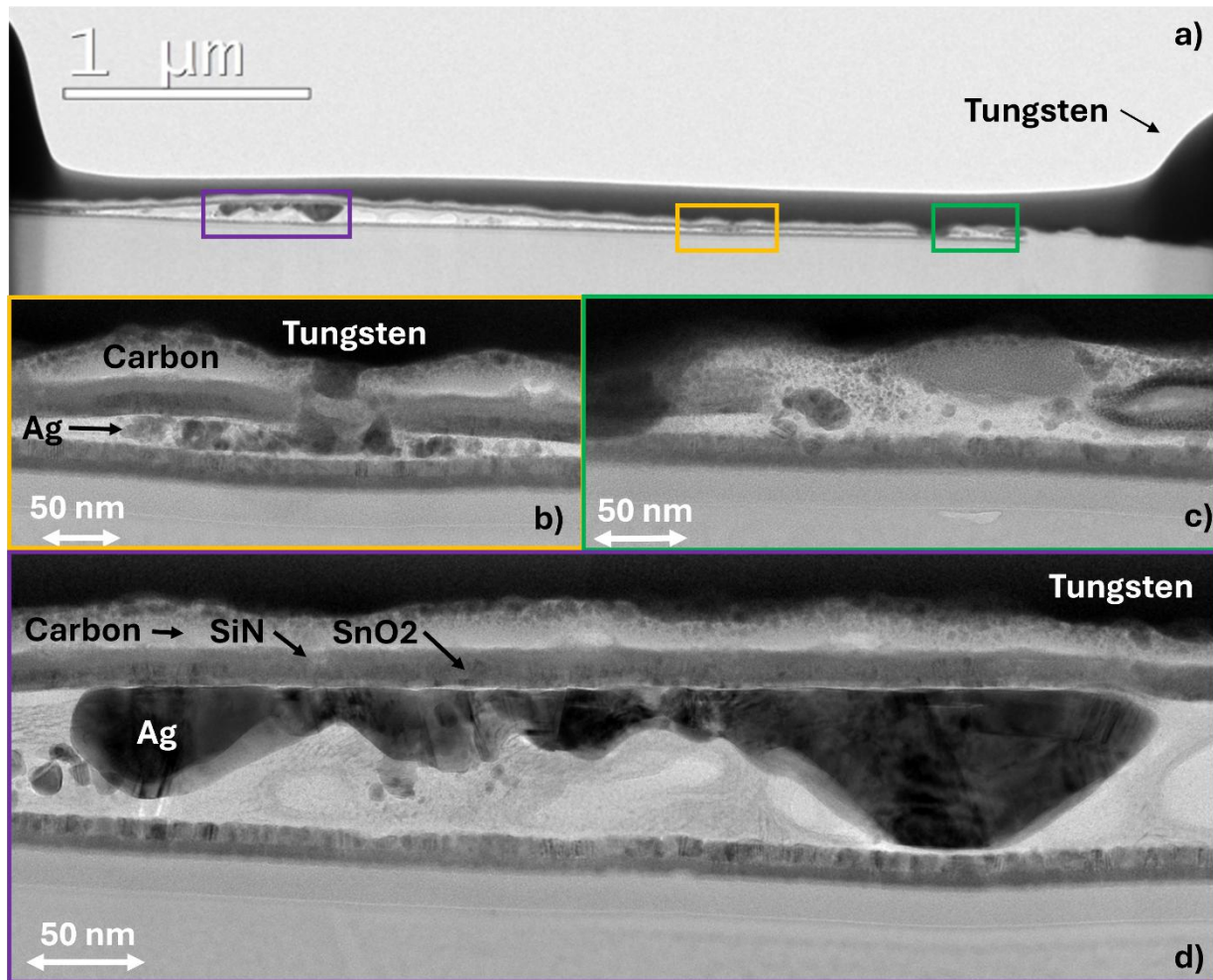


**Figure 5.1:** a) Full TEM image of a lamella taken from a heat-treated (under SEM) scratched sample (0.8 N load). b), c) and d) correspond to higher magnification TEM images of regions of interest within the cross-section.

The depletion and agglomeration of the Ag layer seen in Figures 4.21a and 4.21d is naturally associated with the heating that was performed. However, openings in the topcoat as well as the disturbance observed in the upper layers seen in Figures 4.21b and 4.21c, apart from the already degraded Ag layer, could be linked to the formation of the scratch, and not due to heating. In fact, one of the two main features that was observed multiple times in typically HT scratches was the fully delaminated regions separating the majority of the stack from the substrate (as seen in Figure 4.11). Openings and disruption in the upper layers such as the one presented here were not observed for lower load scratches, in AC and HT states (see Figure 4.10 and Figure 4.11). This leads us to believe that higher load scratching will create a higher level of disruption in the as-coated state compared to what is seen in lower load AC scratches.

AC visibility is observed externally as a result of the other changes within the coating following the scratch formation, and the plastic deformation informs on the general deformation of the whole coating. It is thus believed that the changes related to crack formation as well as Ag and NiCrO<sub>x</sub> disruption play a key role in the degradation. Ag and NiCrO<sub>x</sub> disruption cause an unstable morphology of the Ag layer. The Ag layer that was once uniformly encapsulated, is now distorted and upon heating, the Ag atoms will, in an attempt to reach a thermal-equilibrium state, diffuse and agglomerate within the coating [49], [50]. Again, this is enabled by the fact that the coating itself is deformed, and layers are expected to show less adhesion with one another than if the coating was not scratched. Both effects are expected to go hand in hand. During the heat treatment, weakened adhesion between the Ag and NiCrO<sub>x</sub> layers will lead to delamination that will give rise to more disruption of the Ag layer since the mobility of the now near-unencapsulated Ag layer is increased. Similarly, Ag agglomeration within its layer will lead to further adhesion failure and collapse of adjacent layers as well by creating regions in the coating where the depletion of Ag atoms creates voids within its layer. Here, the magnitude of the effect is rather clear, on higher loading scratches, where we expect higher disruptions in these layers, the intensification is higher following HT. The crack formation enables diffusion within the coating in a sense that paths are created and can be used by mobile atoms (i.e. Ag) to diffuse and cluster in various locations within the coating. It can become difficult to dissociate and evaluate the magnitude of the contribution of the crack formation enabling Ag diffusion, without humidity exposure, from the Ag and NiCrO<sub>x</sub> disruption as higher loading presents high instances of both effects. It would be hard to conduct an experiment where a lower density of cracks is formed paired with a high disruption of the Ag and

NiCrO<sub>x</sub> layers or the other way around. On sample T-6, a high intensification was observed even on lower load scratches, where we would expect minimal crack formation with more significant disruption as multiple top layers as well as the NiCrO<sub>x</sub> layer were removed. However, the lower scratch resistance expected due to the lower overall coating thickness is suspected to increase the crack formation as well, even at lower loads. Nonetheless, in all cases, the crack formation and disruption involves a higher mobility and diffusion of the Ag atoms, increasing the degradation via clustering and agglomeration and thus, visibility.

Furthermore, from Section 4.3.2, with the humidity tests, it was revealed that exposure to moisture increased the intensification behavior, indicating that these diffusion paths, created by the formation of cracks, enable the H<sub>2</sub>O molecules to travel inside the coating and reach the Ag layer, oxidizing it and in turn weakening adhesion with the neighboring layers [48], [51], [53]. The H<sub>2</sub>O contamination contribution to the degradation is suggested to be partly inconsequential compared to the degradation enabled by significant Ag and NiCrO<sub>x</sub> disruption. In fact, in cases where the disruption is expected to be already notable, with higher loading for example, the humidity exposure doesn't contribute significantly to the scratch intensification, as comparing high loading in humid and vacuum conditions resulted in similar intensification behavior (see Figure 4.20). The contribution of contamination of the coating through exposure to moisture becomes apparent at lower loads where the visibility is significantly increased following the heat treatment in comparison to scratches that remain mostly invisible when stored in vacuum. In this sense, exposure to humidity has an important detrimental effect at lower loads, where the layers' disruptions are still minimal. This result is notable in the fact that it suggests a possible reversibility of the damage that can result in a mitigation of the degradation. Contrary to the case of high load scratches, where it is understood that the significant damage created upon scratching will inevitably cause degradation when heating, with lower load scratches, storage in an unreactive environment ensures that the degradation stays minimal. Preliminary experiments aiming to mitigate the intensification for lower load scratches stored in humid conditions were conducted. The methodology involved scratching the REF sample as usual and storing it for 72 h in a high humidity environment ( $\approx 75\%RH$ ). Prior to performing the typical 12 minutes, 650 °C treatment, a pre-heat treatment of 5 minutes at 150 °C was performed with the goal of extracting any traces of adsorbed water from the surface of the sample. A sample stored in humidity and one stored in vacuum with no pre-treating were also added to compare the results. The result showed that the visibility of the



scratches that were stored in humidity and pre-heated, were in fact lower than the one observed for the sample that was stored in humidity without pre-heating. In addition, the sample stored in vacuum presented the lowest HT visibility. Again, consistent with our model of degradation, this experiment showed that it was possible to mitigate the detrimental impact of the exposure to humidity on the degradation. Nonetheless, samples scratched with lower loads (minimal disruption and crack formation) and stored in an unreactive environment (no corrosion of the damaged material) still showed some intensification, confirming that, much like at higher loads, the creation of disruption upon scratching, even if minimal, will be enhanced through the HT.

## CHAPTER 6 CONCLUSION AND RECOMMENDATIONS

This work evaluated the visibility of created scratch defects on Ag-based low-e coatings and studied their evolution following high temperature heat treatments. Three sub-objectives of the project were put forward. First, characterize the as-coated and heat-treated surface defects on low-e coatings, aiming to reproduce noticeable defects that are representative of real-life occurrences that arise in the field. Second, develop an experimental setup that could provide reproducible images of the created surface defects in their AC and HT states, and provide a basis for a methodology that is able to quantitatively compare the images and the corresponding effects. Third, present a model for the degradation of surface defects on Ag-based low-e coatings undergoing heat treatments.

The first objective was completed by performing scratch testing on reference low-e samples and by defining a specific range of scratch loads for which different cohesive and adhesive failure modes were observed. The characterization was obtained with morphological and chemical analyses performed with AFM, SEM, TEM and EDS in order to confirm the presence and extent of each failure mode for the different defined load regimes. It was found that lower loads (0.4 N and lower) led to a low plastic deformation of the coating and substrate (under 10 nm of total penetration depth, the presence of tensile cracking and a low density of partial delamination, whereas higher loads (0.5 N and higher) presented significant plastic deformation (over 100 nm of total penetration depth), while showing an increased density of tensile cracking and partial delamination in their as-coated state. This characterization helped explain the increase in as-coated visibility observed for higher loading scratches. The measurements performed for heat-treated defects, revealed that the degradation of the coating manifested itself via the delamination of the full coating in various locations within the scratch track as well as via the formation of large Ag nanoparticles (50-150 nm in radius) that were found throughout the coating, from the location of the original, pristine Ag layer.

The second objective was realized, and an experimental photography setup has been designed and constructed to take reproducible images of the generated scratches. The control of the imaging parameters (aperture, sensitivity and exposure time) as well as the lighting configuration of the setup were designed to be controlled remotely. As such, a certain automatization of the image

acquisition methodology was achieved, and consistent images could be taken. Paired with that, a home-made *Python* image processing code was written in order to create quantifiable metrics related to the visibility of the scratches, used to accurately compare the scratches in their AC and HT state. Quantitative metrics such as the  $\Delta PI$ , the variation in intensity between AC and HT scratches, the  $S_w$ , the width of the scratches as well as background intensities of the samples were all used to assess the observed defect intensification.

Finally, a model for the degradation of scratches following the high temperature heat treatment was proposed. The degradation, localized at the scratches, was linked to two main types of failure in the coating created during scratching, the disruption of the Ag metallic layer and  $NiCrO_x$  protective layer, and the formation of cracks. The disruption of these key layers enabled the degradation within the scratch tracks by creating an unstable Ag layer. Upon heating, with its higher mobility and diffusion, Ag atoms were favored to diffuse and aggregate, creating nanoparticles and clusters in the topcoat, bottom coat, and voids created by the full delamination of the coating between the coating and the substrate.

Similarly, crack formation is expected to play a part in the diffusion of the Ag atoms as well, creating pathways within the coating for the Ag to diffuse in various locations. Results revealed that exposure to humidity, where  $H_2O$  molecules are expected to react with the Ag layer through the openings in the films, resulted in a stronger intensification. This result also indicated that the degradation due to the layers' disruption is greater than the one due to contamination from the environment. In fact, when the disruption is significant, the intensification behavior remains similar regardless of storing conditions. It is only at lower loads, with reduced disruption, that the increase in intensification is observed for the samples stored in humidity compared to low vacuum.

Finally, a few considerations/recommendations for the improvement of the degradation model are proposed here that stem from the many results and articles reviewed that were conducted throughout the course of this work. First, the focus was put in constantly comparing the AC and HT states of the created scratches to determine the underlying degradation mechanisms occurring during the heat treatment. It would be of interest to pay close attention to the dynamics at play *during* the heat treatment as it could greatly inform on the sequence of the observed degradation mechanisms allowing for a step-by-step degradation model. As such, high-temperature SEM and TEM analyses are recommended with as-coated, damaged samples as a way to investigate the

dynamics of the degradation further. Similarly, the assessment of heat treatments at various temperatures would help identify at which temperatures the different mechanisms are enabled (delamination of the coating, diffusion, and agglomeration of Ag). Moreover, the appearance of tensile cracking was made clear with SEM imaging but was not revealed with the tested TEM lamellas. These cracks are possibly hidden when preparing cross-sections that are perpendicular to the scratch direction. Therefore, using cross-sections parallel to the direction of the scratch could reveal those cracks and help investigate their extent. Furthermore, it was pointed out in the literature review that stress changes, expected during the high temperature treatments, are known to affect the scratch resistance and expected to impact the degradation as well, and in turn, the resulting visibility. Therefore, one would gain a great deal by quantitatively assessing, and perhaps, modifying the different stress levels of the layers within the coating and compare it with the observed intensification of the defects. Studying the stress changes during heating of fewer layers (one-layer, bi-layer and tri-layer) systems would provide a more systematical approach where the specific influence and behavior of each individual film could be better understood and linked to the overall behavior observed in the tested multilayer coatings.

## REFERENCES

- [1] U. N. Environment, “2022 Global Status Report for Buildings and Construction,” UNEP - UN Environment Programme. Accessed: Apr. 02, 2024. [Online]. Available: <http://www.unep.org/resources/publication/2022-global-status-report-buildings-and-construction>
- [2] “Transition to Sustainable Buildings – Analysis,” IEA. Accessed: Apr. 02, 2024. [Online]. Available: <https://www.iea.org/reports/transition-to-sustainable-buildings>
- [3] “Energy Efficient Window Coverings,” Energy.gov. Accessed: Apr. 02, 2024. [Online]. Available: <https://www.energy.gov/energysaver/energy-efficient-window-coverings>
- [4] N. Herguedas and E. Carretero, “Evaluation of low-emissivity coatings with single, double, and triple silver layers,” *Solar Energy Materials and Solar Cells*, vol. 263, p. 112592, Dec. 2023, doi: 10.1016/j.solmat.2023.112592.
- [5] G. K. Dalapati *et al.*, “Transparent heat regulating (THR) materials and coatings for energy saving window applications: Impact of materials design, micro-structural, and interface quality on the THR performance,” *Progress in Materials Science*, vol. 95, pp. 42–131, Jun. 2018, doi: 10.1016/j.pmatsci.2018.02.007.
- [6] K. Sun, X. Tang, C. Yang, and D. Jin, “Preparation and performance of low-emissivity Al-doped ZnO films for energy-saving glass,” *Ceramics International*, vol. 44, no. 16, pp. 19597–19602, Nov. 2018, doi: 10.1016/j.ceramint.2018.07.207.
- [7] G. Ding and C. Clavero, “Silver-Based Low-Emissivity Coating Technology for Energy-Saving Window Applications,” in *Modern Technologies for Creating the Thin-film Systems and Coatings*, N. N. Nikitenkov, Ed., InTech, 2017. doi: 10.5772/67085.
- [8] B. P. Jelle, S. E. Kalnæs, and T. Gao, “Low-emissivity materials for building applications: A state-of-the-art review and future research perspectives,” *Energy and Buildings*, vol. 96, pp. 329–356, Jun. 2015, doi: 10.1016/j.enbuild.2015.03.024.
- [9] M. G. Hutchins, “Selective thin film coatings for the conversion of solar radiation,” *Surface Technology*, vol. 20, no. 4, pp. 301–320, Dec. 1983, doi: 10.1016/0376-4583(83)90111-5.
- [10] “Solar control glass | SunGuard glass products,” Guardian Glass. Accessed: Apr. 02, 2024. [Online]. Available: <https://www.guardianglass.com/us/en/our-glass/glass-types/solar-control-glass>
- [11] A. Mareška, T. Kordová, and M. H. Míka, “Defects on silver based coatings,” *Koroze a ochrana materialu*, vol. 66, no. 1, pp. 72–80, Jan. 2022, doi: 10.2478/kom-2022-0011.
- [12] M. Meszaros, “Effect of thermal annealing on the mechanical properties of low-emissivity physical vapor deposited multilayer-coatings for architectural applications”.
- [13] N. Sheth *et al.*, “Effects of tempering and heat strengthening on hardness, indentation fracture resistance, and wear of soda lime float glass,” *Int J of Appl Glass Sci*, vol. 10, no. 4, pp. 431–440, Oct. 2019, doi: 10.1111/ijag.13507.
- [14] D.-Y. Ju, S. Ishiguro, T. Arizono, and K. Hasegawa, “Effect of additional element and heat treating temperature on micro-structure and mechanical behavior of Ag alloy thin film,” *Transactions of Nonferrous Metals Society of China (English Edition)*, vol. 16, no. SUPPL., pp. s217–s219, 2006, doi: 10.1016/S1003-6326(06)60178-7.
- [15] Y. Liu, W. Zhang, Y. Sun, and W. Liang, “Diffusion behavior of Ag in TiO<sub>2</sub> nanofilms,” *Materials Research Bulletin*, vol. 98, pp. 240–249, Feb. 2018, doi: 10.1016/j.materresbull.2017.10.027.

- [16] J. Kulczyk-Malecka, P. J. Kelly, G. West, G. C. B. Clarke, and J. A. Ridealgh, "Investigations of diffusion behaviour in Al-doped zinc oxide and zinc stannate coatings," *Thin Solid Films*, vol. 520, no. 5, pp. 1368–1374, Dec. 2011, doi: 10.1016/j.tsf.2011.08.076.
- [17] V. I. Egorov, A. I. Sidorov, A. V. Nashchekin, P. A. Obratsov, and P. N. Brunkov, "Investigation of the morphological features of silver nanoparticles in the near-surface layers of glass when they are synthesized by heat treatment in water vapor," *Journal of Optical Technology (A Translation of Opticheskii Zhurnal)*, vol. 80, no. 3, pp. 174–178, 2013, doi: 10.1364/JOT.80.000174.
- [18] J. Kulczyk-Malecka *et al.*, "Investigation of silver diffusion in TiO<sub>2</sub>/Ag/TiO<sub>2</sub> coatings," *Acta materialia*, vol. 66, pp. 396–404, 2014.
- [19] C. H. Stoessel, "Optical coatings for automotive and building applications," in *Optical Thin Films and Coatings*, Elsevier, 2013, pp. 718–740. doi: 10.1533/9780857097316.4.718.
- [20] G. Stachowiak, "Coated article with anti-reflective layer(s) system," US 6,589,658 B1, Jul. 08, 2003
- [21] Blacker, Frank, and Imran, "BARRIER LAYERS COMPRISING NI AND/OR TI, COATED BARRIER LAYERS, AND METHODS OF MAKING THE SAME," US 8,790,783 B2, Jul. 29, 2014
- [22] S. Kim and J.-L. Lee, "Design of dielectric/metal/dielectric transparent electrodes for flexible electronics," *J. Photon. Energy*, vol. 2, no. 1, p. 021215, Oct. 2012, doi: 10.1117/1.JPE.2.021215.
- [23] P. B. Johnson and R. W. Christy, "Optical Constants of the Noble Metals," *Phys. Rev. B*, vol. 6, no. 12, pp. 4370–4379, Dec. 1972, doi: 10.1103/PhysRevB.6.4370.
- [24] X. Sun, R. Hong, H. Hou, Z. Fan, and J. Shao, "Thickness dependence of structure and optical properties of silver films deposited by magnetron sputtering," *Thin Solid Films*, vol. 515, no. 17, pp. 6962–6966, Jun. 2007, doi: 10.1016/j.tsf.2007.02.017.
- [25] W. N. S. Wan Shamsuddin, "Environmentally durable low-e coatings."
- [26] P. Rumsby, "Metal-based antireflective coatings with improved durability for ophthalmic applications."
- [27] P. J. Ries, "Silver thin films: Improving the efficiency of low-E coatings by employing different seed layers," Jun. 2015.
- [28] J. Zhang, Y. Zhang, K. Tse, X. Hu, D. Bei, and Z. Junyi, "Surface energy calculations from Zinc blende (111)/(-1-1-1) to Wurtzite (0001)/(0000-1): a study of ZnO and GaN," Oct. 2015.
- [29] G. Zhao *et al.*, "Strategy for improving Ag wetting on oxides: Coalescence dynamics versus nucleation density," *Applied Surface Science*, vol. 510, p. 145515, Apr. 2020, doi: 10.1016/j.apsusc.2020.145515.
- [30] D. Cornil, H. Wiame, B. Lecomte, J. Cornil, and D. Beljonne, "Which Oxide for Low-Emissivity Glasses? First-Principles Modeling of Silver Adhesion," *ACS Appl. Mater. Interfaces*, vol. 9, no. 21, pp. 18346–18354, May 2017, doi: 10.1021/acsami.7b03269.
- [31] S. Hafezian, R. Beaini, L. Martinu, and S. Kéna-Cohen, "Degradation mechanism of protected ultrathin silver films and the effect of the seed layer," *Applied Surface Science*, vol. 484, pp. 335–340, Aug. 2019, doi: 10.1016/j.apsusc.2019.04.043.
- [32] Z. Wang, X. Cai, Q. Chen, and P. K. Chu, "Effects of Ti transition layer on stability of silver/titanium dioxide multilayered structure," *Thin Solid Films*, vol. 515, no. 5, pp. 3146–3150, Jan. 2007, doi: 10.1016/j.tsf.2006.08.040.
- [33] K. P. Marimuthu, G. Han, and H. Lee, "Multilayer thin film metallic glasses under nanoscratch: Deformation and failure characteristics," *Journal of Non-Crystalline Solids*, vol. 601, p. 122047, Feb. 2023, doi: 10.1016/j.jnoncrysol.2022.122047.

- [34] C. A. Paulson *et al.*, “Industrial-grade anti-reflection coatings with extreme scratch resistance,” *Opt. Lett.*, vol. 44, no. 24, p. 5977, Dec. 2019, doi: 10.1364/OL.44.005977.
- [35] I. Zakiev, G. A. Gogotsi, M. Storchak, and V. Zakiev, “Glass Fracture during Micro-Scratching,” *Surfaces*, vol. 3, no. 2, pp. 211–224, Jun. 2020, doi: 10.3390/surfaces3020016.
- [36] Chorfa, Belkhir, Hamidouche, and Petit, “Study Of The Glass Deformation Regime Transition Using Indentation And Scratch Test,” *Verres Céramiques Composites*, vol. Volume 2, no. Numéro 1, p. Pages 19-25, Jun. 2012.
- [37] M. Sebastiani *et al.*, “Nano-Scale Residual Stress Profiling in Thin Multilayer Films with Non-Equibiaxial Stress State,” *Nanomaterials*, vol. 10, no. 5, p. 853, Apr. 2020, doi: 10.3390/nano10050853.
- [38] R. Ali, M. Sebastiani, and E. Bemporad, “Influence of Ti–TiN multilayer PVD-coatings design on residual stresses and adhesion,” *Materials & Design*, vol. 75, pp. 47–56, Jun. 2015, doi: 10.1016/j.matdes.2015.03.007.
- [39] R. Ali, M. Renzelli, M. I. Khan, M. Sebastiani, and E. Bemporad, “Effects of Residual Stress Distribution on Interfacial Adhesion of Magnetron Sputtered AlN and AlN/Al Nanostructured Coatings on a (100) Silicon Substrate,” *Nanomaterials*, vol. 8, no. 11, p. 896, Nov. 2018, doi: 10.3390/nano8110896.
- [40] Home *et al.*, “Soda-lime glass Material Properties,” Imetra, Inc. Accessed: Aug. 28, 2024. [Online]. Available: <https://www.imetra.com/soda-lime-glass-material-properties/>
- [41] “Thermal Expansion - Linear Expansion Coefficients.” Accessed: Aug. 28, 2024. [Online]. Available: [https://www.engineeringtoolbox.com/linear-expansion-coefficients-d\\_95.html](https://www.engineeringtoolbox.com/linear-expansion-coefficients-d_95.html)
- [42] M. Powers, B. Derby, E. Raeker, N. Champion, and A. Misra, “Hillock formation in co-deposited thin films of immiscible metal alloy systems,” *Thin Solid Films*, vol. 693, p. 137692, Jan. 2020, doi: 10.1016/j.tsf.2019.137692.
- [43] “Standard Test Method for Adhesion Strength and Mechanical Failure Modes of Ceramic Coatings by Quantitative Single Point Scratch Testing.” Accessed: Sep. 12, 2022. [Online]. Available: <https://www.astm.org/c1624-22.html>
- [44] S. J. Bull, “Failure mode maps in the thin film scratch adhesion test,” *Tribology International*, vol. 30, no. 7, pp. 491–498, Jul. 1997, doi: 10.1016/S0301-679X(97)00012-1.
- [45] S. J. Bull, “Failure modes in scratch adhesion testing,” *Surface and Coatings Technology*, vol. 50, no. 1, pp. 25–32, Jan. 1991, doi: 10.1016/0257-8972(91)90188-3.
- [46] P. J. Burnett and D. S. Rickerby, “The scratch adhesion test: An elastic-plastic indentation analysis,” *Thin Solid Films*, vol. 157, no. 2, pp. 233–254, Feb. 1988, doi: 10.1016/0040-6090(88)90006-5.
- [47] B. Lenz, H. Hasselbruch, H. Großmann, and A. Mehner, “Application of CNN networks for an automatic determination of critical loads in scratch tests on a-C:H:W coatings,” *Surface and Coatings Technology*, vol. 393, p. 125764, Jul. 2020, doi: 10.1016/j.surfcoat.2020.125764.
- [48] T. E. Graedel, “Corrosion Mechanisms for Silver Exposed to the Atmosphere,” *J. Electrochem. Soc.*, vol. 139, no. 7, p. 1963, Jul. 1992, doi: 10.1149/1.2221162.
- [49] P. Jacquet *et al.*, “On the solid-state dewetting of polycrystalline thin films: Capillary versus grain growth approach,” *Acta Materialia*, vol. 143, pp. 281–290, Jan. 2018, doi: 10.1016/j.actamat.2017.08.070.
- [50] P. Jacquet *et al.*, “Grain growth: The key to understand solid-state dewetting of silver thin films,” *Scripta Materialia*, vol. 115, pp. 128–132, Apr. 2016, doi: 10.1016/j.scriptamat.2016.01.005.

- [51] R. C. Ross, "Observations on humidity-induced degradation of Ag-based low-emissivity films," *Solar Energy Materials*, vol. 21, no. 1, pp. 25–42, Nov. 1990, doi: 10.1016/0165-1633(90)90040-8.
- [52] G. Abadias, A. Michel, C. Tromas, C. Jaouen, and S. N. Dub, "Stress, interfacial effects and mechanical properties of nanoscale multilayered coatings," *Surface and Coatings Technology*, vol. 202, no. 4–7, pp. 844–853, Dec. 2007, doi: 10.1016/j.surfcoat.2007.05.068.
- [53] H. S. Park and D. E. Day, "CORROSION OF EVAPORATED Ag FILMS ON GLASS BY SATURATED WATER VAPOR.," *Solar energy materials*, vol. 13, no. 5, pp. 351–365, 1986.
- [54] J. Kulczyk-Malecka, "Diffusion Studies in Toughenable Low-E Coatings."
- [55] W. Kono, "METHOD OF SULFIDE TARNISH INHIBITING OF SILVER-COPPER, SILVER-GOLD AND SILVER-COPPER.GOLD ALLOYS," 4,775,511, Oct. 04, 1988
- [56] D. Davitz, "SILVER-COLORED ALLOY WITH LOW PERCENTAGES OF COPPER AND ZINC," US 7,128,871 B2, Oct. 31, 2006
- [57] E. Suoninen, H. Herø, and E. Minni, "Effect of palladium on sulfide tarnishing of noble metal alloys," *J. Biomed. Mater. Res.*, vol. 19, no. 8, pp. 917–934, Oct. 1985, doi: 10.1002/jbm.820190804.
- [58] M. Zhou, Y. Cai, Y.-P. Li, and D.-Q. Liu, "Durability of Ultra-Thin Silver Films and Silver—Gold Alloy Films under UV Irradiation," *Chinese Phys. Lett.*, vol. 33, no. 10, p. 107803, Oct. 2016, doi: 10.1088/0256-307X/33/10/107803.
- [59] E. Ando, S. Suzuki, N. Aomine, M. Miyazaki, and M. Tada, "Sputtered silver-based low-emissivity coatings with high moisture durability," *Vacuum*, vol. 59, no. 2–3, pp. 792–799, Nov. 2000, doi: 10.1016/S0042-207X(00)00349-3.
- [60] K. Koike, K. Shimada, and S. Fukuda, "Aggregation in thin-film silver: Induced by chlorine and inhibited by alloying with two dopants," *Corrosion Science*, vol. 51, no. 11, pp. 2557–2564, Nov. 2009, doi: 10.1016/j.corsci.2009.06.044.
- [61] A. G. Dirks, J. J. Van Den Broek, and P. E. Wierenga, "Mechanical properties of thin alloy films: Ultramicrohardness and internal stress," *Journal of Applied Physics*, vol. 55, no. 12, pp. 4248–4256, Jun. 1984, doi: 10.1063/1.333027.
- [62] W. N. S. Wan Shamsuddin, A. Roccisano, K. Zuber, P. J. Murphy, and M. Llusca Jane, "Environmentally robust Ag–Cu based low-e coatings," *Solar Energy Materials and Solar Cells*, vol. 248, p. 112033, Dec. 2022, doi: 10.1016/j.solmat.2022.112033.
- [63] "Key to heterogeneous integration: Materials Bonding Stress - iST -Integrated Service Technology," iST-Integrated Service Technology. Accessed: Nov. 04, 2024. [Online]. Available: [https://www.istgroup.com/en/tech\\_20220802-materials-bonding-stress/](https://www.istgroup.com/en/tech_20220802-materials-bonding-stress/)
- [64] L. Lin, "Test apparatus and method of measuring mar resistance of film or coating," US 6,520,004 B1, Feb. 18, 2003
- [65] "Oliver-Pharr Method - an overview | ScienceDirect Topics." Accessed: Nov. 18, 2024. [Online]. Available: <https://www.sciencedirect.com/topics/engineering/oliver-pharr-method>
- [66] 관리자, "SEM Technology | Specialize in Industrial X-ray inspection system and SEM(Scanning Electron Microscope) | SEC Co., Ltd.," SEC. Accessed: Nov. 04, 2024. [Online]. Available: [https://www.seceng.co.kr/eng/technology/sem\\_tech/](https://www.seceng.co.kr/eng/technology/sem_tech/)
- [67] O. Marti, "AFM Instrumentation and Tips," in *Handbook of Micro/Nano Tribology*, 2nd ed., CRC Press, 1999.
- [68] A. Rochefort, "MTR6040E – Characterization of materials, Chapter 9: Chemical composition of surfaces Page 9-12," Physics Engineering, Polytechnique Montréal, 2023.



- [69] T. Poirié, T. Schmitt, E. Bousser, L. Martinu, and J.-E. Klemberg-Sapieha, “Influence of internal stress in optical thin films on their failure modes assessed by in situ real-time scratch analysis,” *Tribology International*, vol. 109, pp. 355–366, May 2017, doi: 10.1016/j.triboint.2016.12.053.

## APPENDIX A Visibility assessment *Python* Code – Image Processing

<pre> '''python  from PIL import Image import numpy as np import matplotlib.pyplot as plt from scipy.signal import find_peaks from scipy.signal import peak_widths ''' </pre>	1
<pre> # Load the first image img1 = Image.open(r"Path to image")  # Convert the first image to grayscale gray_img1 = img1.convert("L")  # Convert the grayscale image to a NumPy array img_arr1 = np.array(gray_img1)  # Get the number of pixels in the x and y directions x_pixels1, y_pixels1 = img_arr1.shape[1], img_arr1.shape[0]  # Calculate the average intensity of all y-cross sections avg_intensity1 = np.mean(img_arr1, axis=0)  # Plot the average intensity plt.plot(range(x_pixels1), avg_intensity1) plt.xlabel("Pixels in x direction") plt.ylabel("Average Intensity") plt.title("Average Intensity across y-cross sections") plt.show()  #plt.imshow(img1, cmap='gray')  pixels_to_crop = 70  # Crop the bottom 'pixels_to_crop' pixels cropped_img_arr = img_arr1[:y_pixels1 - pixels_to_crop, :]  # Convert the cropped NumPy array back to an image cropped_img = Image.fromarray(cropped_img_arr)  #plt.imshow(cropped_img, cmap='gray') ''' </pre>	2
<pre> #Baseline regression  # Generate the x-coordinates (assuming equal spacing) </pre>	3

<pre> x = np.arange(len(avg_intensity1))  # Perform linear regression to estimate the baseline regression1 = np.polyfit(x, avg_intensity1, 3) baseline1 = np.polyval(regression1, x)  # Subtract the baseline from the intensity signal leveled_intensity1 = avg_intensity1 - baseline1  # Plotting the original intensity signal and the leveled signal plt.figure(figsize=(8, 4)) plt.plot(x, leveled_intensity1, label='Leveled Intensity') plt.xlabel('x') plt.ylabel('Average Intensity') plt.legend() plt.show() \`\` </pre>	
<pre> # Find the peaks in the intensity values peaks1, _ = find_peaks(avg_intensity1, prominence=2, width=1) # Adjust the prominence threshold as needed  # Calculate the integral for each peak peak_integrals1 = [] max_of_peak1_values = []  for i in range(len(peaks1)):     max_of_peak1_index = peaks1[i]     start_index = max_of_peak1_index - 10     end_index = max_of_peak1_index + 10     peak_intensity_values = avg_intensity1[start_index:end_index]     peak_integrall1 = np.trapz(peak_intensity_values)     peak_integrals1.append(round(peak_integrall1,2))     max_of_peak1_values.append(round(avg_intensity1[max_of_peak1_index],2) ) widths1, _, _, _ = peak_widths(avg_intensity1, peaks1, rel_height=0.5)  print("Position in X pixels of the peaks:", peaks1) print("Maximum intensity of those peaks", max_of_peak1_values) print("FWHM values of those peaks", widths1) print("Integrals of individual peaks:", peak_integrals1) \`\` </pre>	4
<pre> #Define area coverage:  #Define a box around each scratch centered at the maximum value of the peak wide of 100 pixels (50 on each side) Threshold = 33 Coverage = []  for i in range(len(peaks1)):     max_of_peak1_index = peaks1[i]     start = max_of_peak1_index - 50 </pre>	5

```

end = max_of_peak1_index + 50
Coverage_Area = img_arr1[500:2500, start:end]
print(i)
print(max_of_peak1_index)

Intense_Pix = 0
Pix = 0

for x in range(len(Coverage_Area[:,0])):
    for y in range(len(Coverage_Area[0,:])):
        Pix += 1
        if Coverage_Area[x,y] > Threshold:
            Intense_Pix += 1

print(Intense_Pix, Pix)
Coverage_i = round((Intense_Pix/Pix)*100,2)
Coverage.append(Coverage_i)

Intense_Pix = 0
Pix = 0

print(Coverage)
` ``

```

```

# Assuming you have your image array and coordinates
# image_array = ... # Your image array
# coordinates = (x_start, y_start, x_end, y_end) # Coordinates of the
# crop

#max_of_peak1_index = peaks1[0]
#start = max_of_peak1_index - 100
#end = max_of_peak1_index + 100

# Crop the image
Coverage_Image = cropped_img_arr

# Display the original image and the cropped image side by side
plt.figure(figsize=(10, 5))

# Original image
plt.subplot(1, 2, 1)
plt.imshow(img_arr1)
plt.title('Original Image')

# Cropped image
plt.subplot(1, 2, 2)
plt.imshow(Coverage_Image)
plt.title('Cropped Image')

plt.tight_layout()
plt.show()

# Define the threshold
threshold = 110 # Adjust this value according to your needs

```

```

# Threshold the cropped image
thresholded_image = np.where(Coverage_Image > threshold, 255,
0).astype(np.uint8)

# Display the thresholded image
plt.imshow(thresholded_image, cmap='gray')
plt.title('Thresholded Image')
plt.axis('off') # Turn off axis labels and ticks
plt.show()

#Add coverage area: Light percentage
Coverage = []

Light_Pix = 0
Pix = 0

for x in range(len(Coverage_Image[:,0])):
for y in range(len(Coverage_Image[0,:])):
Pix += 1
if Coverage_Image[x,y] > threshold:
Light_Pix += 1

print(Light_Pix, Pix)
Coverage = round((Light_Pix/Pix)*100,2)
#Coverage.append(Coverage_i)

print(Coverage)

```

*One can repeat sections 1-6 for multiple different images for their respective analyses*

7

```

# Plot the normalized histograms of the two images
#avg_max_intensity_1 = np.mean(max_of_peak1_values)
#avg_max_intensity_2 = np.mean(max_of_peak2_values)
#avg_max_intensity_3 = np.mean(max_of_peak3_values)
#avg_max_intensity_4 = np.mean(max_of_peak3_values)

plt.plot(np.arange(x_pixels1) , leveled_intensity1, color='green')
#(AHIP: {round(avg_max_intensity_1)})')
plt.plot(np.arange(x_pixels2), leveled_intensity2, color='Red')
#(AHIP: {round(avg_max_intensity_2)})')
plt.plot(np.arange(x_pixels3), leveled_intensity3, color='purple',
label=f'0.4N, HT (0h of storage)') # (AHIP:
{round(avg_max_intensity_1)})')
plt.plot(np.arange(x_pixels4), Realleveled_intensity4,
color='orange', label=f'0.4N, HT (2h of storage)') # (AHIP:
{round(avg_max_intensity_1)})')
plt.xlabel("Pixels in X Direction")
plt.ylabel("Normalized Average Pixel Intensity")
plt.xlim([2900, 3000])
plt.ylim([-5,100])
plt.legend()

plt.show()

```

8